The interfacial contact of Cu/ZnO, and doped ZnO – different routes to modify the electronic, structural, and catalytic properties

Inaugural-Dissertation

to obtain the academic degree

Doctor rerum naturalium (Dr. rer. nat.)

submitted to the Department of Biology, Chemistry, Pharmacy

of Freie Universität Berlin

by

Elisabeth Hannah Wolf

from Köln-Porz

2020

This dissertation was prepared between September 2014 and November 2020 at the Fritz-Haber-Institut of the Max-Planck-Society under the supervision of Prof. Robert Schlögl.

1. Gutachter: Prof. Dr. Robert Schlögl

2. Gutachter: Prof. Dr. Thomas Risse

Disputation am 01.02.2021

Acknowledgements

For his mentoring, supervision, and support during my time as a PhD student, and for giving me the opportunity to work on this interesting topic, I would like to express my thanks to Prof. Robert Schlögl. Likewise, I thank Prof. Thomas Risse for his input, discussions, and advice, and for being the second thesis referee.

I would like to thank Dr. Elias Frei for his many discussions and support as well as the supervision of this project and my dissertation. Dr. Sébastien Cap is acknowledged as my former group leader and for advice regarding the writing of my thesis and one of the included paper drafts. Furthermore, I thank my former group leader, Prof. Maik Eichelbaum, for giving me the chance to start working at FHI as a doctoral researcher and his introduction to MCPT, as well as Dr. Katarzyna Skorupska for welcoming me in her group during the last part of my work at the FHI.

For the great opportunities presented by discussion meetings, block courses, a student-led conference, and soft skill courses, and especially for funding and the opportunity to attend conferences, I thank the International Max Planck Research School "Functional Interfaces in Physics and Chemistry". I especially thank the coordinators, Prof. Tobias Kampfrath and Dr. Alexander Paarmann, and the school's secretaries, Bettina Menzel and Ines Bressel, for discussions and support. Furthermore, I would express my gratitude for the funding received from the SFB 1349 and the fruitful discussions regarding the fluorine-related part of the project. (Gefördert durch die Deutsche Forschungsgemeinschaft (DFG) – Projektnummer 387284271 – SFB 1349)

I am especially grateful for the warm welcome, constructive work atmosphere and much advice regarding the operation of the MCPT setup and interpretation of results offered by my laboratory colleagues, Dr. Maria Heenemann and Dr. Anna Maria Wernbacher. For a great collaborative spirit and working atmosphere in the laboratory, I also thank Dr. Peter Kraus. Furthermore, I sincerely thank all colleagues and collaborators who have contributed to the experimental results presented in this thesis, in alphabetical order: Dr. Gerardo Algara-Siller, Daniel Brennecke, Thomas Drews, Wiebke Frandsen, Dr. Frank Girgsdies, Maike Hashagen, Dr. Walid Hetaba, Dr. Robert Imlau, Dr. Alexander Klyushin, Dr. Liudmyla Masliuk, Dr. Marie-Mathilde Millet, Dr. Hannah Nerl, Jessica Plagemann, Dr. Frenio Redeker, Dr. Wiebke Riedel, Prof. Sebastian Riedel, Priv.-Doz. Dr. Gudrun Scholz, Dr. Friedrich Seitz, Dr. Detre Teschner, Dr. Olaf Timpe, A. Samuel Tragl, Dr. Marc-Georg Willinger, Dr. Sabine Wrabetz, and Dr. Leon D. Zwiener. I thank Dr. Sylvia Becker and Natalia Kowalew for preparation of the hydrothermal carbon samples used for method development and Dr. Saskia Heumann for providing these samples.

I would like to express my sincere gratitude to Dr. Gregor Koch and Dr. Walid Hetaba, as well as all department colleagues for the many fruitful discussions about my projects. For teaching me the use of equipment as well as assistance in running experiments and equipment maintenance and repairs I thank Dr. Pierre Kube, Ezgi Erdem, Jutta Kröhnert, Daniel Brennecke, Jasmin Allan, and the colleagues at the electronics and mechanical workshops.

Many colleagues have made my time at FHI enjoyable and productive. I would like to express my thanks to the administrative and maintenance staff, and extend a special thanks to the secretaries, Andrea Moebius, Dorothea Damm, Sabrina Wobring, and Sibylle Hartung. I'd like to thank my fellow PhD representatives for the constructive atmosphere during meetings and events. I have made many great friends during my time at FHI, which greatly helped in making the working environment pleasant, for which I would like to express my gratitude. Here, I especially thank my office colleagues Leon, Max, Detre, Pia, and Ramzi.

I thank my teachers and mentors for increasing both my knowledge and enthusiasm for science and research. Finally, I would like to sincerely thank my family, especially my grandparents, my parents Ute and Peter, my siblings Johannes, Judith, and Matthias, and my fiancé for supporting me unconditionally.

Summary

In this thesis, Cu/ZnO catalysts active in the reduction of CO_2 were investigated using *operando* conductivity measurements. These measurements made use of a contact-free microwave cavity perturbation technique (MCPT). For the CO_2 reduction in methanol synthesis or the reverse water-gas shift reaction, the commonly used catalyst is $Cu/ZnO/Al_2O_3$ with high content of Cu. However, the exact electronic processes occurring between the ZnO support and the copper particles under reaction conditions are yet to be completely understood. Furthermore, the relevance and nature of the interface between the catalyst components Cu and ZnO are to be further studied. To contribute to this research, work regarding the structural, electronic, and catalytic properties of Cu/ZnO samples is presented, focusing on the interaction of Cu and ZnO. To reduce the system's complexity as well as facilitate the use of additional characterisation techniques, often model catalysts are employed.

To achieve the above-mentioned aims, binary Cu/ZnO samples were synthesised, where the loading of Cu was varied and kept low. Furthermore, different degrees of interaction were achieved by employing two synthetic approaches, namely impregnation and coprecipitation. Both the low Cu content as well as the chosen synthetic techniques are common strategies in the generation of Cu/ZnO model catalysts. The two synthesis methods were aimed at the generation of two very different precursors: while impregnation ideally leads to precursors with fully separated CuO and ZnO phases, coprecipitated samples were found to contain Cu incorporated into the ZnO lattice. Conversely, by activating the catalysts, a portion of the Cu contained in the samples generated by impregnation can migrate into the ZnO lattice, while some of the incorporated Cu in the coprecipitated samples can be extracted and form metallic Cu particles. A thorough characterisation of the samples enabled the investigation of their structural, electronic, and catalytic properties. By measuring the catalytic activity of these samples simultaneously with the MCPT conductivity, the electronic and catalytic properties can be related. A further aim of this investigation was to assess the suitability of the samples to function as models for the industrially applied catalytic system.

By using MCPT, the conductivity of the samples was measured *operando* in the reverse water-gas shift reaction. Interestingly, this revealed a qualitatively different behaviour of the samples generated by the distinct synthetic methods. While the CO production rate increased for both types of sample upon increasing the proportion of hydrogen in the reaction feed, the conductivity of samples generated by impregnation increased simultaneously, but the conductivity of the coprecipitated samples was found to decrease instead. This striking difference points at very different interactions between Cu and ZnO in these two sorts of samples. Further characterisation revealed that the samples differ not only as a consequence of their synthetic history, but also depending on their Cu content. The catalytic performance, e.g., the apparent activation energies of the samples towards the rWGS reaction, was found to differ significantly from the values expected for binary Cu/ZnO catalysts with industrially relevant Cu content. This shows that these samples with low Cu loadings are not applicable as model catalysts for the industrial system and

highlights the importance of ensuring the comparability of model and technical system before transferring conclusions from one to the other.

The reversible incorporation of Cu into the ZnO lattice, even when the sample is synthesised by impregnation, was further studied. For this, a sample with a Cu content below the dissolution limit of Cu in ZnO was characterised in more detail. This highlighted the contribution of small clusters and the modification of the ZnO structure by Cu ions. It was revealed that in its oxidised state, the sample contained isolated Cu^{2+} species in the ZnO lattice. These Cu^{2+} ions get reduced when a hydrogen containing gas feed is applied, which was demonstrated using inert transfer EPR and *in situ* MCPT measurements. This effect was also shown to be reversible by reoxidation of the sample.

Besides Cu, many other dopants are known to modify the properties of ZnO. Using fluorine as a modifier, the structural and electronic properties of ZnO as well as the way it interacts with applied gas phases were investigated. The fluorine-modification of polycrystalline ZnO was notably achieved by the application of gaseous fluorine and could be controlled by the variation of the treatment parameters such as the F_2 partial pressure. Two fluorinated samples with differing F contents were compared to pristine ZnO. Of these, the sample with lower F content was found to consist of a homogeneous distribution of fluorine as a dopant in ZnO, while the sample treated at a higher F_2 partial pressure contained ZnF_2 as a by-phase. The conductivity of the samples measured using MCPT revealed that the sample with less F content had a stronger response to the application of a hydrogen containing gas phase compared to pure ZnO or the sample containing the ZnF_2 by-phase, indicating that fluorine doping of ZnO positively affects the ability of the material to activate and chemisorb H_2. This finding can have extensive implications for the use of fluorine-doped ZnO in catalytic applications such as CO_2 reduction, which will be interesting to explore in the future.

Zusammenfassung

Im Rahmen dieser Arbeit wurden Cu/ZnO-Katalysatoren, die in der Reduktion von CO_2 aktiv sind, mittels *operando*-Leitfähigkeitsmessungen untersucht. Diese Messungen verwendeten die kontaktfreie Mikrowellenresonator-Störungsmethode (MCPT). Für die Reduktion von CO_2 in der Methanolsynthese und der reversen Wassergas-Shiftreaktion (rWGS) wird gewöhnlich ein Cu/ZnO/Al_2O_3-Katalysator mit hohem Kupferanteil verwendet. Die elektronischen Prozesse zwischen dem ZnO-Träger und den Kupferpartikeln unter Reaktionsbedingungen sind jedoch bisher nicht vollständig verstanden. Auch bedürfen die Wechselwirkungen zwischen den Katalysatorkomponenten Cu und ZnO weitergehender Untersuchung. Als Beitrag zu diesen Forschungen werden in dieser Arbeit Untersuchungen über die strukturellen, elektronischen, und katalytischen Eigenschaften von Cu/ZnO-Proben präsentiert, mit Fokus auf die Interaktion zwischen Cu und ZnO. Zur Verringerung der Komplexität des Systems und um weitere Charakterisierungsmethoden zu ermöglichen werden oft Modellkatalysatoren verwendet.

Um die oben genannten Ziele zu erreichen wurden binäre Cu/ZnO-Proben synthetisiert, deren Kupferbeladung variiert und generell klein gewählt wurde. Weiter konnten durch die Verwendung zweier unterschiedlicher Synthesemethoden, nämlich der Imprägnierung und der Kofällung, Proben mit unterschiedlichem Ausmaß an Interaktion zwischen Kupfer und Zink erhalten und untersucht werden. Sowohl der geringe Kupfergehalt sowie die gewählten Synthesetechniken sind häufig angewendete Strategien bei der Herstellung von Cu/ZnO-Modellkatalysatoren. Die beiden Synthesestrategien hatten das Ziel, zwei grundlegend verschiedene Präkursoren zu erzeugen: Während die Imprägnierung idealerweise zu Präkursoren mit vollständig separierten CuO und ZnO-Phasen führt, stellte sich heraus, dass in den kogefällten Proben Cu im ZnO-Kristallgitter enthalten ist. Bei Aktivierung der Katalysatoren migriert ein Teil des Cu in den Proben, die durch Imprägnierung hergestellt wurden, in das ZnO-Kristallgitter, während ein Teil des inkorporierten Kupfers in den kogefällten Proben aus der Struktur ausgelagert werden kann und metallische Cu-Partikel formt. Eine sorgfältige Charakterisierung der Proben ermöglichte die Untersuchung deren struktureller, elektronischer, und katalytischer Eigenschaften. Durch Messung der katalytischen Aktivität simultan mit der MCPT-Leitfähigkeit können die elektronischen und katalytischen Eigenschaften in Bezug gesetzt werden. Ein weiteres Ziel der Arbeit war es, die Eignung der Proben als Modell für das industriell angewandte Katalysatorsystem zu beurteilen.

Mittels Verwendung von MCPT wurde die Leitfähigkeit *operando* in der reversen Wassergaskonvertierungsreaktion gemessen. Interessanterweise zeigte sich ein qualitativ unterschiedliches Verhalten der Proben, die mit den deutlich verschiedenen Methoden synthetisiert wurden. Während die CO-Produktionsrate für beide Arten von Proben anstieg, wenn der Wasserstoffgehalt des Reaktionsgases erhöht wurde, zeigte die Leitfähigkeit der durch Imprägnierung hergestellten Proben einen gleichzeitigen Anstieg, aber die Leitfähigkeit der kogefällten Proben fiel hingegen ab. Dieser entscheidende Unterschied lässt auf deutlich unterschiedliche Cu-ZnO-Interaktionen der beiden Arten von Modellkatalysatoren schließen. Die weitere Charakterisierung der Proben machte deutlich, dass diese sich nicht nur als

Konsequenz der Synthesevergangenheit unterscheiden, sondern auch abhängig von ihrem Kupfergehalt. Es zeigte sich, dass die katalytischen Eigenschaften, z.B. die scheinbaren Aktivierungsenergien der Proben in der rWGS-Reaktion, sich deutlich von Werten unterscheiden, die für binäre Cu/ZnO-Katalysatoren mit industriell relevantem Kupfergehalt zu erwarten wären. Dies zeigt, dass diese Proben mit geringem Kupfergehalt nicht als Modellkatalysatoren für das Industrielle System geeignet sind, und unterstreicht die Bedeutung, die Vergleichbarkeit von Modell und technischem System sicher zu stellen, wenn Schlussfolgerungen von einem System zum anderen übertragen werden sollen.

Die reversible Aufnahme von Cu in die ZnO-Kristallstruktur, auch bei durch Imprägnierung synthetisierten Proben, wurde weiter untersucht. Dafür wurde eine Probe mit einem Cu-Gehalt unterhalb der Löslichkeitsgrenze von Cu in ZnO weitergehend charakterisiert. Dies unterstrich den Einfluss kleiner Cluster und der Modifikation der ZnO-Struktur durch Kupferionen auf die Messergebnisse. Es wurde gezeigt, dass die oxidierte Probe isolierte Cu^{2+}-Spezies im ZnO-Gitternetz enthält. Mittels EPR-Messungen nach Inerttransfer und *in situ* MCPT-Messungen wurde nachgewiesen, dass diese Cu^{2+}-Ionen beim Überleiten eines H_2-haltigen Gasfeeds über die Probe reduziert werden. Dieser Effekt ist durch Reoxidation der Probe reversibel.

Abgesehen von Cu sind auch viele andere Dopanden bekannt, die die Eigenschaften von ZnO verändern. Unter der Verwendung von Fluor zur Modifikation wurden die strukturellen und elektronischen Eigenschaften von ZnO sowie die Art und Weise der Interaktion mit angelegten Gasphasen untersucht. Hervorzuheben ist, dass die Fluor-Modifikation von polykristallinem ZnO durch das Anlegen von gasförmigem Fluor erreicht wurde und durch die Veränderung der Parameter dieser Behandlung, etwa des F_2-Partialdrucks, kontrolliert werden kann. Zwei fluorinierte Proben mit unterschiedlichem F-Gehalt wurden mit reinem ZnO verglichen. Es stellte sich heraus, dass die Probe mit niedrigerem F-Gehalt eine homogene Verteilung von Fluor als Dopanden im ZnO enthält, während die Probe, die mit einem höheren F_2-Partialdruck behandelt wurde, auch ZnF_2 als Nebenphase enthielt. Die Leitfähigkeit dieser Proben, gemessen mittels MCPT, macht deutlich, dass die Probe mit kleinerem F-Gehalt eine stärkere Veränderung bei Überleitung einer wasserstoffhaltigen Gasphase zeigt als reines ZnO oder auch die Probe, die die ZnF_2-Nebenphase enthält. Dies zeigt, dass die Fluordotierung des ZnO die Fähigkeit des Materials zur H_2-Aktivierung und -Chemisorption positiv beeinflusst. Dieses Ergebnis könnte weiterführende Konsequenzen für die Anwendung von fluordotiertem ZnO in katalytischen Anwendungen wie der CO_2-Reduktion haben. Es bietet sich daher für eine vertiefende zukünftige Untersuchung an.

Table of Contents

Table of Abbreviations

at. %	atom percent
BET	Brunauer-Emmet-Teller
BG	band gap
CB	carbon black
CW	continuous wave
DRIFT	diffuse reflectance infrared Fourier transform spectroscopy
DR-UV-vis	diffuse reflectance UV-visible spectroscopy
EDX	energy-dispersive X-ray spectroscopy
EELS	electron energy loss spectroscopy
EPR	electron paramagnetic resonance
EXAFS	extended X-ray absorption fine structure
FFT	fast Fourier transform
FHI	Fritz-Haber-Institute
FID	flame ionisation detector
FWHM	full width at half maximum
H_2-TPD	H_2- temperature programmed desorption
HRTEM	high resolution TEM
ICPE	inductively coupled plasma
LN_2	liquid N_2
MAS	magic angle spinning
MCPT	microwave cavity perturbation technique
N_2O-RFC	N_2O- reactive frontal chromatography
NEXAFS	near-edge x-ray absorption fine structure
NIR	near IR
NMR	nuclear magnetic resonance
OES	optical emission spectroscopy
rWGS	reverse Water Gas Shift
s.a.	surface acidity
SA	surface area
SDD	silicon drift detector

SEM	scanning electron microscope
SMSI	strong metal-support interaction
STEM	scanning transmission electron microscopy
TCD	thermal conductivity detector
TDS	thermal desorption spectroscopy
TEM	transmission electron microscopy
TM	transversal magnetic
UDOS	unoccupied density of states
UHV	ultra high vacuum
UPS	ultraviolet photoelectron spectroscopy
VNA	vector network analyser
wt. %	weight percent
XPS	X-ray photoelectron spectroscopy
XRD	X-ray diffraction
XRF	X-ray fluorescence

1 Introduction

The use of conventional fossil fuels such as oil and natural gas is problematic, since it leads to the depletion of finite resources and the release of detrimental climate-active combustion products such as carbon dioxide. For this reason, it is desirable to find alternative energy carriers and basic chemicals. An important role of such energy carriers is to store energy generated from sustainable but fluctuating sources such as wind or solar (photovoltaic) power. Since hydrogen can be produced directly from electrolytic water splitting, it is often considered as a good storage molecule. However, the storage and handling of hydrogen proves difficult, since it has a low volumetric energy density[1], requires high pressures and thus large amounts of energy in order to be liquefied[2] and can react violently with atmospheric oxygen. Therefore, it is desirable to convert this "green" hydrogen using chemical reactions, leading to compounds with better handling and storage capabilities that can be integrated to already existing infrastructure. For example, by reduction of CO_2, various chemicals such as methanol or methane can be generated. This has the added advantage that the amount of CO_2 in the atmosphere is reduced by fixing it in storable compounds, which is important in order to reduce global warming. The generated molecules methanol and methane are easier to handle. Methanol is liquid at ambient pressure and temperature, and methane can be stored and distributed using the already established natural gas grid. The combustion products of methanol and methane include water and carbon dioxide, which is thus regenerated and could be reduced again with hydrogen. Furthermore, methanol can serve as a feedstock for further chemical transformations, with the aim of generating more advanced energy carriers. A visualisation of this cyclic process can be found in Figure 1.1. Methanol and other products from CO_2 reduction can thus be the keystones of the energy economy in the future[3–5] and many schemes for their integration into the power and energy network are proposed.[1,6]

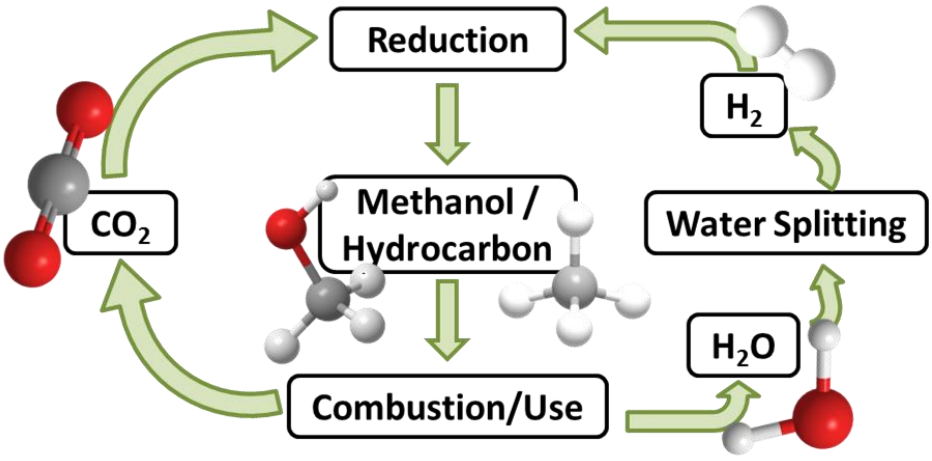

Figure 1.1: Visualisation of a sustainable cycle using methanol or hydrocarbons as platform molecules.

In this thesis, the focus is on the catalytic reduction of CO_2 over Cu/ZnO catalysts. This reaction has been of interest since the discovery of a methanol synthesis method using a ZnO catalyst in 1923.[7,8] At present, copper nanoparticles supported on alumina modified ZnO are the basis for catalysts applied in the industrial methanol production.[9] Since processes making use of the $Cu/ZnO/Al_2O_3$ catalyst are widely applied and industrially important, even small improvements on the existing system are beneficial from the viewpoints of both economics as well as sustainability.

While the reduction of CO_2 over Cu/ZnO is a well-known reaction, the exact electronic processes between the (modified) zinc oxide support and the copper particles occurring during the catalytic reaction, e.g., transfer of electrons between the components of the catalyst or the incorporation of Cu as a dopant ion, are still not fully understood. Since the electronic properties of the catalysts may influence their catalytic activity[10,11], it is of interest to gain more understanding of the processes such as charge transfer occurring at the metal/metal oxide interface under reaction conditions. This especially the case in the Cu/ZnO system, where a strong metal-support interaction was found, such that ZnO greatly enhances the catalytic activity of Cu.[12,13] The investigation of the electronic properties of Cu/ZnO catalysts is a complex undertaking since different components of the catalyst such as Cu metal, the zinc oxide support, and any promoter ions may all have an influence. Furthermore, changing the electronic structure of a catalyst may have an influence on the structural properties of the sample, and vice versa[14], which has to be taken into account when explaining their effects on catalytic performance. For the investigation of such relationships between structure, function, and catalytic properties of the catalysts, the measurement of

the conductivity under reaction conditions has been shown to be an effective tool.[15] The microwave cavity perturbation technique (MCPT) is the method of choice for such conductivity measurements, since it enables the measurement of powder catalyst samples under reaction conditions, while at the same time avoiding problems such as contact and intergrain resistances.[15] By measuring the *operando* conductivity, it is possible to relate the reactions of the gas phase occurring at the surface to the electronic properties of the materials. However, it is challenging to ascribe the conductivity to specific processes occurring in the sample, since many factors contribute to the overall conductivity of the system. For this reason, it is necessary to make use of additional characterisation techniques to rationalise the observations made by *operando* MCPT.

Doping of ZnO component is a useful way to improve the activity of the Cu/ZnO system and control its electronic properties.[16,17] Furthermore, the modification of ZnO with dopants and the resulting modification of the electronic properties of the material is of general interest since ZnO is a material with wide applications not only in catalysis, but also in fields such as optoelectronics[18], owing to it being an accessible wide-band gap semiconductor. Since it enables the alteration of its electronic properties, doping of ZnO has therefore been a topic of interest. In previous studies, both cations and anions have been employed as dopants. Of these, fluorine is an interesting dopant substance, since it acts as an anionic dopant and is highly electronegative, which can be useful in view of the modification of the electronic properties of ZnO[19]. Owing to the application as optoelectronic devices, most research on fluorine-doped ZnO has previously been focused on thin film geometries. In contrast to this, it is furthermore interesting to explore fluorine modified polycrystalline ZnO, which could be useful as a catalyst material or support in the future. To this end, direct treatment of ZnO powder with gaseous F_2 proves to be a facile synthetic route for the synthesis of the fluorine-doped derivative, which is shown to affect the structural, electronic, and surface properties of the material. Again, the MCPT technique can be employed to study the response of the conductivity of (fluorinated) ZnO to applied gas phases.

2 Background

2.1 Catalytic CO_2 reduction / reverse Water Gas Shift Reaction (rWGS)

The reduction of CO_2 is of interest in light of the global climate challenge. In nature, photosynthesis is a highly efficient process in which CO_2 is reduced to form carbohydrates. Many homogeneously catalysed reduction processes of CO_2 to products such as formate, methanol, and methane are known.[20] In these cases, methanol is generated either using indirect routes via other derivatives of CO_2 using Ru based homogeneous catalysts in the presence of H_2, or using direct routes which predominantly make use of Ru pincer complexes as the reduction catalyst.[20] It is also possible to electrochemically reduce CO_2. Here, proton-coupled electron transfer reactions result in products such as CO, and formate.[21] Electrochemical CO_2 reduction catalysts are mostly based on transition metals (e.g., Mn, Fe, or Co) with macrocyclic ligands (e.g., bipyridines, porphyrins) and produce mainly CO.[21] Photocatalytic CO_2 reduction requires the use of photosensitisers as well as sacrificial electron donors in addition to the catalyst. While many catalysts of first-row transition metals are known, most of the efficient systems require the use of expensive Ru or Ir- containing components which, along with the mostly low stabilities of the catalysts and the requirement for sacrificial reagents, disfavours the use of photocatalytic systems.[21]

For these reasons, heterogeneous catalysts are used for large-scale industrial CO_2 reduction. Using heterogeneous catalysts, methanol, dimethyl ether, formic acid, carbon monoxide, and other hydrocarbons can be generated. In comparison to homogeneous catalysts, heterogeneous catalysts have the advantage that the separation of reagents, products, and the catalyst itself is more facile, which also makes it easier to reuse them. Furthermore, such catalysts show improved stability, handling, and lower cost.[22,23]

For the catalytic reduction of CO_2 to methanol, the most relevant industrial catalyst system is $Cu/ZnO/Al_2O_3$ with a high content of Cu of ca. 60 %. [22,24] While it is possible to synthesise methanol in absence of CO_2 in the reaction feed, the yield to methanol is increased when it is present.[24]

Methanol synthesis catalysts are also active in the reverse water-gas shift reaction (rWGS)[25,26]

$$CO_2 + H_2 \rightleftharpoons CO + H_2O$$

which is the reversible generation of carbon monoxide and water by the reduction of CO_2. In contrast to methanol synthesis, which requires high pressures[24], this reaction can be performed over Cu/ZnO catalysts at ambient pressures already[27], making it especially suitable for the investigation with ambient pressure *in situ* characterisation techniques.

2.2 The Cu/ZnO catalyst system and the Cu-ZnO interface

In the Cu/ZnO catalyst system active in the reduction of CO_2, ZnO does not only serve as a support preventing the Cu nanoparticles from sintering. Additionally, there exists a strong metal support interaction (SMSI)[28–30] in form of a synergy between Cu and ZnO[13] which was shown to play an important role for the system's properties as well. The synergy presents itself as an increase in activity, e.g., towards methanol synthesis, when both Cu and ZnO are used in the catalytic system, rather than just Cu alone or on an inert support.[12] Since it was found that the catalyst's activity does not simply correlate with the amount of exposed Cu metal surface area, the interface between Cu and ZnO is thought to be of paramount importance.[31] Previous studies concerning the interaction between Cu and ZnO have employed a number of experimental techniques, including electron microscopy, X-ray diffraction, photoelectron spectroscopy, EXAFS, DRIFT-spectroscopy and diffuse reflectance optical spectroscopy.[13,32–39] Reversible changes in the sample structure upon changing the reaction feed over model Cu/ZnO catalysts were found as a further manifestation of SMSI.[30]

As an effect associated with the SMSI, the ZnO support has been found to be able to migrate onto the Cu nanoparticles, forming an ZnO overlayer or ZnO_x adspecies.[13,29,32,38] Ultimately, this behaviour can lead to alloying of Cu and Zn at the surface of the catalyst and to brass formation under reduction conditions.[30,35,40] Under varying gas atmospheres, it was found that the shape and wetting of the Cu particles changes as a consequence of variations in the concentration of interface-near oxygen vacancies.[30,36,41] These results show that the interface between Cu and ZnO is dynamically responding to the applied conditions, which has important consequences for the catalytic activity of the system. Heating the samples to reaction temperature may furthermore change the Cu particles' size and shape.[34]

2.2.1 Modifications of Zinc Oxide by doping

Doping of ZnO is in general considered as an important way to affect the performance of the Cu/ZnO catalytic system.[16,42] For many other applications of ZnO, such as photocatalysis,

electronic- or sensor devices, the control of the electronic properties of the material is likewise of crucial importance.[43,44] To this end, defects and dopants are particularly interesting, rendering the understanding of their impact on the electronic properties important. ZnO can contain a variety of intrinsic defects, including oxygen vacancies, Zn interstitials, Zn vacancies and others.[18,45] Of these, the Zn interstitials and oxygen vacancies were in the past often regarded as the cause of the observed intrinsic n-type conductivity of ZnO. [45–47] However, it is nowadays accepted that the n-type conductivity is mainly caused by impurities.[44,45] Generally, doping, e.g., by chemical methods, can be employed to evoke or control n-type or p-type conductivity of ZnO.[48] However, p-type ZnO was found to be difficult to achieve and the materials were problematic in regards to stability and reproducibility.[44,49] A main doping strategy to generate n-type ZnO or improve the n-type behaviour of ZnO is the inclusion of impurities of group III (B, Al, Ga, In).[16,50–53] Further dopants which result in n-type ZnO include interstitial hydrogen[54] or the substitution of oxygen by fluorine[55,56] or hydrogen[57].[44] Additionally and especially interesting in the context of the Cu/ZnO catalyst system, Cu can act as a dopant in ZnO, which was already discussed above. While p-type doping has been proposed in literature and is highly sought after due to expected applicability in electronic devices, a reliable preparation of such systems turned out to be challenging.[58] With respect to generating p-type ZnO, for example group I (Li, Na)[59,60] impurities substituting for Zn or group V impurities (N, P, As, Sb)[61–65], e.g., substituting oxygen, have been investigated.[45]

Cu-doping of ZnO in the CO_2 reduction catalyst has been controversially debated.[66,67]A series of papers investigated of Cu^+ ions present in the ZnO bulk and regarded this species as responsible for the activity of the catalyst.[33,37,39,68] The possibility to dope ZnO with Cu^{2+} ions has also been shown.[69–71] Another interesting aspect is the mobility of Cu ions present in the ZnO lattice as a consequence of the application of reducing or oxidising conditions. Cu from a (Cu,Zn) oxide solid solution was found to give Cu^0 particles when subjected to reducing conditions.[72] This migration was partly reversible when the sample was re-oxidised.[72] It should be noted that the solubility of Cu in ZnO is ≈ 2 at. %. If the Cu content in a Cu/ZnO sample is above the solubility limit of Cu in ZnO, it was found that reduction results in the production of two types of Cu particles (larger particles, likely from CuO reduction, and highly dispersed particles in close contact with ZnO by migration from the solid solution).[73]

Therefore, both of these kinds of Cu particles may play a role in the catalytic system. In contrast, other authors have disputed the presence of Cu ions in the ZnO lattice or their relevance for the system's catalytic activity.[66,74] Next to Cu^{+}, other active sites have been proposed, including oxygen vacancies in ZnO stabilised by a transfer of electrons to Cu, partly oxidised Cu unaffected by the support, Cu^{0} in a strong metal-support interaction with ZnO, or a Cu-Zn surface alloy.[75] In light of the possible presence of Cu ions in ZnO during reaction conditions, and the evident strong interaction between the components in reaction conditions, it is interesting to further explore their presence and influence on the electronic, structural, and catalytic properties of Cu/ZnO catalysts.

As a consequence of the influence of the electronic properties on the catalytic activity of the Cu/ZnO system, it has been shown that doping of the ZnO component can alter the catalytic properties. This is especially relevant in light of Al doping of ZnO in Cu/ZnO:Al catalysts.[42] It was shown that a major effect of doping with Al is the generation of defects in the ZnO support coinciding with a high activity in methanol synthesis.[76] An electronic modification was shown for ZnO doped with Ga^{3+} and Al^{3+} and impregnated with Cu by a decrease in the optical band gap determined by UV-vis spectroscopy an increased conductivity measured using MCPT.[16] In particular, the decrease of apparent activation energy and H_2 reaction order in the reverse water-gas shift reaction upon doping was shown to correlate with an increase in conductivity of the system, while doping with Mg^{2+} ions lowered both the conductivity and the activity in the rWGS reaction.[16]

Fluorine doped ZnO has been previously studied, mainly as a thin film in view of applications as a transparent conducting oxide and therefore with a predominant focus on the optical and electronic properties of the materials.[77,78] Additionally, the applicability of F-doped ZnO as a gas sensor was also confirmed by investigating the electrical response of the material to the exposure to, e.g.,NO_2 or acetaldehyde.[79,80] Furthermore, polycrystalline ZnO doped with fluorine has also already been studied in applications such as photocatalysis.[81] In the field of heterogeneous catalysis, fluorine treated Cu/ZnO employed as a methanol synthesis catalyst has been the focus of a recent study.[82] However, the precise function of fluorine doping for the catalytic properties of ZnO-containing catalysts continues to be elusive, and it is of interest to further study the influence of fluorine as a dopant influencing the structural, electronic, and surface properties of ZnO.

2.2.2 Charge Transfer in the Cu/ZnO system

When metallic Cu is in contact with the n-type semiconductor ZnO, a Schottky junction is generated at the interphase in between the support and the metal, which was hypothesised to enable the support to play an active role in catalysed reactions.[67,83] It is proposed that electrons may be transferred between ZnO and Cu as a result of this Schottky junction. In the active catalyst, the direction of charge transfer is often hypothesised to result in Cu^- species near the Schottky junction as a result of electrons transferred from ZnO.[30,67,84] Nevertheless, the direction of charge transfer may depend on the amount of Cu in the sample, and the sample's composition, morphology, and preparation method.[85–88] Especially the amount of Cu on ZnO may play an important role as shown by a variation of the Zn $2p_{3/2}$ binding energy, determined using photoelectron spectroscopy, when the coverage of Cu on a ZnO(0001) surface was increased up to about 1.6 monolayers.[85] Other methods employed to identify the charge transfer between Cu and ZnO include field emission measurements[88] and contact conductivity measurements[87]. It should be noted that these investigations were performed on less complex systems than can be expected to be present in real catalysts (Cu thin films rather than particles), and therefore the results cannot be directly transferred to the case of Cu/ZnO catalysts.

The conductivity of the Cu/ZnO system, besides by charge transfer, may however be also affected by intrinsic or extrinsic doping of ZnO[16,58], the oxidation state of Cu in the samples (since Cu^0, Cu_2O and CuO have different conductivities[89]), the overall amount of Cu in the sample, the preparation parameters[90], and the gas atmosphere[16,91]. Herein, the conductivity can be altered by either modifying the number of charge carriers in the system or their mobility. It is therefore important to differentiate between any contributions possibly affecting the sample conductivity in order to be able to draw any conclusions about the charge transfer direction or magnitude.

2.3 Microwave Cavity Perturbation Technique

The Microwave Cavity Perturbation Technique (MCPT) is an effective tool for the determination of electronic properties of a sample. This technique makes use of the changes in frequency and peak width of a resonant mode which in a microwave cavity. While the technique has already been pioneered in the 1940s[92], recent advances have adapted it for the measurement of samples under application of reactive and inert gases at ambient pressures

and elevated temperature.[15,93,94] Thereby, *operando* conductivity measurements of catalysts under reaction conditions are facilitated. Previous studies have thereby been able to examine the relationship between electronic and catalytic properties of catalysts active in oxidation reactions[15,95,96] as well as investigate ZnO supports and Cu/ZnO catalysts modified with dopant ions[16,96].

MCPT has several advantages over the measurement of conductivity using conventional contact measurements: The measurement of the resistances between the contact and the material under test is avoided, as is the measurement of intergrain resistances.[15] Thus, the intrinsic material properties can be probed. Specifically for the case of ZnO, the conventional contacted measurements for the conductivity or mobility of the samples have been found to be problematic due to problems with, e.g., making electrical contacts to the material as well as the above mentioned grain boundary effects.[44,45] Furthermore, it is important to stress in the context of measurement under catalytic conditions that reactivity on the metallic contacts is avoided, which becomes especially important when the conversion of the catalysts is low.

In the MCPT setup[15] it is possible to measure the dielectric properties of samples at the same time as its catalytic conversion. The sample is placed in a fixed bed reactor, through which reaction gas mixtures can flow, and the exit gas flow can be analysed using a gas chromatograph. During the measurement, the sample can be heated with a pre-heated flow of N_2 around the outside of the reactor tube.

For the simultaneous determination of the sample's dielectric properties, the changes of the electromagnetic wave inside a resonant cavity upon inserting the sample, and upon changing the conditions (such as gas phase or temperature) are utilised. The cavity consists of a cylinder made of conductive material, in this case copper which was silver- and gold plated, whose dimensions were chosen to accommodate resonant modes using radiation of an appropriate wavelength.[97]

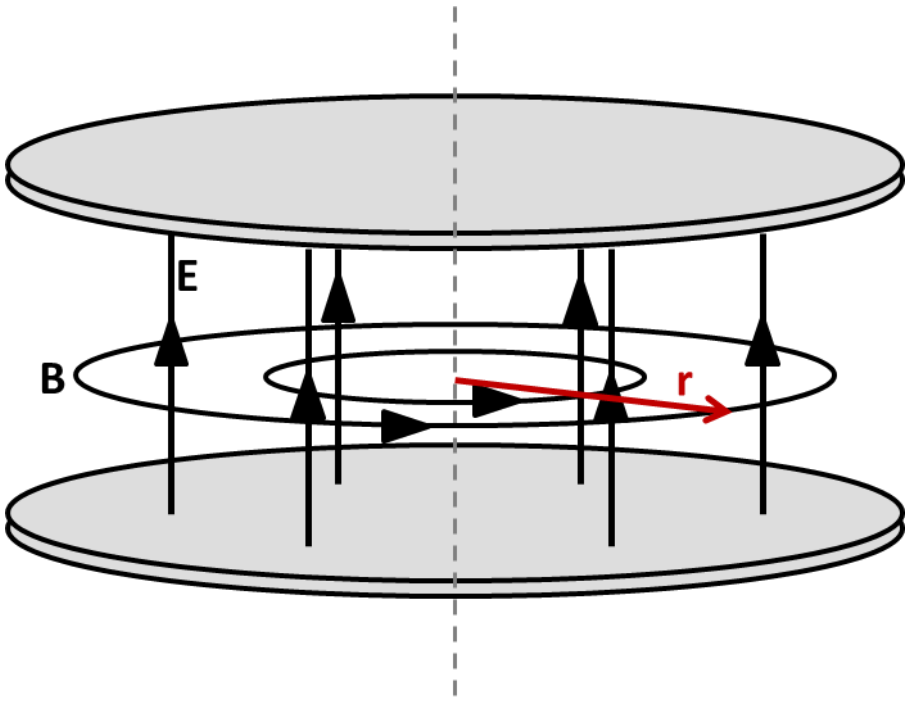

Figure 2.1: Schematic of Plate Capacitor

If we consider alternating fields in a plate capacitor (see a schematic in Figure 2.1), and recall that the electric field component will be forced to zero at the surface of a metal, the solution of Maxwell's equations for the plate capacitor gives the following expression for the electric field[97]

$$E = E_0 e^{i\omega t} J_0\left(\frac{\omega r}{c}\right)$$

where E_0 is the amplitude of the electric field of the electromagnetic wave, ω is the frequency, r is the radial coordinate of the system (see Figure 2.1, and c is the speed of light. J_0 is the Bessel function of first kind and order zero[98]

$$J_0\left(\frac{\omega r}{c}\right) = 1 - \frac{1}{(1!)^2}\left(\frac{\omega r}{2c}\right)^2 + \frac{1}{(2!)^2}\left(\frac{\omega r}{2c}\right)^4 - \frac{1}{(3!)^2}\left(\frac{\omega r}{2c}\right)^6 + \cdots$$

From Figure 2.2, it can be seen that this function oscillates, while the amplitude decreases. The first root of this function occurs at $\frac{\omega r}{c} \approx 2.405$, followed by another at 5.520 and so forth. This result indicates that, since if $J_0 = 0$, $E = 0$, the field will completely vanish at values for $J_0(\omega r/c) = 0$. At these points, the plates of the condenser could be connected, forming a cavity.

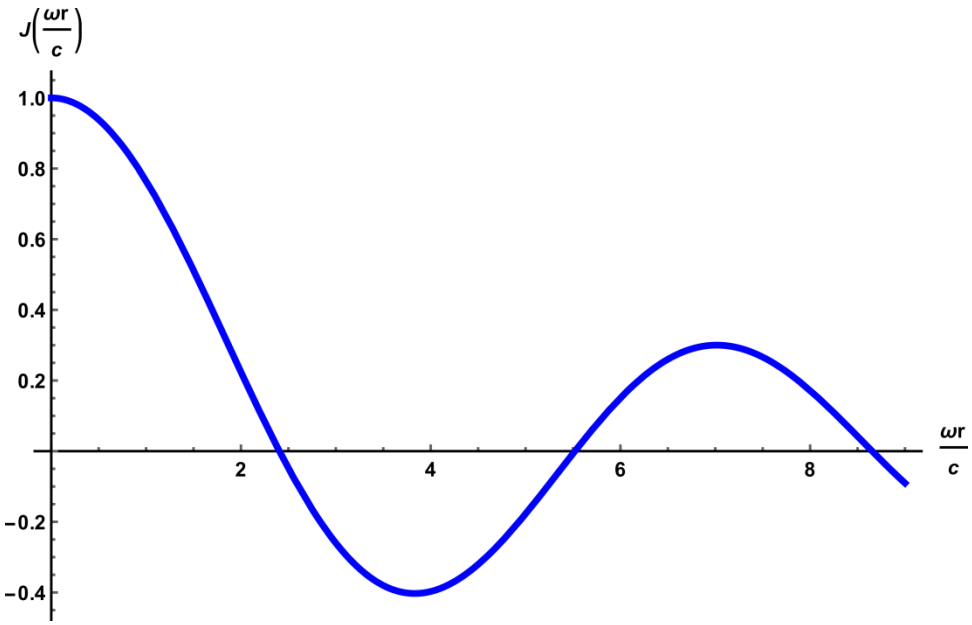

Figure 2.2: Plot of the first-order Bessel function.

The cavity resonates at the frequencies of the roots of the Bessel function, e.g.

$$\omega_0 = 2.405\,\frac{c}{r}$$

The multiple roots existing of the Bessel function thus also highlight that the cavity can accommodate several resonance modes. In this thesis, the so-called TM_{010} and TM_{020} (TM corresponds to the Transversal Magnetic modes, described using J_0) modes of cylindrical cavities are used, which have their electric field maximum in the centre of the cavity, making them especially sensitive to changes in the electronic properties of the sample, which is located at this position.[99]

Since the electromagnetic fields in the cavity will decay over time due to resistance of the cavity walls, the cavity is connected via a coupling loop to a microwave source. In case of the setup used throughout the investigations presented in this thesis, this was supplied by a vector network analyser (VNA). The fields in the cavity can be kept up by matching the frequency of the external source with the resonance frequency of the cavity.

Using the VNA which serves as both the microwave source and detector, a signal called the reflection coefficient is measured

$$\Gamma = \frac{V_-}{V_+}$$

where V_- and V_+ are the reflected and incident voltages, respectively[100]. This is plotted against the frequency. At the cavity's resonance frequencies ω_0, a resonance peak will appear. A sketch of a typical peak shape can be found in Figure 2.3.

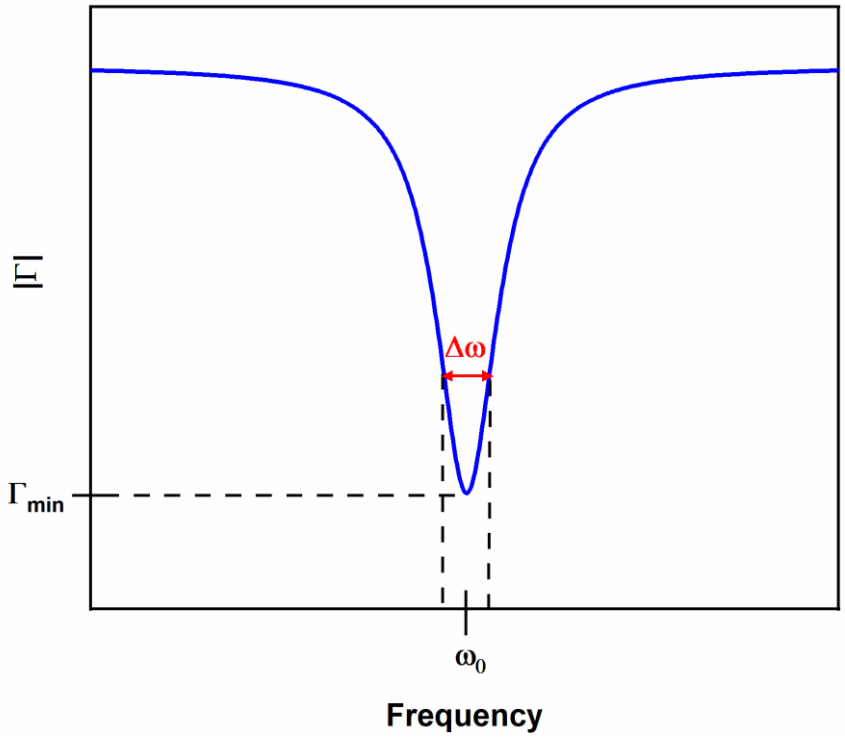

Figure 2.3: Sketch of the Resonance Peak

Apart from the resonance frequency, the resonator can be characterised by the so-called quality factor Q defined as

$$Q = \frac{\omega_0}{\Delta\omega}$$

where Δω denotes the half-power bandwidth.[100] The position of this in terms of Γ can be found in equation 2.468 in the book by Chen et al.[100] In addition to the losses resulting from the resistance of the cavity walls, there will be additional losses occurring when a sample is inserted into the electromagnetic field. Furthermore, changes in the dielectric function of the sample as a result from applied gas phases or temperature will also result in changes in the losses of the system, and hence, changes in the quality factor Q.

From this quality factor as well as the resonance frequency, assuming that the perturbation introduced into the cavity is only small, the real and imaginary part of the complex permittivity can be calculated with[100]

$$\varepsilon_{1,p} = D\left(\frac{V_c}{V_s}\right)\left(\frac{f_0 - f_s}{f_0}\right) + 1$$

$$\varepsilon_{2,p} = C\left(\frac{V_c}{V_s}\right)\left(\frac{1}{Q_s} - \frac{1}{Q_0}\right)$$

In these formulae, $\varepsilon_{1,p}$ and $\varepsilon_{2,p}$ denote the real and imaginary parts of the permittivity of the sample, respectively. The subscript p denotes that the values are not yet corrected for the fact that the samples used in this thesis are powders. V_c and V_s denote the volumes of the resonance cavity and sample, respectively, and Q_s and Q_0 the quality factors determined from a measurement with sample (subscript s) and of the system without sample (subscript 0). The frequencies f_s and f_0 are the resonant frequencies ($f_i = \omega_i/2\pi$) of the filled and empty system. The constants C and D denote calibration factors[101], which have been previously determined for the setup employed for the measurement presented in this thesis by using calibration standards of known permittivity.[96]

2.3.1 MCPT Measurement of Mixed Samples

Since catalyst samples are often powders, it is necessary to account for the packing density of the powder in the sample tube. By measuring the bed length of the sample and using the known diameter of the sample tube, the volume of the sample can be determined. Furthermore, the sample mass is determined by weighing. The fraction factor can then be determined by

$$\delta = \frac{\frac{m}{\rho}}{V_s}$$

using the density of the sample, ρ.

Many catalyst samples contain mixtures of different phases. In this case, the density of the material mixed from phases A and B can be calculated from

$$\rho = \frac{\rho_A \rho_B}{x\rho_B + (1-x)\rho_A}$$

where x denotes the mass fraction of A in the mixture. Using this fraction factor, the permittivities can be corrected to bulk values using[102,103]

$$\varepsilon_{1,b} = \left(\frac{\varepsilon_{1,p}{}^{\frac{1}{3}} - 1}{\delta} + 1 \right)^3$$

$$\varepsilon_{2,b} = \frac{\varepsilon_{2,p}}{\delta} \left(\frac{\varepsilon_{1,b}}{\varepsilon_{1,p}} \right)^{\frac{2}{3}}$$

where $\varepsilon_{1,b}$ and $\varepsilon_{2,b}$ are the bulk corrected real and imaginary parts of the complex permittivity, respectively.

Finally, the sample conductivity can be calculated by

$$\sigma = \omega \varepsilon_0 \varepsilon_{2,b}$$

where ε_0 is the vacuum permittivity.

2.3.2 The Percolation Effect in Conductivity Measurements of Composite Materials

The formulae derived above are limited to small perturbations of the cavity. In turn, special care has to be taken when measuring samples which alter the properties of the cavity significantly. Previous work at the Fritz-Haber-Institute has focused on the measurement of semiconductors with relatively low conductivity.[15,104–106] However, a wide range of catalytically active systems, such as catalysts which contain metals, or conductive supports for electrocatalysts, exhibit high conductivity, which has to be taken into account. MCPT measurements of conductive materials have several special features which have to be considered, and which we will explain in the following.

Due to absorption of the microwave, the resonance peak can be lost for such high conductivity materials. This problem can be alleviated either by reducing the amount of sample in the resonator or by dilution of the sample in a non-conductive medium. The latter method is preferable in the case of powder catalyst samples, since the handling of the sample and measurement of the sample dimensions and weight is more accurate compared to samples of minute amount. However, in composites consisting of a conductor – and a non-conductive matrix, percolation may occur.[100] This is a phenomenon arising if the particles of conductor in the inert matrix start connecting such that they form an extended network of

conducting material. Both the real and the imaginary part of the permittivity change rapidly around the percolation threshold.[100] This makes it hard to compare different conductive materials, since they might be differently close to the percolation threshold. Thus, the dilution should be chosen as such that the composite's dielectric properties are away from the percolation limit.

2.4 Dilution with an insulating material as a method to avoid percolation

Previous studies have determined the percolation limit in composites of conductive carbon materials and polymeric matrices by varying the content of carbon in the composite. DC conductivity measurements revealed the percolation limit as the location of a drastic increase of the logarithm of the conductivity versus carbon content in the sample.[107] Therefore, the need for a method usable for the measurement of highly perturbing samples using MCPT while avoiding the percolation phenomenon arises. For the development of a dilution method applicable in MCPT, mixtures of conductive carbon materials and silica as the non-conductive matrix were found to be facile to prepare and suitable for the characterisation of percolation in our experimental setup. The methodology and results underlining the principle are given in the following, while further results can be found in chapter 8.

2.4.1 Methodology

As test samples for carbon/silica mixtures, physical mixtures of commercially available carbon black as the highly perturbing, and silica as the non-perturbing materials were produced by physical mixing in an agate mortar. To ensure a good separation between carbon particles, SiO_2 was chosen in nanopowder form. These mixtures were measured in the MCPT setup, and determined the quality factor Q using an Algorithm published by Kajfez[108]. For comparison the results of finding Q using different methods, one published prior by Heine[109] and one by fitting a Lorentz peak to the experimental data of frequency versus the reflection coefficient $\Gamma = \frac{V_-}{V_+}$ and determining Q from

$$Q_o = \frac{f_0}{\Gamma_0}$$

where f_0 is the resonance frequency and Γ_0 is the full width at half maximum (FWHM) of the signal are also given. This method revealed that the creation of a dilution series is a good way to determine appropriate dilutions which are outside of the percolation regime. A more

detailed description of the experimental approach and parameters can be found in chapter 8.

The results of the investigations of Carbon Black (CB) mixed with silica can be found in Figure 2.4. When the amount of highly perturbing sample (Carbon Black) in the non-perturbing matrix (SiO_2) is increased, the resonance frequency decreases, while the peak width drastically increases.

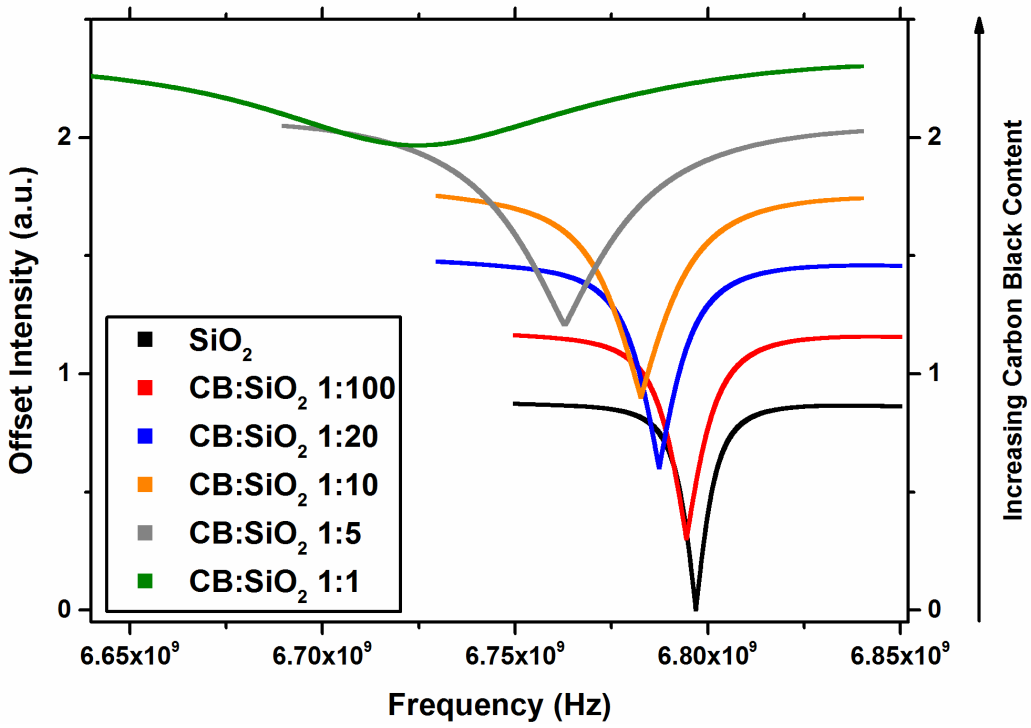

Figure 2.4: MCPT signal intensity versus frequency for the dilution series of carbon black in silica. The data have been offset for increased clarity.

The average Q_0 values for the series consisting of carbon black diluted in silica are presented in Figure 2.5. The figure compares the fit results of fitting the Lorentz peak in Origin (black squares) with Kajfez' algorithm[108] (red empty circles) and Heine's algorithm[109] (green crossed triangles). It becomes evident that up until some critical value, the quality factor vs. carbon content follows a near-linear trend, while it flattens off when the carbon content is further increased. This can be interpreted as due to percolation and an indication that the border of the quasistatic and depolarisation regime[15] was crossed. If the quality factor is to be related to the permittivity of the sample, measurements in the near-linear regime need to be considered rather than those located beyond the point where the trend flattens off (here, the sample with 51 wt.% carbon black). In doing so, measuring in the

percolation regime can be avoided. Overall, this case study presents a convenient way to determine the degree of dilution needed when comparing samples from a series of highly perturbing samples, while at the same time illustrating why the dilution itself is unavoidable.

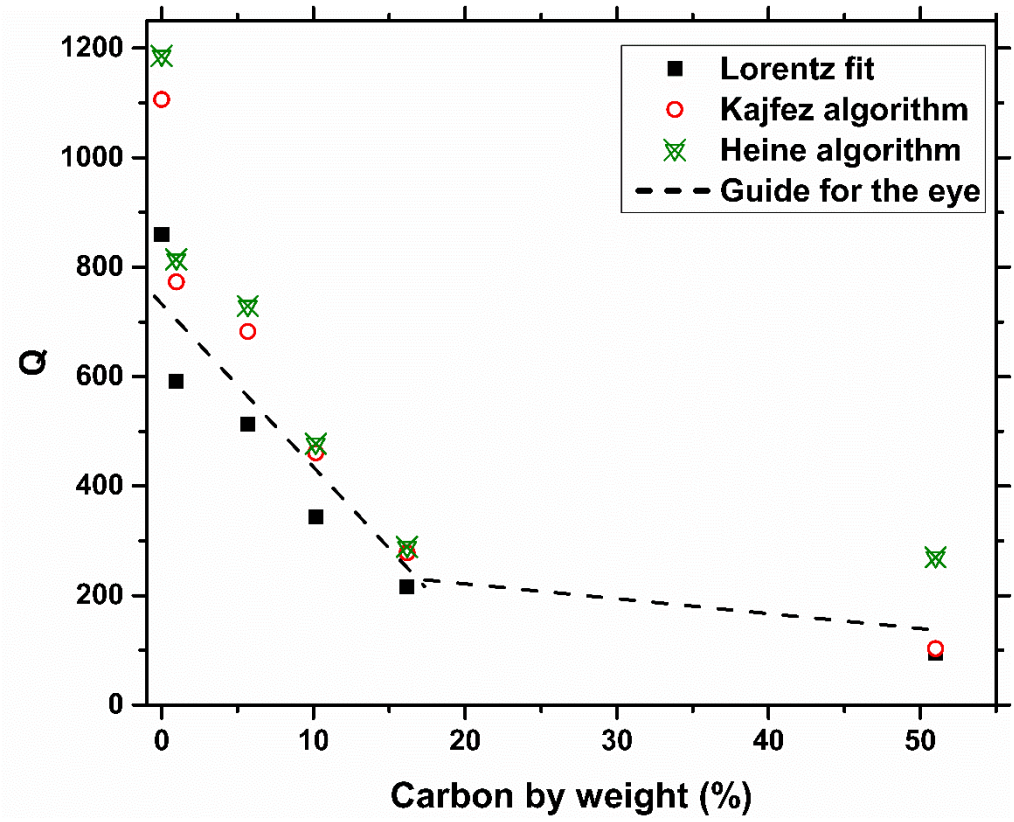

Figure 2.5: Quality factors for the carbon black dilution series for the determination of a suitable measurement regime. Different fit methods are compared. The model-free guide for the eye illustrates how the initially linear trend flattens off at high carbon contents.

The extension of the dilution method to *in situ* MCPT measurements might require additional care in the selection of the non-perturbing dilution material, because it has to be catalytically inert as well. Furthermore, treatment with reactive gases or heating/cooling may result in a higher conductivity as observed in inert gas or air at room temperature, which has already been observed for the samples in the following chapters. For this reason, it has to be ensured that none of the samples drops out of the linear response regime under any of the applied conditions. This might make it necessary to generate and measure dilution series for multiple or all samples and test them under several experimental conditions. For this reason, the dilution of Cu-containing samples in chapter 5 was evaluated for the sample with the highest Cu loading and tested in reducing conditions at the highest temperature used later during

the experiment. This ensured that the data observed for the diluted samples reflected the most conductive conditions.

3 Thesis Aims and Outline

In this thesis, the role of the interface between the components Cu and ZnO in Cu/ZnO samples active in the reverse water-gas shift reaction (rWGS) is investigated. Here, a focus lies on the modification of the ZnO component, e.g., by using copper or fluorine as dopant ions. Doping of ZnO is of interest not only in catalysis, but also for numerous other applications, since it enables the alteration of not only the structural, but also the electronic properties of the material.

The use of varied Cu/ZnO samples which differ in their synthetic background and their Cu loading enabled the study of their properties and catalytic performance as a function of these parameters. Furthermore, the applicability of such samples as models for the industrial catalysts is examined. The results of these investigations are presented in chapter 5. To gain an understanding of the interface between Cu and ZnO, the Cu content of the samples is kept low. Lowering the Cu loading is furthermore a common strategy employed for the generation of model catalysts, since it can enable the use of certain experimental techniques, as well as lower the system's complexity and shed a focus on specific aspects of the catalyst system. By reducing the amount of Cu in the samples, the effects resulting from metallic Cu nanoparticles present in the industrial catalyst can be minimised. Thus, effects of the interface of Cu and ZnO can be studied. To get insight into the effect of Cu on ZnO, the content of Cu in the samples is varied. Thereby, the presented work effectively forms a bridge between studies on (doped) ZnO and Cu/ZnO catalysts, which contains a higher amount of metallic Cu in its active state. By comparing samples formed by two synthetic approaches, namely impregnation and coprecipitation, two common methods of generating model catalysts are investigated as well as their ability to serve as models for the industrial catalyst. The different synthetic techniques also allow for the comparison between a more phase-separated precursor system (generated by impregnation) and a system based on a Cu,Zn oxide solid solution (generated by coprecipitation).

To fulfil the aim to gain more insight in the properties and the applicability of these samples as model catalysts the samples' structural, electronic, and catalytic properties are studied by investigating trends in properties as a function of the catalyst loading and the synthetic approach. It is shown that the two synthetic methods impregnation and coprecipitation here

produce samples with different properties. Furthermore, the samples' properties and performance are shown to vary as a consequence of differences in Cu content.

In particular, *operando* conductivity measurements using MCPT[15] were used to correlate changes of the electronic properties of the catalysts with their catalytic performance, in line with previous investigations using this technique.[95,96,105,106] The different components of the catalyst, including metallic Cu nanoparticles, the ZnO support, and any promoter ions will all influence the electronic and structural properties of the catalyst and contribute to the overall catalytic performance of the system, making the analysis of these processes demanding. To be able to rationalise the results obtained by MCPT, the samples' structural and electronic properties are therefore further probed using a mixture of inert transfer and *in situ* techniques. Through these means, the structure and electronic properties of the samples in their reduced state or under reaction conditions is studied and related to their activity in the rWGS reaction. The samples' catalytic performance in the reverse water-gas shift reaction and their suitability as models for the technical Cu/ZnO-based catalyst is investigated.

Even though synthesis by impregnation would ideally lead to fully phase-segregated CuO/ZnO precursors, the mobility of Cu ions in ZnO can allow the migration of Cu ions into the ZnO lattice[72,73]. For this reason, chapter 6 presents a detailed characterisation of the structure and electronic properties of one sample from the series generated by impregnation. The sample with 1.06 wt.% loading has a Cu content below the solubility limit in ZnO[110], which provides the possibility of the presence of reducible Cu species in the support. Using a combination of inert transfer techniques (e.g., electron paramagnetic resonance (EPR) and electron microscopy) and *in situ* MCPT, the presence and reversible reducibility of these species is shown. Thus, the impact of Cu-doping of ZnO on the properties of the material is elucidated.

Apart from cationic doping of ZnO with, e.g., Cu or Al ions, ZnO can also be doped with anions, providing further ways to affect the materials' structural and electronic properties. In chapter 7 we therefore investigate the use of fluorine as a dopant for ZnO. The aim of this was to provide a facile way to modify ZnO using the application of gaseous F_2, which resulted in the incorporation of fluorine to different degrees, depending on parameters such as F_2 partial pressure and duration of the gas application. The chapter presents the detailed characterisation of the resulting samples in view of their structural, electronic, and surface

properties. This involved, e.g., the investigation of the interaction of the fluorinated and non-fluorinated ZnO samples with H_2 using MCPT.

A summary of the findings presented in this thesis as well as final conclusions can be found in chapter 4.

4 Summary and Conclusions

For heterogeneous catalysts, the relationship between the structural and electronic properties and the corresponding catalytic properties is of crucial importance for a rational design of the catalytic systems. A large amount of work focused on understanding the catalysts' surface properties. However, there is solid evidence that the bulk of the catalyst material is not only altered, e.g., with respect to its electronic properties when applying catalytic turn over conditions, but also that these changes are correlated to the catalytic performance of the catalysts.[111,112] This calls for methods capable of analysing these properties under *in situ* conditions, e.g., the microwave cavity perturbation technique (MCPT). Within this thesis, *operando* MCPT was applied to doped ZnO samples and to Cu/ZnO catalysts, which is the system currently used in industry to produce methanol and considered an important system within the framework of CO_2 activation.

The industrially used catalyst for this reaction is a complex system characterised by a large Cu loading (> 50 mol%) and the presence of electronic and structural promoters, rendering a detailed investigation of the Cu/ZnO interface and the role of Cu in the ZnO phases challenging. Therefore, model catalysts are commonly used in order to simplify the system, lower the system's complexity, and facilitate the use of some additional experimental techniques. A common feature of Cu/ZnO model catalysts is that their Cu content is often lower than is the case in the industrial system. For these reasons, within this thesis two series of catalysts with Cu loading up to 9.65 % were investigated. The samples were generated using two distinct synthetic approaches, namely impregnation and co-precipitation, which are both common methods used for the synthesis of Cu/ZnO model catalysts. Furthermore, this provided the opportunity to study the system from two sides: impregnation results in mostly separated CuO and ZnO phases, of which some of the Cu may migrate into the ZnO upon activation. On the other hand, coprecipitation can yield a system in which Cu forms part of the ZnO structure in form of a (Cu,Zn)oxide solid solution, with some of the Cu migrating out of the structure and being reduced under the activation treatment. A visualisation of this is given by the scheme in Figure 4.1. In the following, the two sample series are termed Cu-C series (coprecipitation series) and Cu-I series (impregnation series), respectively. Individual samples are denoted by the XRF-determined CuO content of the sample and their synthesis

history (e.g., 7.28Cu-I for the sample with 7.28 wt. % CuO content synthesised by impregnation).

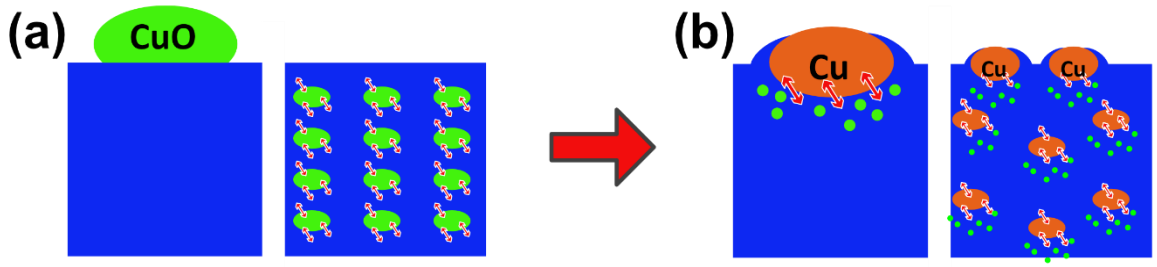

Figure 4.1: Scheme visualising the synthetic strategies employed for the Cu/ZnO catalysts employed in this thesis. (a) reflects the state of the samples before activation and (b) after activation in reducing gas feed. The left part of each image represents the samples generated by impregnation, while the right hand side features the samples synthesised by coprecipitation. The different colours represent different parts of the model catalysts; blue – ZnO, green – CuO/Cu ions, orange – metallic copper.

Furthermore, since they contain relatively low amounts of Cu only, these systems are suitable to be investigated by MCPT. This technique requires samples with low to moderate losses in the microwave regime, a condition which is not met by the industrially used methanol synthesis catalyst. Since the methanol synthesis reaction necessitates the use of elevated pressure, the reverse water-gas shift (rWGS) reaction, which occurs already at ambient pressure, was employed to probe the correlation between catalytic and electronic properties of the systems. The interpretation of these measurements relies on additional information, e.g., on the structural properties of the system. These were obtained by employing, e.g., XRD, STEM-EDX, Cu surface area measurements, EPR, and DR-UV-vis spectroscopy. For the samples discussed in this thesis, the situation is complicated by the fact that the catalysts change significantly if exposed to ambient conditions. This required the use of either *in situ* or at least inert transfer techniques to study the Cu/ZnO system.

The investigated samples differed in their properties, both dependent on their synthetic history (differences between the samples generated by impregnation and by coprecipitation, respectively), and on their Cu content (differences between samples with lower and higher Cu content, respectively). The various techniques used to study the samples revealed different sample properties, which changed with Cu loading and between the synthesis techniques to a varying degree. In the following, some selected results highlighting these differences between the samples are presented.

The two series of samples synthesised by impregnation and coprecipitation, respectively, showed significant differences in the behaviour of the lattice parameter *c* as a function of Cu content (see Figure 4.2). The expansion of *c* observed for the case of the coprecipitated samples can be interpreted as an incorporation of Cu ions into the ZnO lattice. This behaviour is not observed for the impregnated samples. This highlights the different synthetic background and the separation of CuO and ZnO in the precursor structure. Overall, the lattice parameter *c* thus highlights the differences of the two different synthetic strategies, and also shows that there are significant differences in the coprecipitated series as a function of the Cu loading, thus separating samples with low and high Cu content.

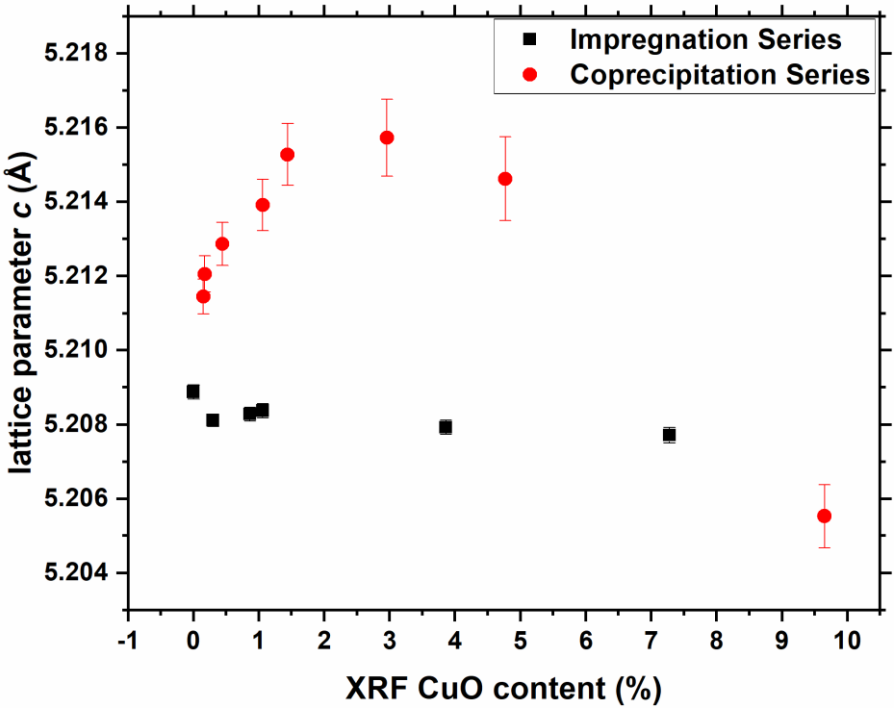

Figure 4.2: Lattice parameter *c* of the CuO/ZnO precursors generated by impregnation and coprecipitation.

Further information on the speciation of the Cu species within the two series of catalysts can be obtained from an analysis of TEM data. The EDX mapping and line scan analysis (see Figure 4.3) shows that the size of Cu particles increases with increasing loading. To exemplify this, two samples with respectively low and higher loading (1.06 % and 7.28 %) and synthesised by impregnation are shown in Figure 4.3 (a) and (b). Therefore, differences within the impregnation series can be found, which result from differences in the samples' Cu content. While the samples with low loading appeared quite similar between the two synthesis methods, the difference between the two approaches became evident when considering the

samples with the highest Cu loading. The impregnated sample 7.28Cu-I contained overall larger Cu agglomerates than 9.65Cu-C (see Figure 4.3 (c) and (d)). This evidences the differences in the samples, but here resulting from their synthetic history. Furthermore, a portion of the Cu is located outside of the particles. The fraction of the latter type depends both on loading and the synthesis method. Overall, the dispersion of Cu increases with decreasing Cu content, and for samples generated by coprecipitation in comparison to impregnation.

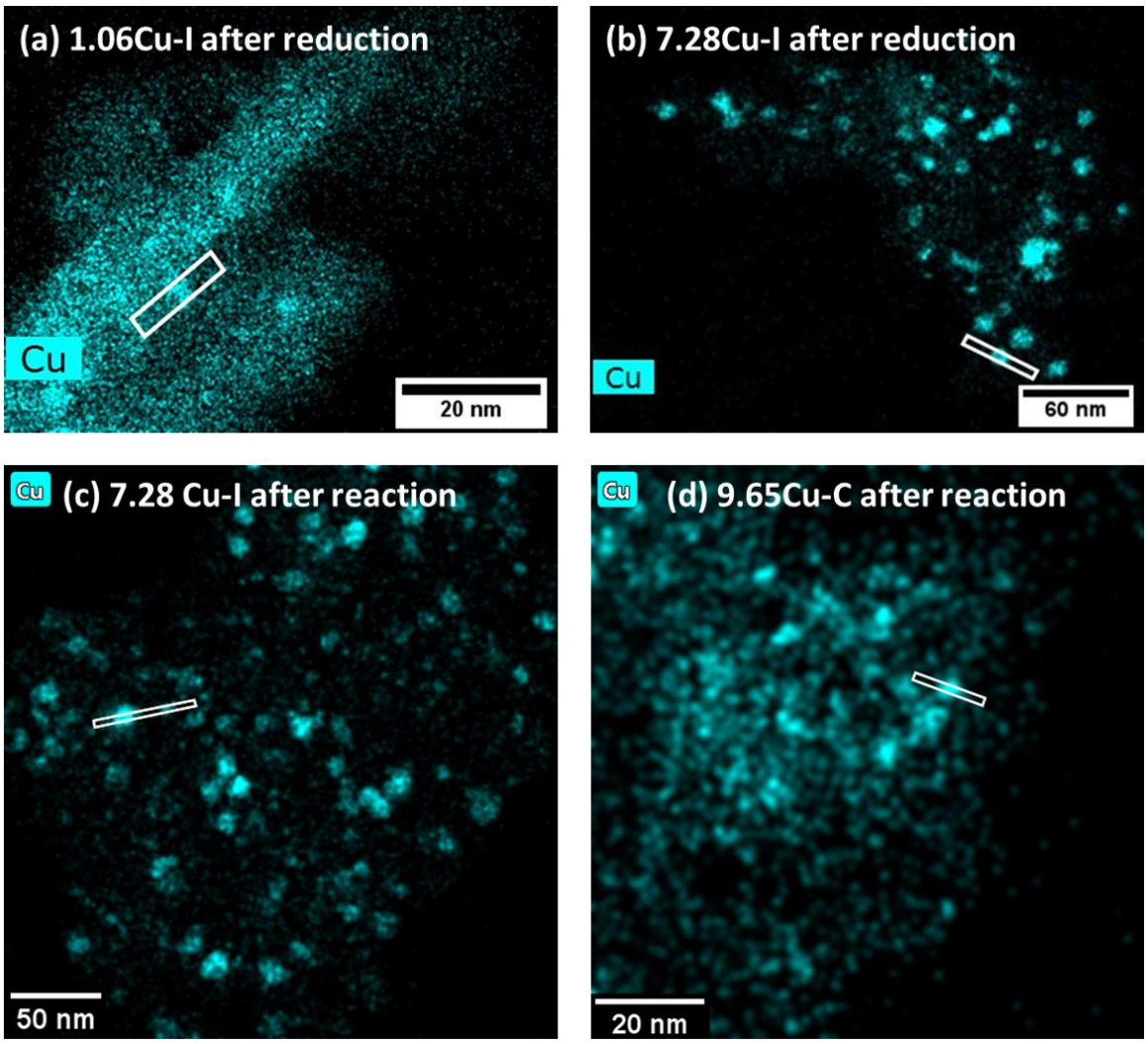

Figure 4.3: Comparison of EDX Cu-maps of samples generated by impregnation (a-c) and coprecipitation (d) in their activated state. Samples with low (a) and higher (b) loading generated by impregnation are compared, as well as the highest loaded samples synthesised by impregnation and coprecipitation, respectively (c and d).

The catalytic activities of the Cu/ZnO were investigated and the two sample series were compared. By normalising the measured activity by various means, e.g., the BET surface area of the samples or the Cu content, different trends were observed. When normalising by the Cu mass, the CO production rates of the catalysts increased with loading up until a certain

point, then decreased again until reaching a plateau when the Cu content in the samples was increased further. The point of the maximum as well as how much the rates decreased towards the higher loading end differed between the two sample series. These results indicate that a high dispersion of the Cu throughout the sample and thus a large interfacial contact, which are more prevalent in the coprecipitation series, are in general beneficial. To support this finding, the apparent activation energies for the rWGS reaction were determined and it was found to decrease with higher Cu loading and be lower for the coprecipitated samples as compared to the impregnated ones. Overall, the coprecipitation strategy leads to a more efficient use of the Cu present in the sample. Again, these findings highlight that the Cu/ZnO samples show differences also in their catalytic performance as a result of the synthetic strategy applied, but also depending on their Cu content. Notably, the 9.65Cu-C sample which does not result in an expansion of the lattice parameter *c* still follows the trends in catalytic activity generated by the other samples in the same series. This leads to the interpretation that it is not necessarily the Cu incorporated in the ZnO lattice which is responsible for the higher activity exhibited by the coprecipitated samples compared with the samples synthesised by impregnation. Instead, the strongly embedded Cu in these catalysts, representing the Cu-ZnO interface, appears to be more important for the catalytic activity.

The differences in the interaction between the catalyst components may also manifest themselves as changes in the samples' electronic properties. To this end, the optical band gap and the conductivity of the catalysts were investigated. The optical band gap might be altered due to Cu incorporation into the ZnO matrix, rendering DR-UV-vis spectroscopy a tool to investigate the extent of Cu incorporation into the ZnO lattice. By determining the band gap *in situ* under reducing conditions, it was found that the optical band gaps of the reduced samples decrease with increasing Cu content. Overall, the band gaps decreased with increasing content of Cu in the samples. (see Figure 4.4), This indicates that ZnO was intrinsically modified by the addition of Cu leading to the generation of states in the band gap of ZnO.

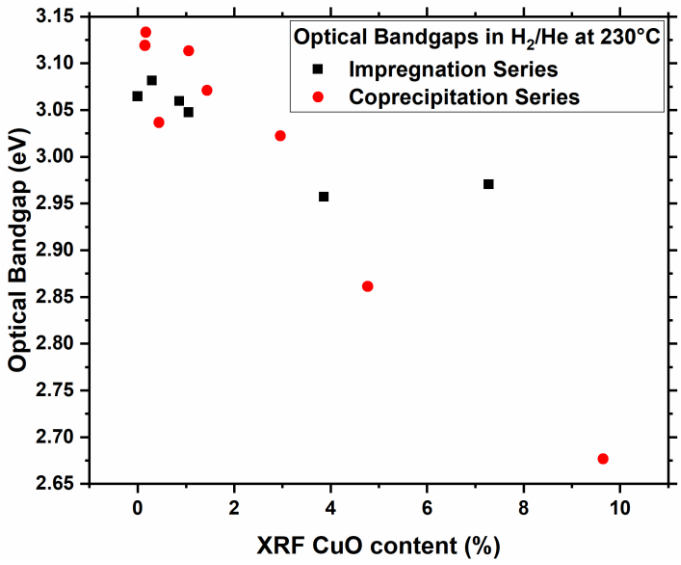

Figure 4.4: Optical Bandgaps of the samples generated by impregnation and coprecipitation in their activated state (in H_2/He at 230°C).

Significant differences between the impregnation and coprecipitation synthesis strategies were observed when the conductivity of the active catalysts was measured under reaction conditions. Strikingly, while an increase in the H_2 proportion of the rWGS feed resulted in an increase in both the conductivity as well as the activity of the catalysts generated by impregnation, coprecipitation yielded samples whose conductivity decreased with increasing H_2 content, even while the activity still increased (see Figure 4.5). Again, a decisive difference in the qualitative behaviour of the samples depending on their synthesis method was found, which points at differing interactions between Cu and ZnO.

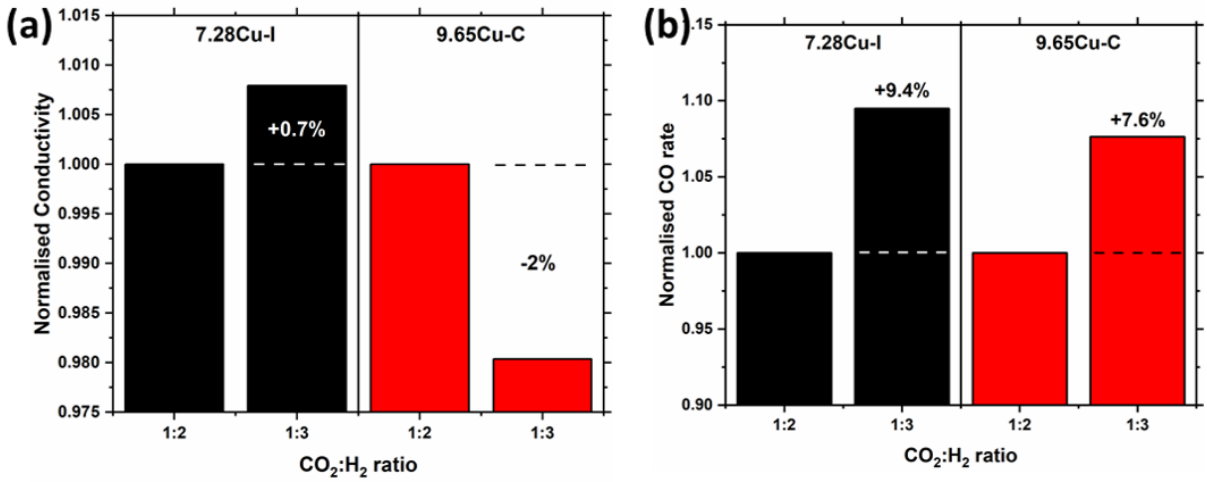

Figure 4.5: relative changes in (a) the MCPT-derived conductivity and (b) the CO rates of the highest-loaded samples in each series in two reaction feeds (1:2:7 and 1:3:6 CO_2:H_2:N_2)

A further important characteristic of the samples' performance in the reverse water-gas shift reaction is their apparent activation energy. These are presented in Figure 4.6 along with a dashed line which represents the activation energy (ca. 60 kJ/mol) that could be expected for a binary Cu/ZnO catalyst with industrially relevant Cu/Zn ratio ≥ 1. It is firstly notable that there is a variation of the apparent activation energy depending on the Cu content of the samples, both in case of the coprecipitated as well as the impregnated samples. In both series, the activation energy generally decreases with increasing Cu content (with 1.06Cu-C forming an exception). Additionally, the activation energies of the impregnated samples were found to be higher than those of the coprecipitated samples, again presenting a difference in the samples depending on how they were synthesised. Most importantly, it should be noted that the apparent activation energies observed for all investigated Cu-containing samples was well above 60 kJ/mol which is the expected value for Cu/ZnO catalysts with a Cu/Zn ratio of above 1, as is the case in the industrially applied catalyst. This means that none of these samples with low Cu content can reasonably stand as a model for the technical system, regardless of their Cu content or their synthetic history. This finding underlines the importance of verifying the comparability of the performance of catalysts to the industrial catalyst, before conclusions based on the model samples' characteristics may be transferred or assigned to the technical system.

In summary, the characterisation as well as the analysis of the catalytic performance of the Cu/ZnO samples presented in this thesis revealed that their properties vary depending both on the method used to synthesise them as well as their Cu content. This, along with the comparatively high apparent activation energies which was found to be far higher than could be expected for Cu/ZnO systems with a Cu content comparable to the industrial catalyst, demonstrated that they are unsuitable as model catalysts. It was thus shown that, in case of the Cu/ZnO catalyst system, the complexity of the catalyst may not be arbitrarily reduced, e.g., by using samples with a significantly lower Cu content, when a sample should still function as a model for the technical system. It should be noted therefore that the verification of a comparable performance is crucial when conclusions on an industrial system are to be drawn from an analysis of a model catalyst.

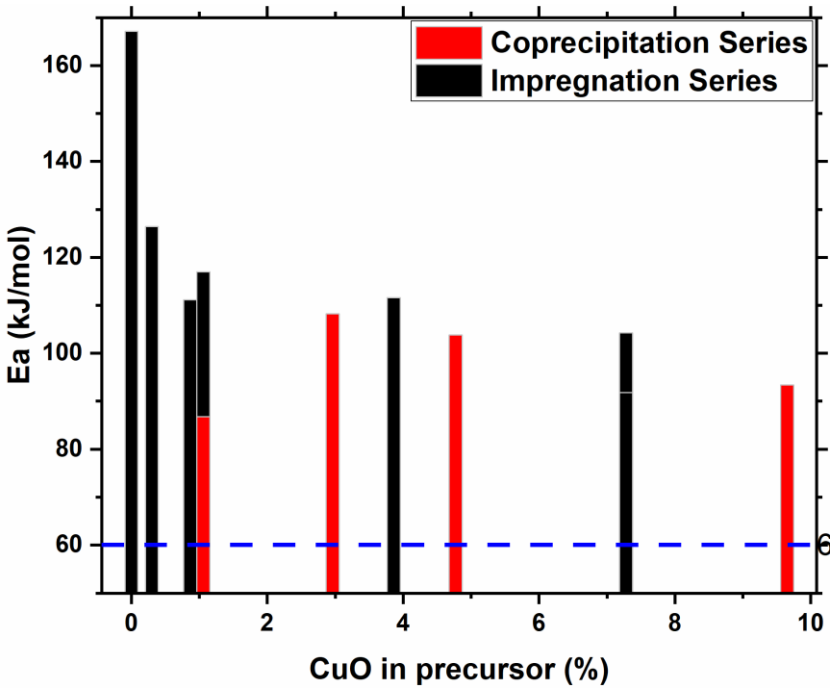

Figure 4.6: Apparent activation energies of Cu/ZnO samples towards the reverse water-gas shift reaction, determined in an 8-fold parallel reactor setup. A (blue dashed) line at 60 kJ/mol was added for comparison.

While, as explained above, the samples with low Cu content were not useful as models for an industrially applied Cu/ZnO catalyst, nevertheless interesting characteristics were observed, of which some (e.g., an expansion of the lattice parameter *c* highlighted the mobility of Cu ions in the ZnO lattice. Since the catalytic performance of those samples was not comparable to the technical catalyst, it may be assumed that this feature does not play an important role for the performance of the industrial system. However, it is an interesting feature present in some of the investigated samples and therefore warranted a further investigation.

Further characterisation of the sample with 1.06 wt.% loading generated by impregnation provided a way to better understand the modification of ZnO by the addition of Cu. While the impregnation synthesis method could be expected to result in phase-separated CuO and ZnO, the mobility of Cu in ZnO rendered it possible for Cu ions to migrate into the ZnO support during calcination or activation. The specific sample was chosen due to its relatively low Cu content, which was below the solubility limit of Cu^{2+} ions in ZnO. By detailed characterisation, it was possible to confirm the incorporation of Cu^{2+} in ZnO in case of this sample. These Cu^{2+} ions are reducible, e.g., by application of hydrogen containing atmospheres at elevated temperatures. This was confirmed by EPR spectroscopy of the sample before and after reduction, as well as after re-oxidising it by exposure to air. Through these results, and by *in*

situ MCPT measurement under reducing and oxidising conditions, it was shown that the incorporated Cu^{2+} ions are reversibly reduced and oxidised, and that the sample in the reduced state is not stable when it is removed from the reducing conditions (or indeed, reaction conditions) to oxygen-containing gas or even inert conditions. This is evident through a decrease in conductivity in inert feed after reduction, and as a slow recreation of the EPR signal associated with the isolated Cu^{2+} sites. These findings highlight that the Cu/ZnO system is dynamic. Likewise to the results obtained for the Cu-C and Cu-I series, the results gained through this further characterisation can give insight into the Cu/ZnO interface in catalysts. Further experimental investigations could include *in situ* EPR measurements, which would facilitate the direct investigation on the dynamics of the creation and loss of the signals related to the isolated Cu^{2+} sites.

For doped compounds, X-ray diffraction often provides a way to confirm the presence of dopant ions in the lattice. If dopant ions are present in the interstitial sites of the lattice, or if some ions on the lattice sites are substituted by dopant ions of different size, changes in the lattice parameters can result. For this reason, inert transfer XRD of the reduced 1.06 wt.% sample was used. The resulting diffractogram was fitted in two different ways, one fit assumed the presence of metallic Cu particles, and one assuming that ZnO was the only phase present in the sample. Both fits yielded equally good agreements between the fit and the measured data, so it is not possible to conclude on the presence of metallic Cu particles from this technique. From the fit assuming ZnO as the only crystallographic phase, the lattice parameters did not show deviations from pure ZnO. The reason for this is likely that the content of Cu^{2+} ions in the lattice is very small in the case of this sample, combined with the fact that the ionic radii of the dopant ion is rather similar to that of the substituted Zn^{2+} ion, so that changes to the lattice parameter can be expected to be small. This finding highlights that even though the presence of Cu^{2+} ions in the ZnO lattice could not be found through XRD measurements, they can still be present, as was evidenced by EPR.

The modification of ZnO was further studied, this time using an anionic modifier, namely fluorine, instead of a cationic one. This was achieved by treating polycrystalline ZnO with gaseous fluorine. The extent of modification and the resulting effects can be controlled by varying the amount of fluorine with which ZnO is treated. Not only the structural and electronic properties of the material were affected, but also the surface acidity/basicity and

the way ZnO interacts with an applied gas phase. The surface acidity and basicity were investigated using IR-spectroscopy and microcalorimetry using NH_3 and CO_2 as probe molecules, respectively. The interaction of ZnO with applied gas phases also manifested itself in differences in the samples' conductivity. The differences in response to reducing and oxidising gas atmospheres are visualised in Figure 4.7. Here, it becomes evident that the F_2-treated sample containing about ten times less fluorine (ZnO_F1), which was shown to be phase-pure using XRD and electron microscopy, showed the largest conductivity response to the application of a reducing gas atmosphere. While the conductivity of the sample treated at a higher partial pressure of fluorine (ZnO_F10) still showed a larger conductivity increase than pure ZnO, the effect was much less pronounced. This can be explained by a phase separation in this sample, which was shown to contain a significant amount of ZnF_2 as a by-phase. Another interesting result from this investigation is the reversibility of the conductivity increase when the samples are subsequently treated with oxygen. Overall, the response of the materials to the applied gas phase highlights that fluorine doping of ZnO greatly increases the ability of the material to activate and chemisorb H_2 which can have significant implications for the application of the materials in catalysts. Therefore, it will be interesting to further investigate fluorine-modified ZnO, especially with regards to its use in Cu/ZnO based catalysts for CO_2 hydrogenation reactions.

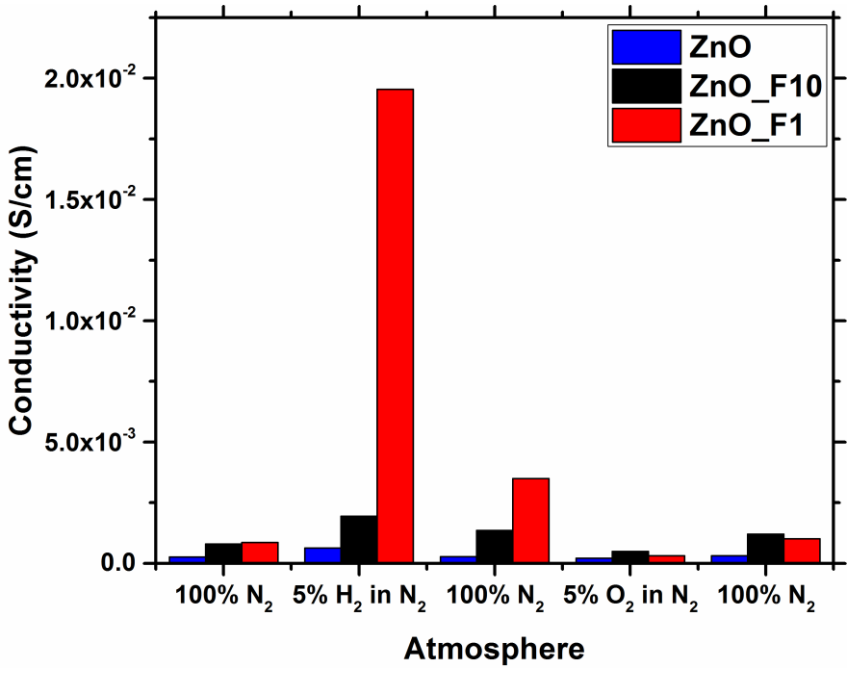

Figure 4.7: Comparison of the conductivities of ZnO and fluorine-treated ZnO in different gas phases. The sequence of the experiment is also represented by the abscissa.

All in all, this thesis provided results important for the research of Cu/ZnO catalysts, which are commonly applied in the reduction of CO_2. The investigations of the structural, electronic, and catalytic properties of two series of Cu/ZnO catalysts active in the rWGS reaction showed that there exists an intrinsic modification of the ZnO support, which was further characterised by analysing the sample with 1.06 wt.% loading synthesised by impregnation in more detail. It was thus shown that isolated Cu^{2+} ions are present in the ZnO support, which are reversibly reducible. The synthetic approach and thereby the variation in the Cu-ZnO interface were shown to not only critically affect the activity of the catalysts, but also the qualitative behaviour of the conductivity (measured by MCPT) as a marker for the samples' electronic properties. It should be noted that the many different characterisation techniques employed in the study of these samples are differently sensitive to the changes in the samples resulting from the Cu loading variation or the synthetic history. For example, the MCPT response and the catalytic activity proved to be sensitive to even small changes in the applied gas phase.

Crucially, the catalytic properties, specifically the apparent activation energies towards the rWGS reaction, were found to differ from the expectation for Cu/ZnO samples with industrially relevant Cu content. This disqualifies the samples investigated in this thesis from the use as model catalysts for the industrial catalyst.

While the samples are not useful for the application as model catalysts, they nevertheless demonstrated interesting properties. These properties include, for example, some catalytic activity in the reduction of CO_2, or a gas-phase dependent change in conductivity, which would be interesting to explore further in view of a possible application as catalysts or gas sensing materials. The same is the case for the fluorinated ZnO samples, whose catalytic performance and stability (e.g., against hydrolysis), was not yet studied, but whose surface properties and gas-phase dependent conductivity response could be changed by varying the degree of fluorination.

As a final summary, the findings presented in this thesis demonstrate that the properties, e.g., the catalytic, electronic, or surface properties, of the ZnO-based samples can be varied by varying their composition (Cu content, F content) or the way they are synthesised (impregnation, coprecipitation). This opens up possibilities for the control and adjustment of the desired characteristics of Cu/ZnO or ZnO – based materials which may prove useful in applications such as catalysis or gas sensing. Nevertheless, it has to be stressed that while it

is a common strategy to use Cu/ZnO samples with low Cu content, and generated by impregnation or coprecipitation as models for the industrial CO_2 hydrogenation catalyst, the samples presented in this work do not function as such, since their catalytic properties (e.g., the apparent activation energy) were shown to be much different from samples with an industrially relevant Cu/Zn ratio. In general, it is important to note that if conclusions or findings are to be transferred to industrial catalyst systems, it has to be ensured that model samples have comparable catalytic properties.

Bibliography Chapters 1 to 4

1 R. J. Pearson, M. D. Eisaman, J. W. G. Turner, P. P. Edwards, Z. Jiang, V. L. Kuznetsov, K. A. Littau, L. Di Marco and S. R. G. Taylor, *Proc. IEEE*, 2012, **100**, 440–460.

2 R. Coontz and B. Hanson, *Science*, 2004, **305**, 957.

3 F. Asinger, *Methanol - Chemie- und Energierohstoff*, Springer, Berlin; Heidelberg; New York, 1st editio., 1986.

4 G. A. Olah, *Angew. Chem. Int. Ed. Engl.*, 2005, **44**, 2636–9.

5 G. A. Olah, A. Goeppert and G. K. S. Prakash, *J. Org. Chem.*, 2009, **74**, 487–98.

6 R. Schlögl, *Angew. Chemie - Int. Ed.*, 2015, **54**, 4436–4439.

7 K. C. Waugh, *Catal. Today*, 1992, **15**, 51–75.

8 Patent US 1569775, 1926, 1–2.

9 J. B. Hansen and P. E. H. Nielsen, in *Handbook of Heterogeneous Catalysis*, ed. G. Ertl, Wiley VCH, 2., 2008, vol. 2, pp. 2920–2949.

10 G.-M. Schwab, *Angew. Chemie*, 1955, **67**, 433–438.

11 M. Eichelbaum, M. Hävecker, C. Heine, A. M. Wernbacher, F. Rosowski, A. Trunschke and R. Schlögl, *Angew. Chem. Int. Ed. Engl.*, 2015, **54**, 2922–6.

12 R. Burch, R. J. Chappell and S. E. Golunski, *Catal. Lett.* , 1988, **1**, 439–444.

13 M. Behrens, F. Studt, I. Kasatkin, S. Kühl, M. Hävecker, F. Abild-Pedersen, S. Zander, F. Girgsdies, P. Kurr, B.-L. Kniep, M. Tovar, R. W. Fischer, J. K. Nørskov and R. Schlögl, *Science*, 2012, **336**, 893–7.

14 G. J. Hutchings, *Catal. Lett.* , 2001, **75**, 1–12.

15 M. Eichelbaum, R. Stösser, A. Karpov, C.-K. Dobner, F. Rosowski, A. Trunschke and R. Schlögl, *Phys. Chem. Chem. Phys.*, 2012, **14**, 1302–12.

16 J. Schumann, M. Eichelbaum, T. Lunkenbein, N. Thomas, M. C. Álvarez Galván, R. Schlögl and M. Behrens, *ACS Catal.*, 2015, 3260–3270.

17 M. Behrens, S. Zander, P. Kurr, N. Jacobsen, J. Senker, G. Koch, T. Ressler, R. W. Fischer and R. Schlögl, *J. Am. Chem. Soc.*, 2013, **135**, 6061–6068.

18 M. D. McCluskey and S. J. Jokela, *J. Appl. Phys.*, , DOI:10.1063/1.3216464.

19 A. Sanchez-Juarez, A. Tiburcio-Silver, A. Ortiz, E. P. Zironi and J. Rickards, *Thin Solid Films*, 1998, **333**, 196–202.

20 K. Dong, R. Razzaq, Y. Hu and K. Ding, *Top. Curr. Chem.*, 2017, **375**, 1–26.

21 A. Rosas-Hernández, C. Steinlechner, H. Junge and M. Beller, *Top. Curr. Chem.*, 2018, **376**, 1–25.

22 W. Wang, S. Wang, X. Ma and J. Gong, *Chem. Soc. Rev.*, 2011, **40**, 3703–27.

23 M. Mikkelsen, M. Jørgensen and F. C. Krebs, *Energy Environ. Sci.*, 2010, **3**, 43–81.

24 K. C. Waugh, *Catal. Lett.* , 2012, **142**, 1153–1166.

25 M. Saito and K. Murata, *Catal. Surv. Asia*, 2004, **8 (4)**, 285–294.

26 G. Centi, E. A. Quadrelli and S. Perathoner, *Energy Environ. Sci.*, 2013, **6**, 1711–1731.

27 J. Schumann, Dissertation, *Cu , Zn-based catalysts for methanol synthesis*, Technische Universität Berlin, 2015.

28 S. Zander, E. L. Kunkes, M. E. Schuster, J. Schumann, G. Weinberg, D. Teschner, N. Jacobsen, R. Schlögl and M. Behrens, *Angew. Chemie - Int. Ed.*, 2013, **52**, 6536–6540.

29 R. Naumann d'Alnoncourt, X. Xia, J. Strunk, E. Löffler, O. Hinrichsen and M. Muhler, *Phys. Chem. Chem. Phys.*, 2006, **8**, 1525–38.

30 J. D. Grunwaldt, A. M. Molenbroek, N. Y. Topsoe, H. Topsoe and B. S. Clausen, *J. Catal.*, 2000, **194**, 452–460.

31 M. B. Fichtl, J. Schumann, I. Kasatkin, N. Jacobsen, M. Behrens, R. Schlögl, M. Muhler and O. Hinrichsen, *Angew. Chem. Int. Ed. Engl.*, 2014, **53**, 7043–7.

32 T. Lunkenbein, J. Schumann, M. Behrens, R. Schlögl and M. G. Willinger, *Angew. Chemie - Int. Ed.*, 2015, **54**, 4544–4548.

33 S. Mehta, G. W. Simmons, K. Klier and R. G. Herman, *J. Catal.*, 1979, **57**, 339–360.

34 A. Zychma, R. Wansing, V. Schott, U. Köhler, C. Wöll, M. Muhler and A. Birkner, *Phys. Status Solidi*, 2013, **250**, 1071–1080.

35 T. Van Herwijnen and W. A. De Jong, *J. Catal.*, 1974, **34**, 209–214.

36 B. S. Clausen, J. Schiøtz, L. Gråbæk, C. V. Ovesen, K. W. Jacobsen, J. K. Nørskov and H. Topsøe, *Top. Catal.*, 1994, **1**, 367–376.

37 R. G. Herman, K. Klier, G. W. Simmons, B. P. Finn, J. B. Bulko and T. P. Kobylinski, *J. Catal.*, 1979, **56**, 407–429.

38 J. Schumann, J. Kröhnert, E. Frei, R. Schlögl and A. Trunschke, *Top. Catal.*, 2017, **0**, 1–9.

39 J. B. Bulko, R. G. Herman, K. Klier and G. W. Simmons, *J. Phys. Chem.*, 1979, **83**, 3118–3122.

40 M. S. Spencer, *Top. Catal.*, 1999, **8**, 259–266.

41 C. V Ovesen, B. S. Clausen, J. Schiøtz, P. Stoltze, H. Topsøe and J. K. Nørskov, *J. Catal.*, 1997, **168**, 133–142.

42 M. Behrens, S. Zander, P. Kurr, N. Jacobsen, J. Senker, G. Koch, T. Ressler, R. W. Fischer and R. Schlögl, *J. Am. Chem. Soc.*, 2013, **135**, 6061–8.

43 C. B. Ong, L. Y. Ng and A. W. Mohammad, *Renew. Sustain. Energy Rev.*, 2018, **81**, 536–551.

44 M. A. Borysiewicz, *Crystals*, 2019, **9**, 505.

45 J. G. Reynolds and C. L. Reynolds, *Adv. Condens. Matter Phys.*, 2014, 457058.

46 A. Kohan, G. Ceder, D. Morgan and C. G. Van de Walle, *Phys. Rev. B - Condens. Matter Mater. Phys.*, 2000, **61**, 15019–15027.

47 D. Look, G. Farlow, P. Reunchan, S. Limpijumnong, S. Zhang and K. Nordlund, *Phys. Rev. Lett.*, 2005, **95**, 225502.

48 K. Mohanta, S. K. Batabyal and A. J. Pal, *Chem. Mater.*, 2007, **19**, 3662–3666.

49 G. Brauer, J. Kuriplach, C. C. Ling and a B. Djurišić, *J. Phys. Conf. Ser.*, 2011, **265**, 012002.

50 M. Behrens, G. Lolli, N. Muratova, I. Kasatkin, M. Hävecker, R. Naumann d'Alnoncourt, O. Storcheva, K. Köhler, M. Muhler and R. Schlögl, *Phys. Chem. Chem. Phys.*, 2013, **15**, 1374–81.

51 W. W. Wenas, A. Yamada, K. Takahashi, M. Yoshino and M. Konagai, *J. Appl. Phys.*, 1991, **70**, 7119–7123.

52 H. J. Ko, Y. F. Chen, S. K. Hong, H. Wenisch, T. Yao and D. C. Look, *Appl. Phys. Lett.*, 2000, **77**, 3761–3763.

53 P. M. Ratheesh Kumar, C. Sudha Kartha, K. P. Vijayakumar, T. Abe, Y. Kashiwaba, F. Singh and D. K. Avasthi, *Semicond. Sci. Technol.*, 2005, **20**, 120–126.

54 D. M. Hofmann, A. Hofstaetter, F. Leiter, H. Zhou, F. Henecker, B. K. Meyer, S. B. Orlinskii, J. Schmidt and P. G. Baranov, *Phys. Rev. Lett.*, 2002, **88**, 045504.

55 S. B. Zhang, S.-H. Wei and A. Zunger, *Phys. Rev. B*, 2001, **63**, 075205.

56 R. G. Gordon, *AIP Conf. Proc.*, 1997, **39**, 394.

57 A. Janotti and C. G. Van De Walle, *Nat. Mater.*, 2007, **6**, 44–47.

58 Ü. Özgür, Y. I. Alivov, C. Liu, A. Teke, M. A. Reshchikov, S. Doğan, V. Avrutin, S. J. Cho and H. Morkҫ, *J. Appl. Phys.*, 2005, **98**, 1–103.

59 Y. J. Zeng, Z. Z. Ye, W. Z. Xu, D. Y. Li, J. G. Lu, L. P. Zhu and B. H. Zhao, *Appl. Phys. Lett.*, 2006, **88**, 062107.

60 P. Ding, X. H. Pan, Z. Z. Ye, J. Y. Huang, H. H. Zhang, W. Chen and C. Y. Zhu, *Solid State Commun.*, 2013, **156**, 8–11.

61 D. C. Look, D. C. Reynolds, C. W. Litton, R. L. Jones, D. B. Eason and G. Cantwell, *Appl. Phys. Lett.*, 2002, **81**, 1830–1832.

62 G.-T. Du, W. Zhao, G.-G. Wu, Z.-F. Shi, X.-C. Xia, Y. Liu, H.-W. Liang, X. Dong, Y. Ma and B.-L. Zhang, *Appl. Phys. Lett*, 2012, **101**, 053503.

63 Z. Shi, Y. Zhang, B. Wu, X. Cai, J. Zhang, X. Xia, H. Wang, X. Dong, H. Liang, B. Zhang and G. Du, *Appl. Phys. Lett.*, 2013, **102**, 161101.

64 F. X. Xiu, Z. Yang, L. J. Mandalapu, D. T. Zhao, J. L. Liu and W. P. Beyermann, *Appl. Phys. Lett.*, 2005, **87**, 1–3.

65 M. Wang, F. Ren, J. Zhou, G. Cai, L. Cai, Y. Hu, D. Wang, Y. Liu, L. Guo and S. Shen, *Sci. Rep.*, 2015, **5**, 1–13.

66 T. H. Fleisch and R. L. Mieville, *J. Catal.*, 1986, **97**, 284–285.

67 J. C. Frost, *Nature*, 1988, **334**, 577–580.

68 J. M. Dominquez, G. W. Simmons and K. Klier, *J. Mol. Catalyis*, 1983, **20**, 369–385.

69 A. J. Reddy, M. K. Kokila, H. Nagabhushana, R. P. S. Chakradhar, C. Shivakumara, J. L. Rao and B. M. Nagabhushana, *J. Alloys Compd.*, 2011, **509**, 5349–5355.

70 A. Ghosh, N. Kumari and A. Bhattacharjee, *Pramana - J. Phys.*, 2015, **84**, 621–635.

71 S. Colak and C. Aktürk, in *EMR/ESR/EPR Spectroscopy for Characterization of Nanomaterials*, 2017, vol. 62, pp. 151–179.

72 T. M. Yurieva, L. M. Plyasova, V. I. Zaikovskii, T. P. Minyukova, A. Bliek, J. C. van den Heuvel, L. P. Davydova, I. Y. Molina, M. P. Demeshkina, A. a. Khassin and E. D. Batyrev, *Phys. Chem. Chem. Phys.*, 2004, **6**, 4522.

73 J. W. Andreasen, F. B. Rasmussen, S. Helveg, A. Molenbroek, K. Ståhl, M. M. Nielsen and R. Feidenhans'l, *J. Appl. Crystallogr.*, 2006, **39**, 209–221.

74 T. H. Fleisch and R. L. Mieville, *J. Catal.*, 1984, **90**, 165–172.

75 J. B. Hansen and P. E. H. Nielsen, in *Handbook of Heterogeneous Catalysis*, 2008, vol. 2, pp. 2920–2949.

76 J. Schumann, T. Lunkenbein, A. Tarasov, N. Thomas, R. Schlögl and M. Behrens, *ChemCatChem*, 2014, **6**, 2889–2897.

77 P. M. Ratheesh Kumar, C. Sudha Kartha, K. P. Vijayakumar, F. Singh and D. K. Avasthi, *Mater. Sci. Eng. B Solid-State Mater. Adv. Technol.*, 2005, **117**, 307–312.

78 R. Gonzalez-Hernandez, A. I. Martinez, C. Falcony, A. A. Lopez, M. I. Pech-Canul and H. M. Hdz-Garcia, *Mater. Lett.*, 2010, **64**, 1493–1495.

79 E. Şennik, S. Kerli, Ü. Alver and Z. Z. Öztürk, *Sensors Actuators, B Chem.*, 2015, **216**, 49–56.

80 E. Gunasekaran, M. Ezhilan, G. K. Mani, P. Shankar, A. J. Kulandaisamy, J. B. B. Rayappan and K. J. Babu, *Semicond. Sci. Technol.*, 2018, **33**, 095005.

81 M. W. Kadi, D. McKinney, R. M. Mohamed, I. A. Mkhalid and W. Sigmund, *Ceram. Int.*, 2016, **42**, 4672–4678.

82 V. Dybbert, S. M. Fehr, F. Klein, A. Schaadt, A. Hoffmann, E. Frei, E. Erdem, T. Ludwig, H. Hillebrecht and I. Krossing, *Angew. Chemie - Int. Ed.*, 2019, 1–6.

83 B. S. Clausen and H. Topsoe, *Catal. Today*, 1991, **9**, 189–196.

84 F. Liao, Y. Huang, J. Ge, W. Zheng, K. Tedsree, P. Collier, X. Hong and S. C. Tsang, *Angew. Chemie - Int. Ed.*, 2011, **50**, 2162–2165.

85 J. Yoshihara, J. M. Campbell and C. T. Campbell, *Surf. Sci.*, 1998, **406**, 235–245.

86 M. Batzill and U. Diebold, *Phys. Chem. Chem. Phys.*, 2007, **9**, 2307–18.

87 X.-Y. Liu, Y.-A. Li, S. Liu, H.-L. Wu and H.-N. Cui, *Thin Solid Films*, 2012, **520**, 5372–5377.

88 F. Jamali Sheini, J. Singh, O. N. Srivasatva, D. S. Joag and M. A. . More, *Appl. Surf. Sci.*, 2010, **256**, 2110–2114.

89 F. M. Li, R. Waddingham, W. I. Milne, A. J. Flewitt, S. Speakman, J. Dutson, S. Wakeham and M. Thwaites, *Thin Solid Films*, 2011, **520**, 1278–1284.

90 S. Hadi, A. Kurniawan, Z. Arifin, Ubaidillah and Suyitno, *AIP Conf. Proc.*, , DOI:10.1063/1.4943445.

91 Z. Zhou, K. Kato, T. Komaki, M. Yoshino, H. Yukawa, M. Morinaga and K. Morita, *J. Electroceramics*, 2003, **11**, 73–79.

92 J. C. Slater, *Rev. Mod. Phys.*, 1946, **18**, 441–512.

93 R. Moos, *Sensors*, 2010, **10**, 6773–6787.

94 Patent DE102011076347, 2012.

95 C. Heine, M. Hävecker, M. Sanchez-Sanchez, A. Trunschke, R. Schlögl and M. Eichelbaum, *J. Phys. Chem. C*, 2013, **117**, 26988–26997.

96 M. Heenemann, Dissertation, *Charge Transfer in Catalysis Studied by In-situ Microwave Cavity Perturbation Techniques*, Technische Universität Berlin, 2017.

97 Feynman, Leighton and Sands, *The Feynman Lectures on Physics - New Millenium Edition, Volume 2*, Basic Books, 1964.

98 M. Abramowitz and I. A. Stegun, *Handbook of Mathematical Functions With Formulas, Graphs and Mathematical Tables (National Bureau of Standards Applied Mathematics Series No. 55)*, National Bureau of Standards, Tenth Prin., 1972.

99 M. Dietrich, D. Rauch, A. Porch and R. Moos, *Sensors*, 2014, **14**, 16856–16868.

100 L. F. Chen, C. K. Ong, C. P. Neo, V. V. Varadan and V. K. Varadan, *Microwave Electronics*, John Wiley & Sons, Ltd, Chichester, UK, 2004.

101 O. Klein, S. Donovan, M. Dressel and G. Grüner, *Int. J. Infrared Millimeter Waves*, 1993, **14**, 2423–2457.

102 D. C. Dube, *J. Phys. D Appl. Phys.*, 1970, **3**, 1648–1652.

103 H. Looyenga, *Physica*, 1965, **31**, 401–406.

104 C. Heine, F. Girgsdies, A. Trunschke, R. Schlögl and M. Eichelbaum, *Appl. Phys. A*, 2013, **112**, 289–296.

105 C. Heine, M. Hävecker, M. Sanchez-Sanchez, A. Trunschke, R. Schlögl and M. Eichelbaum, *J. Phys. Chem. C*, 2013, **117**, 26988–26997.

106 M. Eichelbaum, M. Hävecker, C. Heine, A. Karpov, C.-K. Dobner, F. Rosowski, A. Trunschke and R. Schlögl, *Angew. Chem. Int. Ed. Engl.*, 2012, **51**, 6246–50.

107 P. Pötschke, S. M. Dudkin and I. Alig, *Polymer (Guildf).*, 2003, **44**, 5023–5030.

108 D. Kajfez, *Q Factor Mesurements Using MATLAB (R)*, Artech House, Norwood, 2011.

109 C. Heine, Dissertation, *The Electronic Structure of Vanadium Oxides as Catalysts in the Selective Oxidation of Small Alkanes The Electronic Structure of Vanadium Oxides as Catalysts in the Selective Oxidation of Small Alkanes*, Technische Universität Berlin, 2014.

110 D. O. Klenov, G. N. Kryukova and L. M. Plyasova, *J. Mater. Chem.*, 1998, **8**, 1665–1669.

111 A. Gurlo and R. Riedel, *Angew. Chemie - Int. Ed.*, 2007, **46**, 3826–3848.

112 F. F. Vol'kenshtein, *The electronic theory of catalysis on semiconductors*, Pergamon Press Ltd., 1963.

5 The relation of model Cu/ZnO catalysts to technical systems

E.H. Wolf, M.-M. Millet, L.D. Zwiener, D. Brennecke, O. Timpe, F. Girgsdies, R. Imlau, W. Hetaba, H.C. Nerl, L. Masliuk, G. Algara-Siller, D. Teschner, T. Risse, R. Schlögl, and E. Frei

Author contributions: E.H. Wolf designed and oversaw the project and collected the experimental results by writing this paper draft. Furthermore, she carried out and evaluated the DR-UV-vis, and MCPT experiments, as well as the H_2-TPD and N_2O RFC and the catalytic testing of the catalysts generated by impregnation. M.-M. Millet carried out the synthesis of the samples generated by impregnation and provided feedback on the paper draft. L.D. Zwiener and D. Brennecke carried out the synthesis of the coprecipitated samples, and L.D. Zwiener also gave feedback on the paper draft. D. Brennecke also carried out the H_2-TPD and N_2O-RFC measurements for the coprecipitated series and aided in the data evaluation. O. Timpe carried out and evaluated the XRF and ICP experiments. F. Girgsdies carried out and evaluated the XRD experiments and fits and gave feedback on the paper draft. R. Imlau carried out and evaluated the electron microscopy of the Cu-I samples and gave feedback on the paper draft. W. Hetaba, H. Nerl, L. Masliuk, and G. Algara-Siller carried out the electron microscopy of one of the Cu-C samples each and W. Hetaba also gave feedback on the paper draft and on the evaluation of the electron microscopy results. D. Teschner carried out and evaluated the XPS analysis and provided feedback on the paper draft. T. Risse, R. Schlögl, and E. Frei oversaw the project and provided discussion and extensive feedback on the paper draft and experimental design.

The relation of model Cu/ZnO catalysts to technical systems

5.1 Abstract

In order to investigate aspects of industrial catalyst systems, a common approach is the study of model catalysts. These catalysts simplify the technical system such that aspects of it can be studied in more detail, or with the aim of applying experimental techniques which are not (yet) applicable to the real system. For the industrial methanol synthesis catalyst, commonly Cu/ZnO model catalysts are prepared by employing coprecipitation or impregnation as a synthetic method. Furthermore, often the Cu content of the model systems is lowered in comparison to the technical catalyst. Here, two series of samples made by coprecipitation and impregnation, respectively, and each with samples of different Cu contents, are investigated in view of the applicability of such samples as model catalysts. The influence on synthetic strategy and Cu content on the structural, electronic, and catalytic properties of the samples is investigated. For this, the samples were characterised using multiple experimental techniques including X-ray diffraction, UV-vis spectroscopy, electron microscopy and contact-free and *operando* conductivity measurements using a microwave cavity perturbation technique.

5.2 Introduction

Cu and ZnO form the basis of the industrial catalyst system employed in CO_2 reduction reactions, *e.g.*, methanol synthesis or the reverse water/gas shift reaction (rWGS)[1]. In light of the increasing levels of CO_2 in the earth's atmosphere[2] as well as increasing scarcity of conventional fossil sources for combustion fuels and chemical feedstocks with likewise increasing demand,[3,4] such reactions help to alleviate these problems as part of a closed carbon cycle.[5–7] In industry, a catalyst consisting of Cu/ZnO/Al_2O_3 containing a high amount of Cu (more than 50 mol % metal base[8]) is employed and was intensively studied in the past[8–11 and references therein].

Simplifying the industrial system to give so-called model catalysts can be advantageous, because the complexity of the system is reduced, allowing for the investigation and further understanding of specific aspects of the catalyst. Furthermore, model catalysts

may allow for the use of experimental techniques that cannot be applied on the industrial catalyst due to, for example, the relatively high Cu content or the morphology of the catalyst. Common strategies for the generation of Cu/ZnO model catalysts as models for the technical methanol synthesis catalysts include impregnation and coprecipitation, and the Cu content is often kept significantly lower than is the case in the industrial system.[12–14] In this contribution, the applicability of such model catalysts as models for the technical system is investigated.

One area of interest in Cu/ZnO catalysts is the interaction of its components, Cu and ZnO. It has been shown that a strong interaction between Cu and the ZnO support, referred to as a strong metal-support interaction (SMSI) is of crucial importance for this system, which renders detailed studies of this interface particularly interesting. [8,10,12,13,15,16] As a consequence, under reaction conditions the catalyst surface is strongly enriched by ZnO growing over the Cu particles. Furthermore, it was found that defects, in Cu and ZnO, play an important role for the catalytic activity[10,13,17,18]. Generally, the Cu-ZnO interface is an example of an intriguing synergism, where multiple structural and electronic effects are coupled to each other. One strategy to decouple the effects caused by the different components of the system is to reduce the structural complexity by employing model systems.

A way to affect or alter the Cu/ZnO interface is by doping of ZnO. Doping has an impact on the electronic and structural properties of ZnO, which in turn will affect the way ZnO interacts with Cu.[19] In general, doping of semiconductor oxides with ions changes the electronic structure of the oxide by altering the number of electrons (or holes) in the semiconductor and the position of the Fermi level, which in turn affects the catalytic activity of the material.[20] So far, the interfacial contact of Cu and doped ZnO has been studied in model systems. The investigations involved variation of the dopant (Al, Ga, and Mg, scheme in Figure 5.1(a)) or its quantity (series of Al doping, scheme Figure 5.1(b)) with a constant Cu loading of 10 wt. %. This guaranteed a more or less constant amount of interfacial contact area which differs in its nature (under the assumption of a comparable metal-support interaction). The extrinsically doped ZnO (*e.g.,* using Al, Ga, or Mg[21–25]) was studied with respect to both structural and electronic promotion[26,27]. Upon variation of the doping element, both the ZnO conductivity as well as its ability to form a ZnO overlayer

on Cu could be altered.[19] In addition, studies on model Cu/ZnO:Al catalysts have been performed involving careful characterisation of the catalysts in view of their structural properties and (surface) composition as well as catalytic measurements and the investigation of the electronic properties of the samples using *operando* microwave conductivity and *operando* microwave Hall effect measurements.[19,24,25] This showed that increasing the content of Al dopant leads to an enhanced catalytic activity in the rWGS reaction, correlating with the concentration of charge carriers in the catalyst.[19,24,25] In addition to the inclusion of extrinsic dopants into the Cu/ZnO catalyst, Cu itself may also act as a dopant as a result from incorporation and diffusion into ZnO during the synthesis, calcination[12,28] and activation process[29–31,]. However, the extent of this doping and its significance for CO_2 hydrogenation has been controversially disputed.[30–38] To further elucidate the contribution of $Cu/Cu^{+I/+II}$ on the structural, electronic, and catalytic properties of CO_2 hydrogenation catalyst, this study employs pure Cu/ZnO (CuO/ZnO) systems without the addition of another extrinsic dopants, since these may mask the contribution of Cu acting as a dopant.

In this contribution, the applicability of model Cu/ZnO catalysts as representatives for the technical system is investigated. For this reason, two series of samples were synthesized each with a varying Cu content. To achieve this, two commonly used strategies were employed, namely impregnation and coprecipitation. The two series aim at changing the quantity of interfacial contact of Cu (CuO) and ZnO for a given Cu fraction, so that the consequences of this can be investigated.

The schemes in Figure 5.1(c) and (d) visualise the different starting points of interfacial contact, pre-determined by the two different synthesis methods. From an idealised point of view, impregnation leads to little contact between Cu and ZnO, as a Cu citrate solution is dropped onto already existing ZnO support (incipient wetness impregnation, for details see the experimental section). By subsequent calcination, the interfacial contact between the CuO and ZnO phases in the samples is developed. In contrast, co-precipitation aims at a complete intermixture of Cu and Zn in the hydroxycarbonate precursor on the atomic level. It is expected that the interface might slightly decrease upon calcination because of phase segregation into CuO and ZnO. However, the interfacial contact and the possible doping of ZnO with Cu cations might be greatly enlarged in comparison to the

impregnated samples. A subsequent activation of the catalysts under, *e.g.*, reduction of the Cu moieties leads to the final Cu-ZnO interface we aim at. Here, in case of the samples generated by impregnation, an increase in Cu ions dissolved in ZnO may result from calcination and subsequent reduction.[31,39] On the other hand, reduction of Cu,Zn oxide solid solutions (as for example generated by co-precipitation) may result in the generation of metallic Cu particles and Cu-doped ZnO, respectively. This means with impregnation we start with a low Cu-doped ZnO and possibly enrich the ZnO upon activation, and vice versa: With co-precipitation the perfect intermixture is (at least in parts) transferred into Cu/CuO and ZnO moieties at the expense of Cu-doping.

Comparing samples generated by these two different methods thus enables us to elucidate differences in the *quantity* of the Cu-ZnO interaction by different Cu loadings and a possible *qualitative* change by the degree of Cu dopant (as a function of the loading and the synthesis approach).

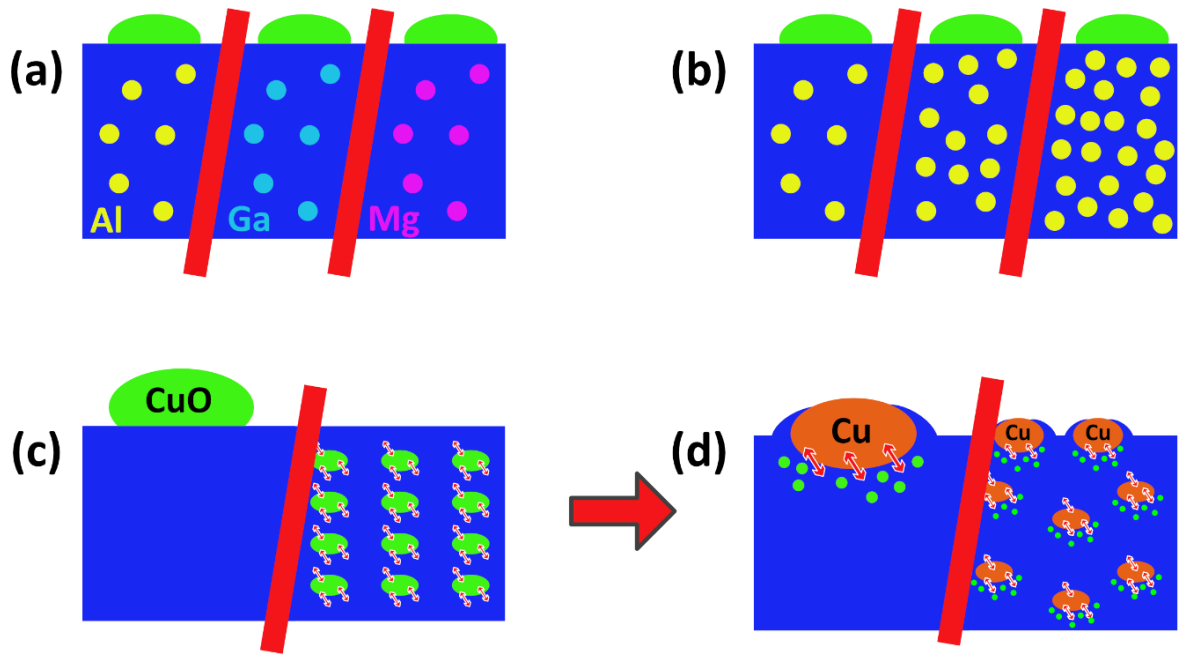

Figure 5.1: Scheme illustrating previous studies (a-b) and the presented work (c-d). (a) Different types of dopant ions (*e.g.*, Al, Ga, or Mg), (b) different amounts of Al dopant, (c) the impregnated (left) and co-precipitated (right) samples after synthesis, and (d) the samples after calcination and reduction.

In this study, the concentration of Cu is kept low (below 10 %) in order to decrease the contribution from Cu particles.

To reveal qualitative changes to the structural, catalytic, and electronic properties of the samples in a relevant state, various experimental techniques were employed. The bulk structure and the morphology of the samples was studied using X-ray diffraction and (Scanning) Transmission Electron Microscopy. The Cu surface area and oxygen vacancies were probed using H_2-Temperature Programmed Desorption (H_2-TPD) and N_2O Reactive Frontal Chromatography (N_2O-RFC). Diffuse Reflectance UV-vis spectroscopy was used to reveal changes to the optical band gap as a function of Cu content. Next to catalytic testing and kinetic analysis in the reverse water-gas shift reaction, an *operando* microwave cavity perturbation technique (MCPT), able to measure the elecrical conductivity of the samples, was used in order to directly relate changes in electronic properties to the catalytic performance of the samples.

5.3 Experimental

5.3.1 Synthesis

Two series of CuO/ZnO samples as pre-catalysts were synthesised, each with a nominal CuO loading between 0 and 10 at.%. The two synthetic approaches employed were impregnation of ZnO with Cu citrate and coprecipitation of Zn-rich Cu,Zn precursors.

5.3.1.1 Impregnation Series

The impregnation series of CuO/ZnO samples with varying loading of CuO on ZnO was synthesised by the impregnation of ZnO with copper citrate.

ZnO was synthesised by precipitation from the nitrate as follows: 357.00 g zinc nitrate hexahydrate were dissolved in 500 mL deionised water, followed by the addition of 15 mL 65 % nitric acid and filling up to 600 mL. Another solution was prepared by dissolving 339.16 g sodium carbonate in deionised water to give a total of 2 L. 400 mL deionised water were added to an automated laboratory reactor (Labmax, Mettler-Toledo), and the zinc nitrate solution was added at a rate of 20 g/min for 30 min, while adding the sodium carbonate solution in appropriate quantities in order to keep the pH constant at 6.5. The mixture was aged for 1 h, the precipitate was filtered and washed twice with 600 mL water. The conductivity of the filtrate after washing was less than 0.5 mS/cm. The powder product was dried at 373 K in a drying oven. After drying, the obtained zinc

hydroxycarbonate was calcined in a muffle oven in static air at 603 K (ramp rate 2 K/min, dwell time 3 h) to yield ZnO.

Copper citrate was synthesised by dissolving 48.96 g copper nitrate trihydrate in 400 mL deionised water. A solution of 16.20 g sodium hydroxide in 400 mL water was added slowly to the copper nitrate solution while ice-cooling. Instantaneously, copper dihydroxide formed as a blue precipitate and was washed until the filtrate conductivity was less than 0.5 mS/cm. The yielded hydroxide was suspended in 400 mL water, and a solution of 16.58 g citric acid in 100 mL water was added slowly. This was then left to stand for 4 days, and a greenish solid precipitated which was subsequently removed from the beaker walls using an ultrasonic bath before filtering and drying.

ZnO was impregnated with copper citrate by dropping 3 mL citrate solution (in 12.5 % $NH_{3(aq)}$) appropriately concentrated for each desired loading on 6 g ZnO before stirring to dry in air. The exact amount of Cu citrate needed for the impregnation solution was determined by thermogravimetry. An overview of the nominal loadings of the samples along with the concentration of the citrate solutions can be found in table SI 5.1 (page81). The samples were dried at 393 K for 10 h (ramp rate 2 K/min) in static air before calcining in a muffle oven at 603 k for 180 min (ramp rate 2 K/min) to yield CuO/ZnO.

5.3.1.2 Coprecipitation Series

A sample of coprecipitated CuO/ZnO was prepared, where the CuO concentration was varied across the series. For this, copper nitrate and zinc nitrate solutions (in water) were prepared, along with a sodium carbonate solution. In an automated reactor (Labmax, Mettler-Toledo), 400 mL water were placed and adjusted to pH 9 using 1.6 M sodium carbonate solution. The metal nitrate solutions were added at a rate of 600 g/30 min at a temperature of 65 °C while keeping the pH at 9 by adding appropriate amounts of sodium carbonate solution. The suspension was aged for 60 min before washing until the filtrate conductivity was less than 0.5 mS/cm. The solid residue was spray dried at 80 °C. The obtained powder was calcined at 330 °C (ramp rate 2 K/min, dwell time 3 h) in a muffle furnace to yield CuO/ZnO. The exact metal salt quantities used for the synthesis can be found in table SI 5.2 (page 81).

5.3.2 Characterisation

5.3.2.1 X-ray Fluorescence Analysis (XRF)

The composition of the samples was analysed using X-ray fluorescence analysis (XRF). The Cu $K\alpha_1$ and Zn $K\alpha_1$ lines were determined using a Bruker S4 Pioneer X-ray spectrometer for the determination of the Cu and Zn content, respectively. For this, about 100 mg sample (exact weights in table SI 5.3, page 82) were fused together with 8.9 g lithium tetraborate and ca. 100 mg lithium bromide to form a glass melt disk of 40 mm diameter.

5.3.2.2 Powder X-ray Diffraction (XRD)

Powder X-ray diffraction (XRD) was performed to identify the crystalline phases present in the sample by using a Bruker AXS D8 Advance II theta/theta diffractometer in Bragg-Brentano geometry, employing Ni filtered Cu $K_{\alpha 1+2}$ radiation and a position sensitive energy dispersive LynxEye silicon strip detector. The XRD data were evaluated by whole powder pattern fitting according to the Rietveld method as implemented in the TOPAS software (version 5, Bruker AXS 1999-2014)

5.3.2.3 (Scanning) Transmission Electron Microscopy (TEM)

(Scanning) Transmission Electron Microscopy (TEM) measurements were performed after reduction at 523 K (ramp rate 2 K/min, dwell time 1 h). Another set of samples was investigated after catalytic testing in the rWGS reaction using a parallel reactor setup. The samples were lightly oxidised after catalytic testing in order to prevent changes to the particles as a result of fast exposure to ambient air, and they were reduced again prior to inert transfer to the microscope. After inert transfer of the samples via a glove box using a vacuum transfer holder, the investigation was performed using a Thermo Fisher Scientific Talos F200X S/TEM. The microscope was operated at an acceleration voltage of 200 kV. For STEM measurements, a HAADF detector was used. Energy Dispersive X-Ray Spectroscopy (EDX) maps were generated using the Super-X EDX system utilising four silicon drift detectors.

5.3.3 Cu surface area determination

The Cu surface area was determined using two complementary methods: H_2-TPD and N_2O-RFC subsequently.

For a typical experiment, about 200 mg of sample were placed into a reactor connected to a gas delivery system at the front end. The exhaust gases were analysed using a mass spectrometer. The reactor was located inside a heating element with the option to apply liquid nitrogen (LN_2) in order to cool down the sample. Prior to the desorption experiment, the sample was reduced in a 40 mL/min flow of 10 % H_2/He by heating to 523 K at a rate of 2 K/min and keeping the sample at this temperature for 1 h. The system was consecutively flushed with 80 mL/min He before cooling to 233 K. The gas flow was then changed to 80 mL/min H_2 and the pressure was increased from ambient pressure to 24 bar. After 30 min at 233 K, the sample was cooled to LN_2 temperature before lowering the pressure back to 1 bar and flushing the system with 80 mL/min He for 1 h. The desorption was then performed by heating the sample to 523 K at a rate of 6 K/min and holding for 30 min.

Following this desorption protocol and letting the sample cool to ambient temperature, a N_2O-RFC was performed by applying a flow of 10 mL/in N_2O over the sample.

Assuming a Cu:H_2 ratio of 2.81,[40] the number of surface Cu atoms per gram of catalyst can be calculated from H_2-TPD. N_2O-RFC assumes a conversion of N_2O on the surface sites according to[41,42]

$$N_2O_{(g)} + 2Cu_{(s)} \rightarrow N_{2(g)} + (Cu - O - Cu)_{(s)}$$

to calculate the amount of surface Cu atoms per gram of catalyst. From this, the Cu surface area can be calculated, assuming that the number of Cu atoms per square meter is $1.47 \cdot 10^{19}$.[42]

5.3.4 Diffuse Reflectance UV-vis Spectroscopy

Diffuse Reflectance UV-visible-near-IR spectroscopy (DR-UV-vis-NIR) was performed on an Agilent Cary 5000 UV-vis-NIR spectrometer in a Harrick Praying Mantis High Temperature Reaction Chamber connected to a gas delivery system. To reduce the samples, they were first heated to 503 K in 50 mL/min He flow, then the gas flow was changed to 50 mL/min 10 % H_2/He for 1 h. The reflectance spectra were transformed to Kubelka-Munk units and normalised, before plotting them as Tauc plots. The ZnO absorption edge was extrapolated to zero intensity to determine the optical band gap.

5.3.5 Reactivity test in the reverse Water-Gas-Shift (rWGS) reaction

Catalytic testing in the reverse Water-Gas Shift (rWGS) reaction was carried out in an 8-fold parallel reactor setup. For this, about 50 mg of sample (sieve fraction 100-200 µm) were weighed out and diluted in about 2.95 g SiC (sieve fraction 250-355 µm) in order to improve heat transfer within the catalyst bed. The reactors were connected at the inlet to a gas supply system, and the composition of the evolved gas was determined using a gas chromatograph (Agilent 7890A). Heating was achieved by placing the samples inside a furnace, and the temperature of each reactor was determined using in-bed thermocouples. A table detailing the exact weight of sample and SiC in each reactor can be found in SI 5.20 (page 91).

Prior to the catalytic measurements, the samples were reduced in 5 % H_2/N_2 with a flow of 50 mL/min by heating to 523 K at a rate of 2 K/min and holding at this temperature for 1 h. The temperature was then lowered to 503 K in 30 mL/min N_2.

Catalytic testing was performed between 473 K and 513 K, varying the flow per reactor between 10 mL/min and 30 mL/min. Different $CO_2/H_2/N_2$ ratios were employed. Details about the experimental conditions and sequence can be found in table SI 5.21 (page 92).

5.3.6 Conductivity Measurements

The conductivity of the samples was determined contact free and *in operando* using a Microwave Cavity Perturbation Technique (MCPT) setup described previously[43]. In short, this technique exploits the properties of a microwave resonator (position and width of the resonance peak) under changing experimental conditions to deduce the conductivity of the sample. Particular care was taken to properly account for background effects of the system. The changes in the peak properties result from the perturbation of a resonance wave of microwave frequency present in the microwave cavity. A network analyser (Agilent Technologies N5230C) is used to provide and detect the frequency response of the resonator. To deduce the conductivity from the measured data (reflection coefficient of the reflected and incident waves, $\Gamma = \frac{V_-}{V_+}$ versus frequency), they were first fit using an algorithm by Kajfez[44] (fitting interval 0.4), resulting in the so-called Q factor and the resonance frequency. From these values, we calculated the conductivity σ using

$$\varepsilon_2 = C\frac{V_c}{V_s}\left(\frac{1}{Q_s} - \frac{1}{Q_e}\right)$$

$$\sigma = \omega_e \varepsilon_2 \varepsilon_0$$

where ε_2 is the imaginary part of the permittivity, V_c and V_s are the volume of the cavity and the sample, respectively, Q_s and Q_e are the Q factors determined from the measurement with sample and the empty reference measurement. ω_e is the resonance frequency and ε_0 is the vacuum permittivity. The factor C is a calibration constant. We used the TM_{020} mode of an S-band resonator with a resonance frequency of about 7.59 GHz for our investigations.

To account for differences in powder packing density between the samples inside the reactor, the values obtained were corrected using effective medium theory[45,46]. For this, the crystallographic density of the samples determined from the formula unit and the cell volume, obtained from refined XRD data, was assumed.

Operando measurements of the conductivity were performed by placing a quartz glass reactor in the maximum of the electric field component of the resonator. The sample is located in a quartz tube surrounded by another tube which carries hot N_2 gas (flow rate of 8 L/min) to heat the sample. The inlet of the sample tube is connected to a gas manifold allowing to apply reactive and inert gases, while the outlet of the tube is connected to a gas chromatograph (Agilent 7890A) for analysis of the product gas stream. The temperature of the microwave resonator is kept constant at 293 K by cooling with Peltier elements located at the top and bottom of the resonator. In order to prevent condensation of water inside the resonator it is purged with 15 mL/min N_2.

We investigated the conductivity of the samples during rWGS conditions. Prior to the application of the rWGS test mixtures, the samples were first reduced by heating to 523 K at a rate of 2 K/min in a flow of 10 % H_2/N_2. After the reduction was completed, the temperature was lowered to 503 K used throughout the entire subsequent testing. For rWGS testing, 10 mL/min of a 1:2:7 $CO_2/H_2/N_2$ gas mixture was applied, before changing the gas ratio to 1:3:6, and finally back to 1:2:7 to confirm the reversibility and reproducibility of the experiment.

5.4 Results and Discussion

In the following, the samples and their derivatives (e.g., activated samples or samples during/after reaction) will be identified by their Cu content (as determined by XRF) and their synthetic method, e.g., “7.28Cu-I” for a sample out of the impregnation series with a CuO content of 7.28 wt.% or “0.1Cu-C” for a sample with 0.1 wt.% Cu content out of the sample series produced by coprecipitation. If the whole series is implied, the designations “Cu-I” and “Cu-C” are used for the series produced by impregnation and by coprecipitation, respectively. The calcined precursors are named “precatalysts”, and they are only termed “catalysts” after activation.

Table 5.1 presents an overview of the samples used in this study along with results from X-ray fluorescence analysis and surface area determination using the BET method. Since the ZnO for the impregnation series was dried in a drying furnace, while all coprecipitated samples were spray dried, absolute values (quantities) can only be compared within each series. However, qualitative trends can also be deduced from comparisons between the “Cu-I” and “Cu-C” series.

Table 5.1:Overview of all samples presented, including the Cu content determined by XRF and the BET surface areas (see Supporting Information in section 5.8.4 for details).

Sample	Nominal Cu loading [at. % metals base]	XRF CuO loading [wt. %]	Precursor BET surface area [m^2/g]	Precursor Internal FHI no	Precatalyst BET surface area [m^2/g]	Precatalyst Internal FHI no
7.28Cu-I	5	7.28			39.6	24278
3.86Cu-I	2.5	3.86			39.5	24279
1.06Cu-I	1	1.06			35.4	24280
0.86Cu-I	0.5	0.86			34.5	24281
0.3Cu-I	0.1	0.3			32.4	24282
ZnO	0				39.9	24277
9.65Cu-C	10	9.65	62.6	30295	87.44	30444
4.77Cu-C	5	4.77	60.5	30294	85.2	30438
2.96Cu-C	2.5	2.96	58.9	30293	91.8	30428
1.44Cu-C	1.5	1.44	55.4	30292		30421
1.06Cu-C	1	1.06	54.2	30291	75.5	30410
0.44Cu-C	0.5	0.44	55.5	30290	76	30392
0.17Cu-C	0.1	0.17	53.2	30289	68.1	30388
ZnO-C	0	0.15	53	30288	65.7	30387

5.4.1 Characterisation of the electronic, structural, and surface properties

5.4.1.1 ZnO lattice parameter c *and ZnO crystallite size determined by X-Ray diffraction*

To elucidate the effect of the two different synthesis methods on the crystalline phases in the samples, powder XRD was employed on the calcined pre-catalysts. Owing to the differences in synthetic method, it can be expected that impregnation leads to agglomeration of CuO on the surface of ZnO, while coprecipitation is expected to enable a more homogeneous intermixture between the metal cations throughout the sample. This can be distinguished from the diffractograms. Crystalline CuO phases result in characteristic reflections in the diffractograms, while an incorporation of Cu^{2+} or Cu^{+} ions into the ZnO lattice may evoke changes to the lattice parameters and thus the diffraction peak positions ZnO. At low Cu content the sensitivity towards CuO is, however, limited.

Furthermore, the location of the dominant 111 reflection of CuO almost coincides with the main feature of the ZnO pattern, rendering a discrimination difficult for small intensities.

The full diffraction patterns are given in the supporting information (see section 5.8.5). In short, the main phase exhibited in the diffractograms of all samples was ZnO, with some CuO reflections observed in the diffractograms of the Cu-I series samples with Cu content > 1 %. In order to explore the question whether copper ions may be dissolved in the ZnO lattice, the diffraction patterns were subjected to full pattern Rietveld fitting. By this means, it was possible to extract the lattice parameters of the ZnO phase. It should be noted that the dominant contribution of the ZnO Bragg peaks in all pattern exhibits complex anisotropic (i.e., *hkl* dependent) peak broadening. The best agreement between measured and calculated data was obtained by combining an anisotropic domain size broadening model with an additional isotropic strain contribution. The lattice parameter *a* remains quite similar for all samples, with the notable exception of the 9.65Cu-C sample (see figure SI 5.12, page 87), and will not be discussed further. In Figure 5.2, the results for the lattice parameter *c* are presented as a function of CuO content for both series. There is little systematic change of *c* for the Cu-I series. In contrast, the lattice parameter changes markedly with CuO content in case of the Cu-C series. There is an increase in this lattice parameter with increasing CuO content between ZnO-C and 2.96Cu-C, after which the lattice parameter becomes slightly smaller for 4.77Cu-C and then drastically decreases to a value even lower than the lattice parameter of ZnO-C for the 9.65Cu-C sample.

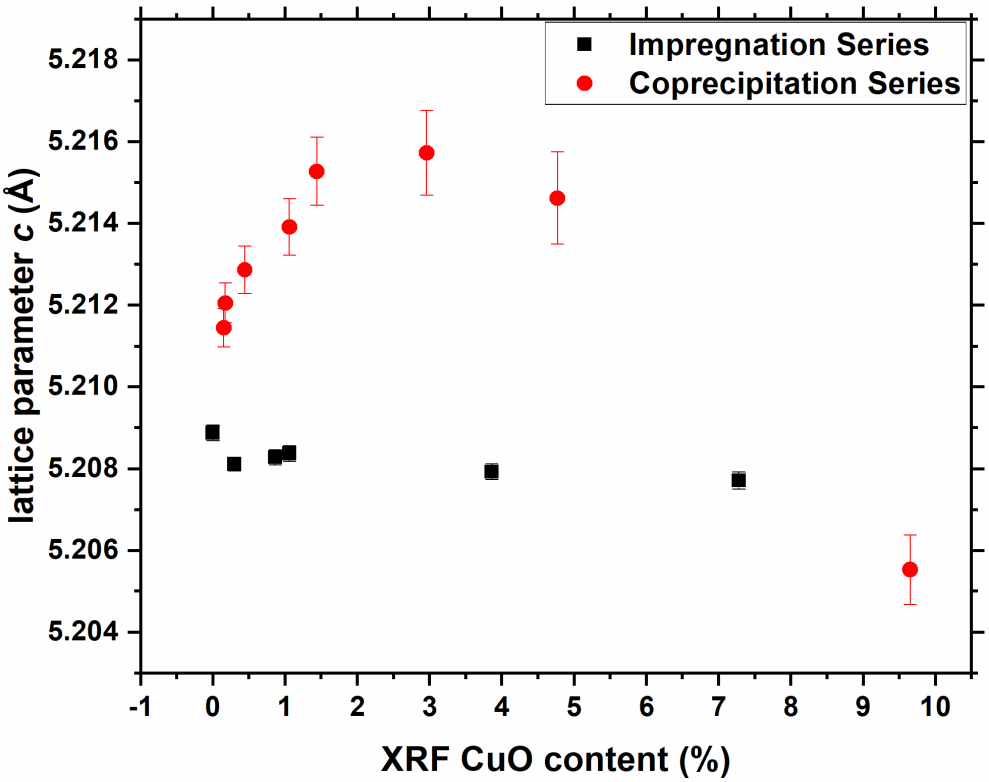

Figure 5.2: ZnO *c* lattice parameter determined by XRD.

The lattice parameter *c* highlights a fundamental difference between the differently synthesised sample series. The behaviour of *c* differs drastically between the Cu-I series (little change) and the Cu-C series (systematic change of *c* with Cu loading), which is indicative of the different interactions between ZnO and the Cu species present in the calcined samples. As mentioned before, there is a systematic change of the lattice parameter c depending on the samples' Cu content observed for the Cu-C series. This change indicates doping of ZnO by Cu ions, while no indication for doping of ZnO with copper ions is found in case of the Cu-I series. However, it has to be kept in mind that Cu and Zn have very similar structure factors, and compounds involving the ions may give rise to similar bond lengths (e.g., in tetrahedral coordination, Cu^{+} and Zn^{2+} typically have similar crystal radii)[47], making it possible that there is not enough sensitivity of this method for the detection of small amounts of Cu ions in the ZnO lattice. Furthermore, the maximum amount of ca. 3 at.% of Cu ions as part of the ZnO structure incorporated in the way observed from the change in lattice parameter *c* presented here is in line with the saturation limit of Al ions in ZnO.[48,49] This observation is very likely linked to an intrinsic property of ZnO defining a limited number of Cu ions which may be incorporated into the ZnO crystal lattice. Exceeding this limit might lead to a tendency for the phases to separate

and a decrease in the lattice parameter *c* as a consequence. Even though the lattice parameter *a* was increased for the 9.65Cu-C sample, this did not result in an increased unit cell volume (see figure SI 5.13, page 87). However, the CuO domains expected to form when the Cu concentration is increased slightly above 3 at.% are evidently below the XRD sensitivity (see figure SI 5.11, page 86, for a close up of the diffractogram around the region where the most intense CuO peaks could be expected). It should be noted that the sample with the highest Cu content (9.65Cu-C) deviates in the size of both lattice parameters as well as the unit cell volume from the behaviour observed for the other samples. Most notably, the lattice parameters for this sample deviate from those of ZnO-C as well. Therefore, this behaviour cannot be explained by phase segregation only, but another effect (most likely related to the addition of Cu) is underlying. Overall, the changes observed for the Cu-C series indicate that the lattice parameter *c* and thus the way Cu is incorporated in the ZnO lattice depends decidedly on the amount of Cu present in a coprecipitated sample. Furthermore, whether or not the lattice parameter *c* changes significantly at all as a function of the Cu content of the sample is dependent on the chosen synthesis method.

Based on the anisotropic peak broadening, estimates for the volume weighted mean domain sizes along the *a* and *c* axes of ZnO crystallites were extracted from the Rietveld fits. Generally, the ZnO crystallites are slightly larger in the *c* direction compared to the *a* direction. The Cu-I series shows rather stable crystallite sizes, whereas the domain sizes for the Cu-C series shows an inverted profile of the ZnO *c* lattice parameter, decreasing until 3 at.% and increasing afterwards (see Figure 5.3). The difference of the domain sizes between the Cu-I series and the Cu-C series (a factor of ≈ 2) is in line with the BET surface area values, which are almost double for the Cu-C series.

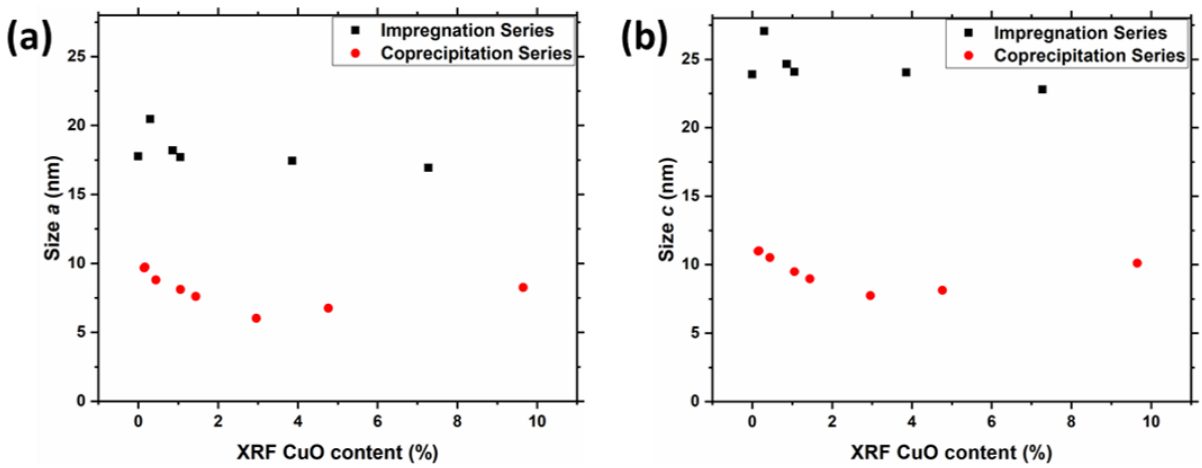

Figure 5.3: ZnO crystallite size of the samples in (a) *a* direction and (b) *c* direction.

5.4.1.2 (Scanning) Transmission Electron Microscopy

(Scanning) Transmission Electron Microscopy (S)TEM is an imaging technique able to give indications about particle size and morphology within the samples.[50] However, since Cu and Zn have very similar atomic weights, they produce very little contrast differences in electron microscope images. Therefore, the distribution of Cu in the ZnO matrix is determined by Energy-Dispersive X-Ray Spectroscopy (EDX) maps using their characteristic X-ray emissions. Since EDX mapping shows a projection through the sample, it has to be kept in mind that no discrimination can be made about the three-dimensional shape or size of the particles from this analysis.

The EDX maps shown in Figure 5.4 highlight the regions with Cu signal intensity for some samples of the Cu-I series. Before the STEM analysis, the samples were reduced (Figure 5.4 (a-c), and in Figure 5.4(d), an EDX map of 7.28Cu-I after rWGS testing and re-reduction is presented for comparison. To preserve the reduced state of the catalyst the samples were inertly transferred into the microscope using a vacuum transfer holder. From the EDX maps, it can be seen that all four samples consist of agglomerates of ZnO and exhibit a heterogeneous distribution of Cu indicative of the presence of small Cu-containing nanoparticles. It becomes evident that the size of the Cu particles increases with increasing Cu content in the samples. The most drastic difference is observed between the 1.06Cu-I and 3.86Cu-I samples, as can be seen from the exemplary line scans given in the supporting information (figure SI 5.27, page 95). Furthermore, the signal/noise and signal/background ratios of the line scans increase with increasing Cu loading. Additionally, it can be noted that there is Cu signal present outside of the Cu

agglomerates, which could indicate finely dispersed Cu, potentially even dissolved in the ZnO support. Overall, a more homogeneous Cu dispersion is resulting if the Cu loading is lowered. Thus, a general difference in the samples' morphology that is depending on the Cu content was found. The morphology and Cu-distribution of 7.28Cu-I was found to be not drastically altered as a cause of the catalytic measurements and subsequent re-reduction treatment (see Figure 5.4(c) and (d)).

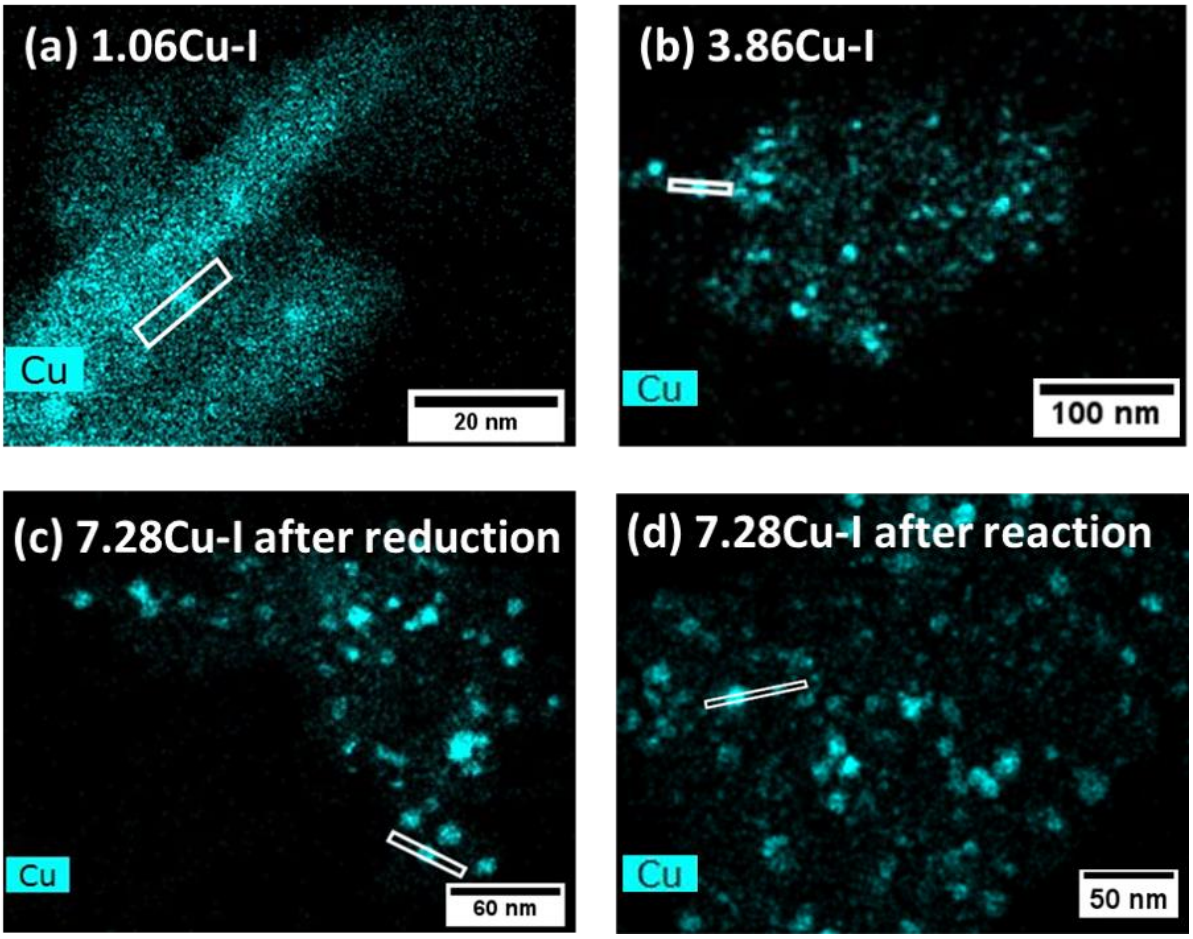

Figure 5.4: STEM/EDX maps of reduced samples (a-c) and 7.28Cu-I after reaction and re-reduction (d). Line scans of the marked regions are given in the supporting information (figure SI 5.27, page 95).

Cu-EDX mappings of Cu-C series samples in their reduced state (after rWGS testing and re-reduction), are presented in Figure 5.5. The white lines indicate the location of the exemplary line scans given in the supporting information (figure SI 5.29, page 96). Since the morphology and distribution of Cu in the 7.28Cu-I sample appeared unaltered between the reduced sample and the sample after reaction and re-reduction as mentioned above, it is possible to draw conclusions from the comparison of Figure 5.4 and Figure 5.5 and thereby compare the two sets of samples.

In general, the Cu-C samples presented in Figure 5.5 appear to have smaller Cu-containing agglomerates than the Cu-I samples presented in Figure 5.4. A comparison of the sizes of the Cu-particles formed at the different concentrations indicates that it may be possible that larger particles are formed only at a higher Cu concentration threshold in case of the Cu-C sample series than for the Cu-I series. Out of the Cu-I samples, only 1.06Cu-I contains particles similar in size to its Cu-C equivalent. Overall, Cu appears to be much more distributed over the investigated region in case of the Cu-C samples. It appears that the first few % of Cu that are added to the sample are included in the ZnO structure while larger particles are formed only when the incorporation limit is exceeded. To sum up, the EDX maps presented here show differences in the investigated samples resulting both from their synthetic history (*i.e.*, Cu-C samples in general show smaller, more dispersed Cu agglomerates) and from their different Cu contents (*i.e.*, Cu is more dispersed in samples with lower Cu content).

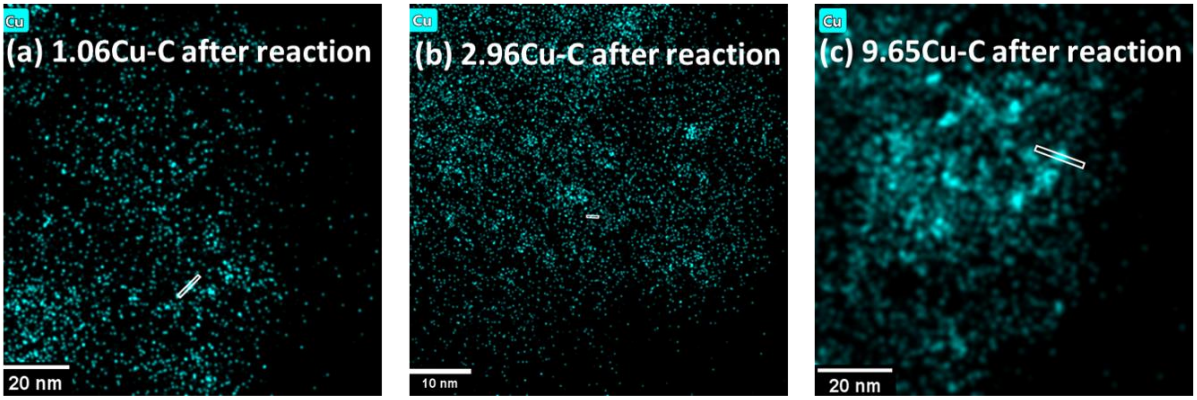

Figure 5.5: STEM/EDX maps of samples retrieved after catalytic testing and re-reductionLine scans of the indicated regions can be found in the supporting information figure SI 5.29, page 96).

5.4.1.3 H_2-Temperature Programmed Desorption and N_2O-Reactive Frontal Chromatography

The Cu surface area of the samples was investigated using both H_2-TPD and N_2O-RFC (Figure 5.6), which are complementary methods but have sensitivity for different surface species. It should be noted that both the N_2O-RFC and H_2-TPD method are not usually applied for samples with such low Cu loading, and thus the relationship between the "surface area" values given here and the actual Cu-surface area is unclear and might even vary from sample to sample. While H_2-TPD selectively probes the Cu surface of the reduced samples only, N_2O-RFC additionally probes defects (or redox active sites) on the

ZnO surface. [19,51] Generally, the N_2O-RFC determined surface areas can be expected to be higher than the surface area determined by H_2-TPD. This was indeed found to be the case for our samples (with a few exceptions). Since the H_2-TPD values obtained are rather small (< 1 m^2/g), a detailed quantitative discussion is not intended. However, the small values of the H_2-TPD indicate that the Cu moieties in the sample may be significantly covered with ZnO. For the Cu-I series, this can be explained by the wetting of Cu on ZnO, leading to flattened particles and a comparably large diameter as already indicated by the EDX maps and line scans. It is observed that the H_2-TPD derived values at low Cu contents are higher for the Cu-I samples than the Cu-C samples, but this is reversed in case of the samples with higher Cu content. It should be noted, that while the trends for the H_2-TPD derived values differ between the differently synthesised samples, both series show a dependence on the Cu content of the samples. This is also the case for the N_2O-RFC derived values. However, the latter show a similar loading-dependent trend and comparable values for the Cu-I and the Cu-C series. This is surprising, since the BET surface area is almost doubled for Cu-C in comparison to Cu-I. A reason for this might be the limited accessibility of Cu within the Cu-C series as a result of the high dispersion (observed by STEM/EDX) and incorporation of Cu within ZnO (as observed by the expansion of the lattice parameter *c* in the calcined precursors). This would lead to the conclusion that the Cu particles are strongly embedded for the samples at a higher Cu concentration and Cu doped ZnO, where particles are absent, is obtained until ≈ 3 at.% (see also Figure 5.2 and Figure 5.5). As a result of the low loading with Cu and the likely coverage of Cu metal particles with ZnO, the N_2O-RFC values might be dominated by redox active sites related to ZnO rather than Cu oxidation. In addition, as can be deduced from the very low Cu surface areas observed, a strong interfacial contact and interaction is evident, but this again is different for the two series due to their origin and synthesis concepts, and varies in both series dependent on the Cu content present in the samples.

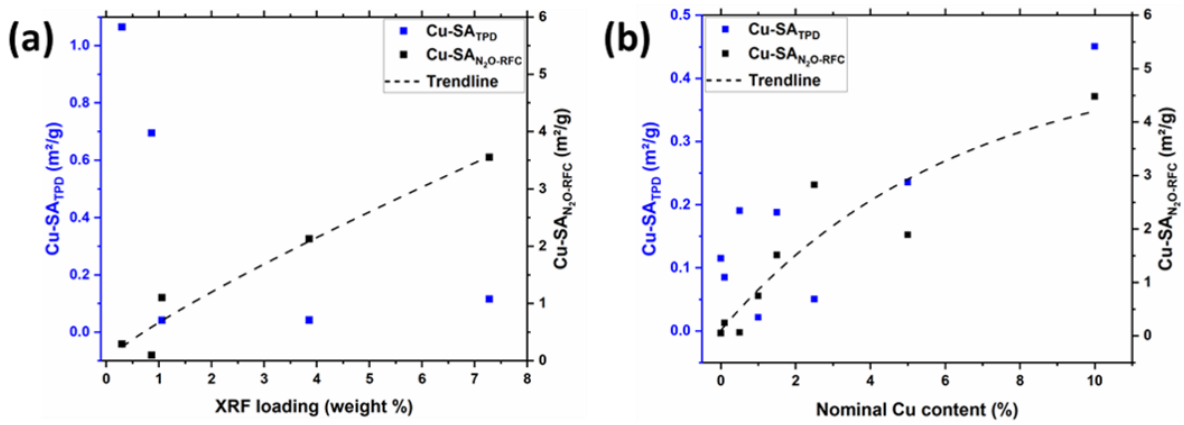

Figure 5.6: Cu surface area determination by H_2-TPD (blue) and N_2O-RFC (black) for (a) the Cu-I series and (b) the Cu-C series. The dashed lines are guides to the eye.

5.4.1.4 Optical band gaps determined by UV-vis measurements

In addition to the structural and surface properties of the samples, the influence of the various Cu loadings and different synthesis strategies on the band gap was investigated by diffuse reflectance UV-vis spectra. To this end, the ZnO band edges were extrapolated in the appropriate Tauc plots (see figure SI 5.18, page 90, for an example). It should be noted that this value for the band gap only denotes a band gap for an optical transition and is not necessarily equivalent to the band gap derived from an electronic band structure. Furthermore, in case of some samples, we observed that the reflectance was significantly un-flat after the large decrease associated with the band gap, which may indicate the presence of states in what we here denote as the "band gap". This was especially the case for samples with higher Cu content and in reducing conditions (see figures SI 5.18 and SI 5.19, page 90, for examples). In general, the band gap can be changed by modification of the ZnO support (creation of acceptor and donor states), or by transfer of electron density between the components of the system. In Figure 5.7, the optical band gaps of the samples studied at 230 °C and under different gas phases are presented. It becomes evident that the optical band gap of ZnO decreases with increasing concentration of Cu in the sample, both in case of the oxidised and the reduced state. This effect is more pronounced for the Cu-C series than for Cu-I. Furthermore, the impact of reduction on the optical band gap is more severe in case of the samples with higher Cu loading, especially in case of the Cu-C samples. It should be noted that in the Tauc plots for the Cu-C samples with a higher loading, additional edges appear in the relevant region,

which may be explained by the creation of defect states in the band gap of ZnO (see figure SI 5.19, page 90, for the Tauc plot of reduced 9.65Cu-C as an example).

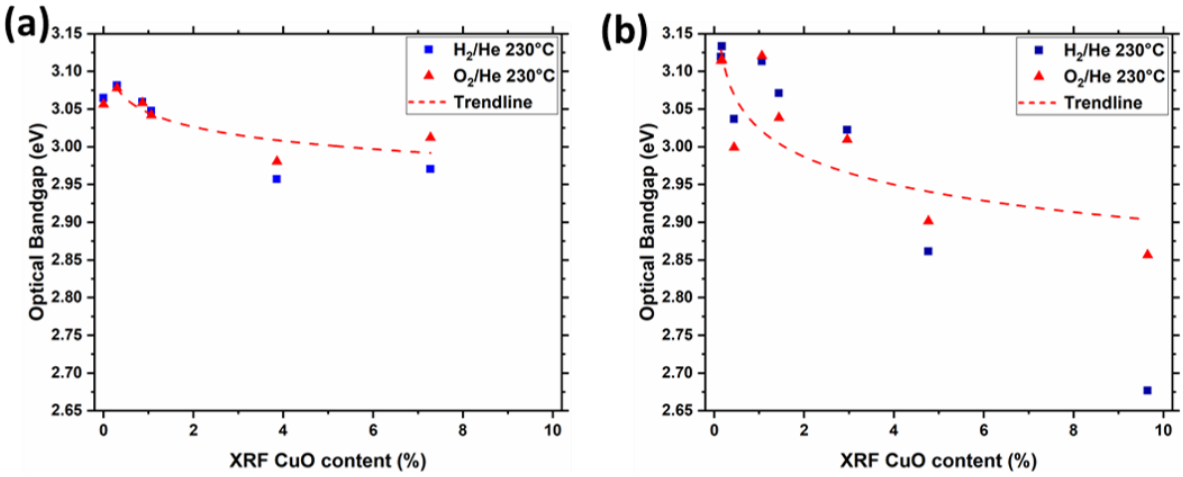

Figure 5.7: UV-vis determined optical band gaps of (a) the Cu-I series and (b) the Cu-C series at 230°C in reducing and oxidising gas feeds.

These results can be rationalised in view of calculations on Cu-doped ZnO,[52] which qualitatively explain the observed red shift by the interaction of the Cu 3d with the O 2p orbitals leading to a down-shift of the conduction band. However, it has to be noted that most band gap calculations found in the literature systematically underestimate the band gaps of Cu-doped ZnO and a more detailed analysis remains elusive[52,53].

5.4.2 Catalytic performance and Conductivity

5.4.2.1 Changes in reaction rate with Cu content

The thorough analysis of the samples by complementary techniques has shown that the addition of Cu to ZnO affects the structural and electronic properties. Depending on the synthetic strategy, these effects are differently pronounced. In general, the characterisation revealed pronounced differences between the samples depending both on their synthetic history as well as on their Cu content. Finally, the impact of the different preparation conditions and Cu loading on their catalytic performance in the rWGS reaction is elucidated. A meaningful interpretation of the catalytic activity is strongly dependent on the way the rates are normalised. To show the trends from different perspectives, the catalytic activities of the samples were normalised by the catalyst weight, BET surface area, and Cu-content. The data for the two series are presented in Figure 5.8 for a reaction feed composition of 1:3:6 CO_2:H_2:N_2. The corresponding data for

the 1:2:7 feed composition containing a smaller proportion of H_2 can be found in figure SI 5.30 (page 97). Additionally, a normalisation of the CO production rates by the apparent N_2O-RFC-derived surface area was investigated. However, since this method of determining a Cu surface area is to be treated with caution (as mentioned above), especially in case of samples with such low Cu content, the results gained by this normalisation will not be discussed further here. Instead, these data are provided in the supporting information (figures SI 5.32 and SI 5.33, page 99-100).

Figure 5.8(a) shows the conversion of the samples normalised by catalyst weight. An almost linear increase in CO production rate with increasing Cu content is observed for the Cu-C series. The reaction rate for the Cu-I series is comparable with the Cu-C series up to about 1% Cu loading, however, for higher loadings the reaction rate for the Cu-I stays almost constant. The CO rates normalized to the BET-SA values in Figure 5.8(b) resemble the trends observed in Figure 8(a), but exclude dispersion effects which would alter the number of reaction sites per g of catalyst. The Cu-C series again follows a linear trend and the Cu-I series saturates again with higher Cu-content.

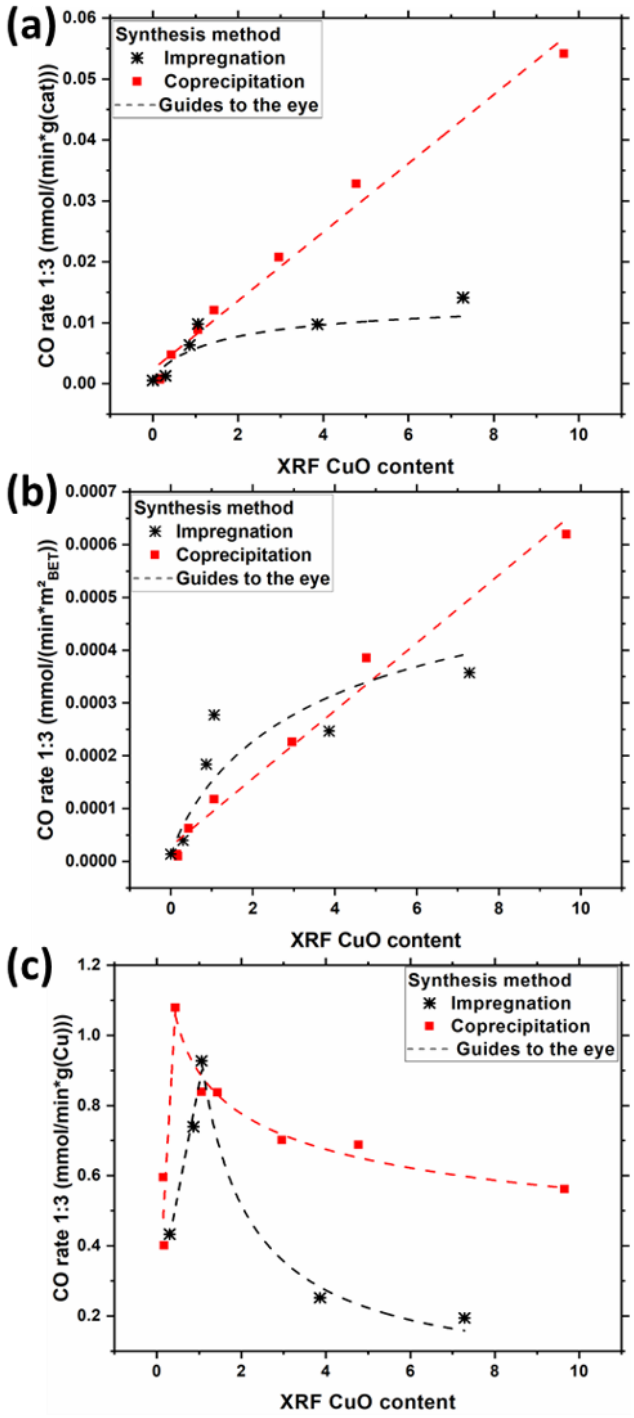

Figure 5.8: CO production rate per g catalyst (a), per m² catalyst surface area (BET) (b) and per g Cu(c) in the 1:3:6 CO_2:H_2:N_2 feed composition as a function of Cu content. All dashed lines are guides to the eye.

In case the CO production rate is normalized on the Cu mass (Figure 5.8(c)) a similar overall trend is observed for both series. Upon increase of the Cu content the rate increases at first, and decreases with even larger Cu content. However, the position of the maximum (0.44 % for Cu-C and 1.06 % for Cu-I) as well as the degree of reduction of the rate at high Cu coverage differ. The latter is much more pronounced for the Cu-I series. In general, the

rates increase with Cu content when the amount of Cu in the sample is overall very low but follows a decreasing trend for the samples with higher Cu content, finally reaching a plateau. The CO rates normalized to the Cu content of the samples express the catalytic efficiency of the integrated Cu. That means that in general and after reaching a certain concentration of Cu in the sample, finely dispersed particles with a large interfacial contact seem to be beneficial, and generally the efficiency decreases with ongoing particle formation. However, due to the intrinsic high dispersion of Cu in case of the Cu-C series, their efficiency is generally higher (compared to the Cu-I series) and stabilizes towards higher Cu loadings.[54,55] Overall these results again highlight the differences of the samples as a consequence of their Cu content and their synthetic history. Different behaviours are observed for the samples with low and high Cu loading, and whether they were generated by impregnation or coprecipitation.

In summary, coprecipitation leads, independent of the normalization method, to more active catalysts, which is interpreted as more efficient implementation of Cu predetermined by the synthesis strategy. Further, the intrinsically different Cu-ZnO interface in the Cu-C series samples, with differently embedded Cu particles (as a result from changing the synthesis method from impregnation to co-precipitation) seems to lead to more active catalysts, particularly at higher Cu-contents. Interestingly, the expansion of the lattice parameter *c* (Figure 5.2, pronounced for low Cu-contents) and the underlying cause behind it (e.g., incorporation of Cu ions into the ZnO lattice) does not lead to an increased activity, which is evidenced by 9.56Cu-C following the linear trend. This indicates that the impact of Cu-ions as possible dopants in the ZnO structure seems to be negligible and the active structure focuses directly on the Cu-ZnO interface (strongly embedded Cu in ZnO, as evidenced by the low H_2-TPD values). This stands in contrast to the impact of Al-ions as dopant in ZnO (Figure 5.1(b)) significantly enhancing the catalytic activity in the rWGS reaction and methanol synthesis. This may be due to the differences in electrons that may be donated from Al^{3+} in comparison to incorporated Cu ions, or differences in size mismatches of the dopant ions with the available sites.

5.4.2.2 Changes in reaction rate upon feed change

As mentioned above, the reaction rates were also measured at an alternative feed composition (besides 1:3:6 CO_2:H_2:N_2, also 1:2:7 CO_2:H_2:N_2) where the H_2:CO_2 ratio was

varied. The trends of the rates with respect to the Cu-content were almost identical (figure SI 5.30, page 97), but the absolute rates differ. The different gas feeds were employed in order to visualise the impact of a variation of the CO_2 to H_2 ratio on the rates, since this was expected to produce changes in catalytic performance as well as in the conductivity.

Figure 5.9(a) shows the CO rate differences between the applied feeds (subtracted from each other to have access to the delta-rates as function of the Cu content and the synthesis strategy, respectively). The delta-rates for the Cu-I series increases linearly in the low-loading regime and saturates already at ca. 4 wt. % of Cu. The increase in activity between the feeds is more strongly pronounced for the Cu-C series, with an almost linear increase until the high Cu-contents (slightly saturating at ca. 9.5 wt.-%).

Additionally, the reaction orders in CO_2 and H_2 determined in a parallel reactor setup are given in Figure 5.9 (b) and (c). It becomes evident that while there is not a lot of variation in the reaction orders within each series, the reaction order in CO_2 is slightly higher in case of the Cu-I series (however, it should be noted that this analysis lies within the errors corresponding to a 95 % confidence interval). It should also be added that the conversion of the samples was quite low in general (the conversion calculated from the CO content of the exit streams was < 5% for all samples) which may explain the overall rather low reaction orders, since limiting conditions were probably not reached.

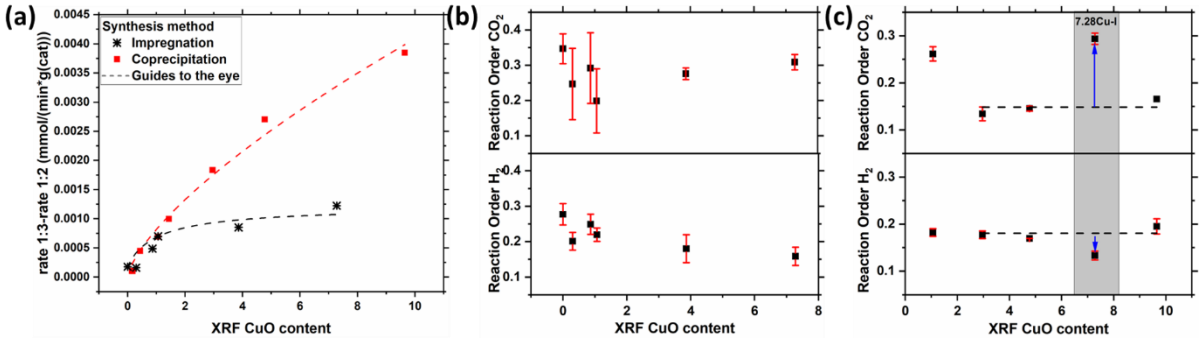

Figure 5.9: Difference in CO production rates per g catalyst determined in the MCPT setup(a), and reaction orders in CO_2 and H_2 for the Cu-I series (b) and the Cu-C series (c) samples determined in a parallel reactor setup. In (c), the corresponding values of 7.28Cu-I are given as a reference, and the horizontal broken line serves as a guide for the eye representing the Cu-C samples. The error bars designate 1 standard deviation. The 9.65Cu-C CO_2 reaction order was derived from only two points of the ln/ln plot since the third data point greatly deviated from the observed trend and therefore no error bars are shown. The error bars for this sample along with the value derived from a three point analysis are given in the supporting information (figure SI 5.25, page 94).

These results show that the change of the reaction rate to the H_2 content of the feed is correlated with the amount of Cu present in the sample. However, this effect flattens off

when the Cu content is increased. The overall lower rate differences exhibited by the Cu-I series may be explained by the slightly lower reaction order exhibited by this series, as shown in Figure 5.9(c), and seems rather to be connected to the CO_2 activation and less to the H_2 activation. Furthermore, the slope of the near-linear increase (observed at higher Cu loadings) in the rate differences of the two series is appreciably different. The slope (or the profile) indicates how much CO is produced per amount of Cu per minute, this means that within the two sample series, the activity of Cu is different. Again, this analysis revealed differences in the samples depending on the Cu content, and on the synthetic method used.

5.4.2.3 Changes in conductivity upon feed change

The relationship of electronic properties and catalytic activity in the reduction of CO_2 of the samples was measured *operando* under rWGS conditions after activation (523 K). This has the potential to identify a possible property-activity correlation previously unknown. This correlation can be understood by the fact that the conductivity of semiconductors is a sensitive probe for changes of the electronic structure (also for, e.g., shallow donor states within the band gap).[19,56] Optical band gap measurements have already indicated that the electronic structure of ZnO was altered by Cu. The suitability of the MCPT setup as a catalytic reactor was verified by comparing the rates measured in this setup with those obtained from an eight-fold parallel catalytic reactor setup (figure SI 5.22, page 92). Switching the feed between 1:3:6 and 1:2:7 CO_2:H_2:N_2 gives access to the role of the electronic properties influencing catalysis, in particular when considering the difference in the reaction rates (figure SI 5.31, page 98).

The graphs showing the conductivity and CO production rate as a function of the time-on-stream for the Cu-I series are presented in figure SI 5.40 (page 105), and in figure SI 5.41 (page 106) for the Cu-C series. The data obtained for selected samples (7.28Cu-I and 9.65Cu-C), which represent the general results of the investigations, are shown in Figure 5.10(a) (conductivity) and Figure 5.10(b) (CO production rate). In this figure, the data for the 1:2:7 and the 1:3:6 feed compositions are given. For the 7.28Cu-I sample an increase in both conductivity and the simultaneously measured CO production rate was observed upon increasing the H_2 ratio (feed conditions 1:3:6 CO_2/H_2/N_2). The activity and conductivity returned to the same value after returning to the 1:2:7 feed composition

afterwards (see figures SI 5.40 and SI 5.41, page 105-106). Both conductivity and conversion thus show the same response to changes in reducing strength of the gas feed mixture.

There is a decisive qualitative difference observed in case of the 9.65Cu-C sample (see Figure 5.10). In contrast to 7.28Cu-I, 9.65Cu-C exhibits a decrease in conductivity upon changing to the more reducing 1:3:6 gas feed composition, while still the CO production rate increases. While overall the absolute values for the conductivity and the CO production rate normalised per g of catalyst are within the same order of magnitude, this difference in qualitative behaviour of the conductivity is striking and indicates a difference in the way how ZnO and Cu interact as a consequence of the differing synthetic methods.

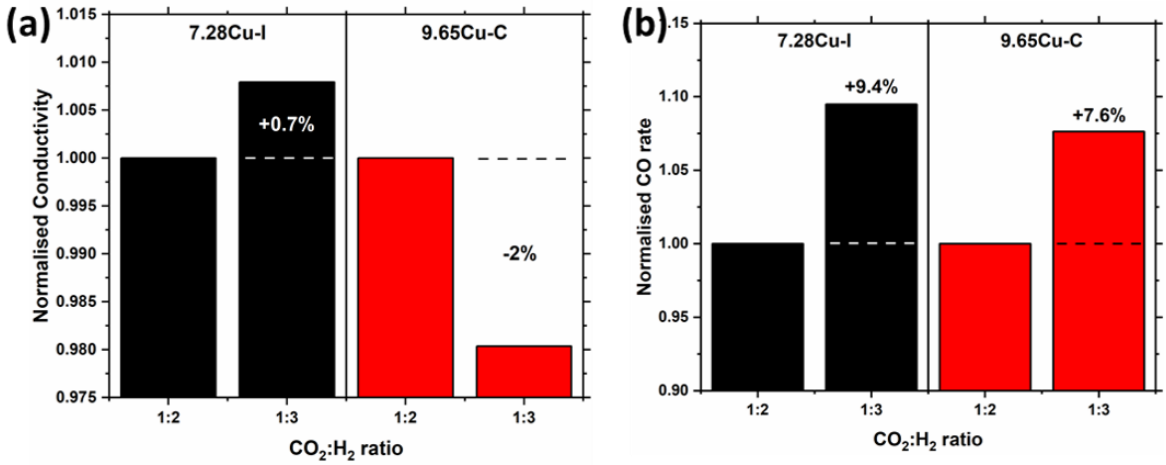

Figure 5.10: Conductivity (a) and CO rate (b) of selected samples in the differing gas phases (CO_2:H_2 1:2 and 1:3). The conductivity and rate values have been normalised to the respective values in the 1:2:7 CO_2:H_2:N_2 reaction feed.

Another interesting aspect of the MCPT results is that while the samples that contain Cu show a conductivity response when the rWGS feed composition is altered, ZnO-I and ZnO-C show no systematic change in conductivity as a response to this change (see figures SI 5.40 and SI 5.41, page 105-106). This implies that modification of ZnO with Cu does not only change the catalytic activity of the system with respect to the rWGS reaction, but it also leads to a qualitatively different response of the dielectric properties on reactive gas feed and establishes a relationship between catalytic performance and dielectric properties. Thus, conductivity has been shown as capable to qualitatively reflect differences in surface properties or the constitution of the catalysts. However, no direct

correlation between the absolute conductivity values and the samples' activities was found in this investigation (see the SI section 5.8.12.2, page 106).

An increase in conductivity when the reducing potential of the applied gas phase is increased is associated with n-type semiconducting behaviour.[57] Thus, the increase in conductivity linked to the increase in H_2 proportion in the feed for the Cu-I series can be explained by an n-type semiconducting behaviour in ZnO for this series. This behaviour could be expected for the intrinsic n-type semiconductor ZnO. Furthermore, also when investigating the MCPT conductivity of the samples in reducing and oxidising conditions, a reversible conductivity increase in reducing conditions was observed (see figures SI 5.42 - SI 5.45, page 107-109), in line with n-type semiconductivity. In contrast, since a decrease in conductivity is observed in the same case for the Cu-C series samples, ZnO in these samples is "less n-type", i.e., it has fewer or less mobile electrons, in the 1:3:6 CO_2:H_2:N_2 reaction feed than in the 1:2:7 reaction feed, or it could even conceivably be p-doped ZnO. It should be noted that such an effect related to the doping of ZnO by Cu as observed in case of the Cu-C series is a bulk effect. However, even in case of the Cu-C series samples, we observe a conductivity change of only about 2 % (see Figure 5.10 (a)). Therefore, it can be assumed that the bulk contributions to the conductivity changes overall are relatively small in this case, i.e., the conductivity change is dominated by the surface as a result of the applied gas phase.

However, while the samples in the coprecipitation series are crystallographically phase-pure in their precursor stage, even the samples with lower Cu loading may form several phases as a result of calcination and activation. Hence, since other parts of the samples than the ZnO may also take a role in determining the overall conductivity response, it is not possible to fully conclude on the type of majority charge carriers in the Cu containing samples of the C-series. Nevertheless, it is noteworthy that the conductivities of the ZnO samples that do not contain Cu are not significantly lower, if at all, than those of the Cu-containing samples (see figures SI 5.40 and SI 5.41, page 105-106). Also, the absolute conductivity values do not vary much between samples with rather low and comparatively high Cu contents within each series. This indicates that the other phases present in the samples, e.g., metallic Cu particles, perhaps do not influence the response of the MCPT method significantly in this case.

5.4.2.4 Apparent activation energy towards the rWGS reaction

In Figure 5.11, the apparent activation energies of some of the samples towards the reverse water-gas shift reaction are presented as determined from a temperature variant measurement in an 8-fold parallel reactor setup. The corresponding Arrhenius plots can be found in the supporting information (figure SI 5.23, page 93) along with the Arrhenius parameters (figure SI 5.24, page 93), which show a trend similar to the apparent activation energies. For the Cu containing samples, apparent activation energies between 82 and 120 kJ/mol were observed. It should however be noted that the typical rWGS activation energy for catalysts with industrially relevant Cu content were previously found to be ca. 60 kJ/mol only.[58,59] Therefore, we observe the apparent activation energy of our samples to be much higher than for samples containing a higher amount of Cu as is the case in the industrial catalyst. Furthermore, variations in the activation energies depending on Cu content were found with the activation energy showing a general decrease with increasing Cu loading, with the notable exception of the 1.06Cu-C sample which shows the overall lowest apparent activation energy out of all the samples tested. Furthermore, the different synthetic history of the samples also leads to differences in the apparent energy, with the activation energies of the impregnated samples appearing slightly higher than those of coprecipitated samples with a similar Cu content, which can also help to explain the overall comparatively higher CO production rates observed for this sample series.

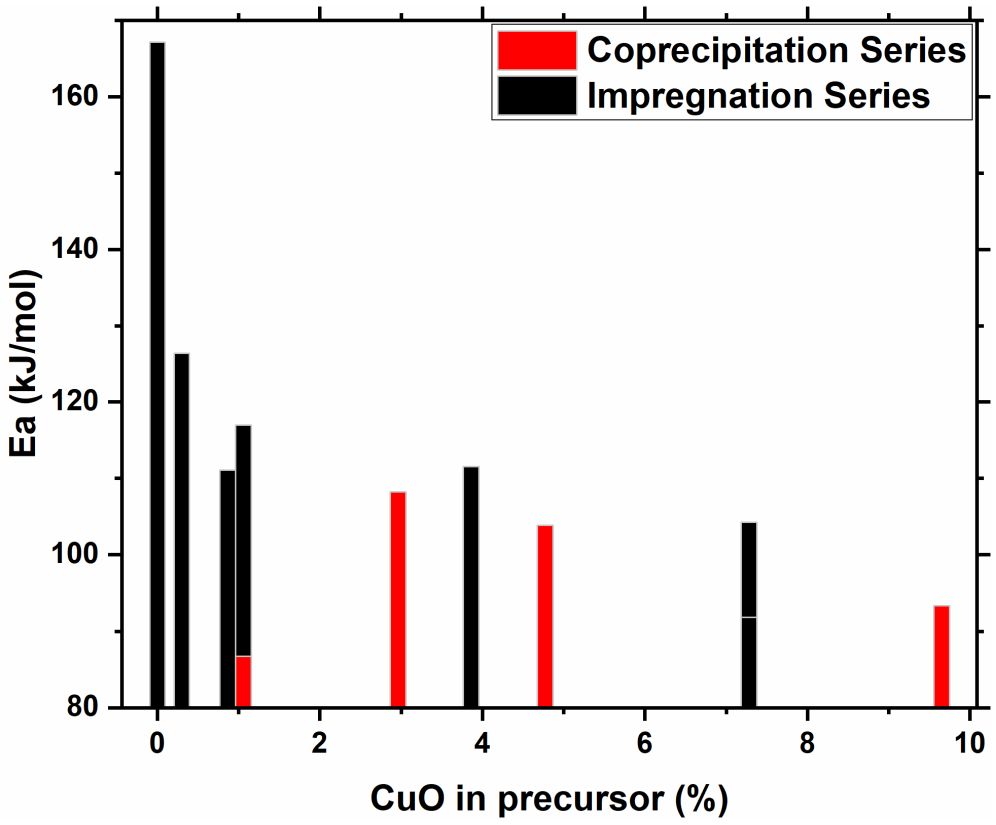

Figure 5.11: Activation energies determined in 8-fold parallel reactor setup.

5.5 Remarks and Conclusions

In conclusion, we investigated the approach of generating model catalysts for the industrial Cu/ZnO based catalyst applied in CO_2 reduction. The aim of this was to generate a system in which the proportion of interfacial Cu in comparison to Cu atoms present in larger metallic particles is increased, so that the effects of this interface would be able to be studied. Furthermore, a reduction in Cu content enables the application of experimental techniques such as MCPT, which is limited to low-conductive materials. In addition, the lower Cu content renders the modification of the ZnO support by Cu more prominent.

To achieve the above-mentioned goals, two synthetic strategies were applied, impregnation of ZnO using a dilution series of Cu citrate in aqueous ammonia, and coprecipitation from the Cu and Zn nitrates. Each series consisted of samples with varying Cu content. From a detailed characterisation of the resulting samples' structure, electronic properties, and reactivity in the rWGS reaction, it however becomes evident that the sample series were not homogeneous series where only the Cu content was altered. Instead, the observed characteristics varied non-continuously across the series.

This may have causes rooted in the synthetic approach: For example, the highly diluted Cu citrate solutions can have led to a shift from an impregnation to an underpotential deposition occurring for the samples of the Cu-I series with lower Cu content. This would be a consequence of a change of the pH of the impregnation solution with decreasing Cu citrate content. On the other hand, the discontinuities within the sample series can be formed through the lowering of the Cu content itself, e.g., the Cu-C samples with lower loading showed an incorporation of Cu into the ZnO lattice (up to the dissolution limit of Cu in ZnO). Overall, four different types of sample were therefore generated: Cu-I and Cu-C with low and high Cu content, respectively. These types, as explained above, all act differently, depending not only on their synthesis history, but also on their Cu content. It should be noted that some characterisation techniques, e.g., reactivity tests or conductivity measurements, are highly sensitive to this, while others are not as useful for detecting these differences.

The apparent activation energies of the investigated samples towards the reverse water-gas shift reaction were investigated and found to be in the range of 82-130 kJ/mol for the Cu containing catalysts. This is significantly higher than the apparent rWGS activation energies found for catalysts with a Cu/Zn ratio of more than 1,[58,59] as is employed in the industrial methanol synthesis catalyst.[8] This is especially the case for the Cu-I samples with low Cu content, which have an apparent activation energy of more than 110 kJ/mol. Furthermore, it should be noted that the activation energies are not equal across the sample series investigated here, but instead generally decrease with increasing Cu content. Therefore, it is clear that the reaction occurring on the samples investigated here is not equivalent to the reaction occurring on the industrial catalyst, and thus, the presented samples cannot be employed as models for this catalyst.

Another important finding of this work is the relevance of Cu as a modifier for ZnO in the industrial catalyst. Since the Cu-C series samples with low Cu content showed an incorporation of Cu ions into the ZnO lattice, these samples represent Cu-modified ZnO. However, also these samples showed an activation energy which was significantly higher than in case of Cu/ZnO catalyst with a high Cu/Zn ratio as is used in industry. Furthermore, the incorporation of Cu in ZnO only occurred when the Cu proportion was very small.

Therefore, Cu as a modifier for ZnO is unlikely to contribute significantly to the reactivity in Cu/ZnO catalyst with an industrially relevant Cu content.

All in all, the samples presented here, which were synthesised by either impregnation or coprecipitation, and had a low Cu content, were found to be unsuitable as model catalysts for the industrially applied Cu/ZnO-based catalysts with a Cu/Zn ratio of ≥ 1.[8] The approach of reducing the Cu content as a way to provide model samples for, e.g., the Cu-ZnO interface is therefore shown to be inadequate, and findings made on such samples can not be generally applied to the industrial catalyst system. However, it is clear that the obtained samples show some reactivity, e.g., towards the reduction of CO_2, and have interesting characteristics, and it would therefore be worthwhile to further explore their applications.

5.6 Acknowledgements

E.H.W. thanks the IMPRS (International Max Planck Research School) "Functional Interfaces in Physics and Chemistry" for funding and support. M. Hashagen is acknowledged for the BET measurements. P. Kube and E. Erdem are acknowledged for their help with catalytic measurements.

5.7 References

1 C. Álvarez Galván, J. Schumann, M. Behrens, J. L. G. Fierro, R. Schlögl and E. Frei, *Appl. Catal. B Environ.*, 2016, **195**, 104–111.

2 P. Tans and R. Keeling, Trends in Atmospheric Carbon Dioxide / Scripps CO2 Program, https://www.esrl.noaa.gov/gmd/ccgg/trends/ and scrippsco2.ucsd.edu/, (accessed 20 April 2020).

3 *BP Statistical Review of World Energy*, 2019.

4 H. Ritchie and M. Roser, Fossil Fuels, https://ourworldindata.org/fossil-fuels, (accessed 20 April 2020).

5 F. Asinger, *Methanol - Chemie- und Energierohstoff*, Springer, Berlin; Heidelberg; New York, 1st editio., 1986.

6 G. A. Olah, *Angew. Chem. Int. Ed. Engl.*, 2005, **44**, 2636–9.

7 G. A. Olah, A. Goeppert and G. K. S. Prakash, *J. Org. Chem.*, 2009, **74**, 487–98.

8 M. Behrens, F. Studt, I. Kasatkin, S. Kühl, M. Hävecker, F. Abild-Pedersen, S. Zander, F. Girgsdies, P. Kurr, B.-L. Kniep, M. Tovar, R. W. Fischer, J. K. Norskov and R. Schlögl, *Science*, 2012, **336**, 893–7.

9 J. B. Hansen and P. E. H. Nielsen, in *Handbook of Heterogeneous Catalysis*, eds. G. Ertl, H. Knözinger, F. Schüth and J. Weitkamp, Wiley VCH, 2008, pp. 2920–2949.

10 S. Zander, E. L. Kunkes, M. E. Schuster, J. Schumann, G. Weinberg, D. Teschner, N. Jacobsen, R. Schlögl and M. Behrens, *Angew. Chemie - Int. Ed.*, 2013, **52**, 6536–6540.

11 T. Lunkenbein, F. Girgsdies, T. Kandemir, N. Thomas, M. Behrens, R. Schlögl and E. Frei, *Angew. Chemie - Int. Ed.*, 2016, **55**, 12708–12712.

12 J. D. Grunwaldt, A. M. Molenbroek, N. Y. Topsoe, H. Topsoe and B. S. Clausen, *J. Catal.*, 2000, **194**, 452–460.

13 P. L. Hansen, J. B. Wagner, S. Helveg, J. R. Rostrup-Nielsen, B. S. Clausen and H. Topsøe, *Science*, 2002, **295**, 2053–2055.

14 J. W. Andreasen, F. B. Rasmussen, S. Helveg, A. Molenbroek, K. Ståhl, M. M. Nielsen and R. Feidenhans'l, *J. Appl. Crystallogr.*, 2006, **39**, 209–221.

15 R. Naumann D'Alnoncourt, X. Xia, J. Strunk, E. Löffler, O. Hinrichsen and M. Muhler, *Phys. Chem. Chem. Phys.*, 2006, **8**, 1525–1538.

16 A. V Tarasov, A. Yu, M. Friedrich, F. Girgsdies, R. Schlögl and E. Frei, *Appl. Catal. A Gen.*, 2020, **594**, 117460.

17 L. Zwiener, F. Girgsdies, D. Brennecke, D. Teschner, A. Machoke, R. Schlögl and E. Frei, *Appl. Catal. B Environ.*, 2019, **249**, 218–226

18 T. Lunkenbein, J. Schumann, M. Behrens, R. Schlögl and M. G. Willinger, *Angew. Chemie - Int. Ed.*, 2015, **54**, 4544–4548.

19 J. Schumann, M. Eichelbaum, T. Lunkenbein, N. Thomas, M. C. Álvarez Galván, R. Schlögl and M. Behrens, *ACS Catal.*, 2015, 3260–3270.

20 F. F. Vol'kenshtein, *The electronic theory of catalysis on semiconductors*, Pergamon Press Ltd., 1963.

21 M. Behrens, S. Zander, P. Kurr, N. Jacobsen, J. Senker, G. Koch, T. Ressler, R. W. Fischer and R. Schlögl, *J. Am. Chem. Soc.*, 2013, **135**, 6061–6068.

22 J. Schumann, T. Lunkenbein, A. Tarasov, N. Thomas, R. Schlögl and M. Behrens, *ChemCatChem*, 2014, **6**, 2889–2897.

23 J. Schumann, Dissertation, *Cu , Zn-based catalysts for methanol synthesis*, Technische Universität Berlin, 2015.

24 M. Heenemann, Dissertation, *Charge Transfer in Catalysis Studied by In-situ Microwave Cavity Perturbation Techniques*, Technische Universität Berlin, 2017.

25 M. Heenemann, M.-M. Millet, F. Girgsdies, M. Eichelbaum, T. Risse, R. Schlögl, T. Jones and E. Frei, *ACS Catal.*, 2020, **10**, 5672–5680.

26 M. Behrens, S. Zander, P. Kurr, N. Jacobsen, J. Senker, G. Koch, T. Ressler, R. W. Fischer and R. Schlögl, *J. Am. Chem. Soc.*, 2013, **135**, 6061–8.

27 R. Wang, A. W. Sleight and D. Cleary, *Chem. Mater.*, 1996, **8**, 433–439.

28 L.-S. Kau, K. O. Hodgson and E. I. Solomon, *J. Am. Chem. Soc.*, 1989, **111**, 7103–7109.

29 E. Frei, A. Gaur, H. Lichtenberg, C. Heine, M. Friedrich, M. Greiner, T. Lunkenbein, J. D. Grunwaldt and R. Schlögl, *ChemCatChem*, 2019, **11**, 1587–1592.

30 J. B. Bulko, R. G. Herman, K. Klier and G. W. Simmons, *J. Phys. Chem.*, 1979, **83**, 3118–3122.

31 R. G. Herman, K. Klier, G. W. Simmons, B. P. Finn, J. B. Bulko and T. P. Kobylinski, *J. Catal.*, 1979, **56**, 407–429.

32 J. C. Frost, *Nature*, 1988, **334**, 577–580.

33 K. Klier, *Appl. Surf. Sci.*, 1984, **19**, 264–297.

34 G. C. Chinchen and K. C. Waugh, *J. Catal.*, 1986, **97**, 280–283.

35 G. R. Apai, J. R. Monnier and M. J. Hanrahan, *J. Chem. Soc., Chem. Commun.*, 1984, 212–213.

36 Y. Okamoto, K. Fukino, T. Imanaka and S. Teranishi, *J. Chem. Soc. Chem. Commun.*, 1982, 1405–1407.

37 T. H. Fleisch and R. L. Mieville, *J. Catal.*, 1984, **90**, 165–172.

38 T. H. Fleisch and R. L. Mieville, *J. Catal.*, 1986, **97**, 284–285.

39 S. Mehta, G. W. Simmons, K. Klier and R. G. Herman, *J. Catal.*, 1979, **57**, 339–360.

40 R. Chatterjee, S. Kuld, R. Van Den Berg, A. Chen and W. Shen, *Top. Catal.*, 2019, **62**, 649–659.

41 G. C. Chinchen, C. M. Hay, H. D. Vandervell and K. C. Waugh, *J. Catal.*, 1987, **103**, 79–86.

42 R. M. Dell, F. S. Stone and P. . Tiley, *Trans. Faraday. Soc*, 1953, **49**, 195.

43 M. Eichelbaum, R. Stösser, A. Karpov, C.-K. Dobner, F. Rosowski, A. Trunschke and R. Schlögl, *Phys. Chem. Chem. Phys.*, 2012, **14**, 1302–12.

44 D. Kajfez, *Q Factor Mesurements Using MATLAB (R)*, Artech House, Norwood, 2011.

45 D. C. Dube, *J. Phys. D Appl. Phys.*, 1970, **3**, 1648–1652.

46 H. Looyenga, *Physica*, 1965, **31**, 401–406.

47 R. D. Shannon, *Acta Crystallogr. Sect. A*, 1976, **32**, 751–767.

48 M. Behrens, G. Lolli, N. Muratova, I. Kasatkin, M. Hävecker, R. Naumann d'Alnoncourt, O. Storcheva, K. Köhler, M. Muhler and R. Schlögl, *Phys. Chem. Chem. Phys.*, 2013, **15**, 1374–81.

49 S. Miao, R. Naumann d'Alnoncourt, T. Reinecke, I. Kasatkin, M. Behrens, R. Schlögl and M. Muhler, *Eur. J. Inorg. Chem.*, 2009, 910–921.

50 D. B. Williams and C. B. Carter, *Transmission Electron Microscopy - A Textbook for Materials Science*, Springer, Boston, MA, 1996, vol. 43.

51 S. Kuld, C. Conradsen, P. G. Moses, I. Chorkendorff and J. Sehested, *Angew. Chemie - Int. Ed.*, 2014, **53**, 5941–5945.

52 M. Ferhat, A. Zaoui and R. Ahuja, *Appl. Phys. Lett.*, 2009, **94**, 2007–2010.

53 S. Horzum, E. Torun, T. Serin and F. M. Peeters, *Philos. Mag.*, 2016, **96**, 1743–1756.

54 M. J. L. Ginés, N. Amadeo, M. Laborde and C. R. Apesteguía, *Appl. Catal. A Gen.*, 1995, **131**, 283–296.

55 C. S. Chen, J. H. Lin, J. H. You and C. R. Chen, *J. Am. Chem. Soc.*, 2006, **128**, 15950–15951.

56 N. A. Vorobyeva, M. N. Rumyantseva, R. B. Vasiliev, V. F. Kozlovskii, Y. M. Soshnikova, D. G. Filatova, A. E. Baranchikov, V. K. Ivanov and A. M. Gaskov, *Russ. J. Inorg. Chem.*, 2014, **59**, 403–412.

57 M. Eichelbaum, M. Hävecker, C. Heine, A. Karpov, C.-K. Dobner, F. Rosowski, A. Trunschke and R. Schlögl, *Angew. Chem. Int. Ed. Engl.*, 2012, **51**, 6246–50.

58 D. S. Newsome, *Catal. Rev. -Sci. Eng.*, 1980, **21**, 275–318.

59 H. Uchida, N. Isogai, M. Oba and T. Hasegawa, *Bull. Chem. Soc. Jpn.*, 1967, **40**, 1981–1986.

60 Y.-N. Xu and W. Y. Ching, *Phys. Rev. B*, 1993, **48**, 4335–4351.

61 S. Åsbrink and L. J. Norrby, *Acta Crystallogr. Sect. B Struct. Crystallogr. Cryst. Chem.*, 1970, **26**, 8–15.

62 R. W. G. Wyckoff, in *Crystal Structures 1*, Interscience Publishers, New York, Second Edi., 1963, pp. 7–83.

5.8 Supporting Information

5.8.1 Synthetic details

5.8.1.1 Impregnation series

Sample designation	Internal sample number (oxidised sample)	Nominal CuO amount	XRF CuO loading (wt.%)	Cu citrate/12.5 % NH_3 concentration
7.28Cu-I	24278	5%	7.28	94.52 g/L
3.86Cu-I	24279	2.5%	3.86	47.28 g/L
1.06Cu-I	24280	1%	1.06	18.90 g/L
0.86Cu-I	24281	0.5%	0.864	9.45 g/L
0.3Cu-I	24282	0.1%	0.3	5.73 g/L
ZnO-I	24277	0%	-	-

SI 5.1:Sample loadings and concentration of citrate solution for CuO/ZnO samples prepared by impregnation.

5.8.1.2 Coprecipitation series

Sample designation	Internal sample number (coprec. Sample)	Internal sample number (oxidised sample)	Nominal CuO amount	XRF CuO loading (wt.%)	m(Na_2CO_3) in 2 L H_2O (g)	m($Zn(NO_3)_2.6H_2O$) (g) in metal salt solution	m($Cu(NO_3)_2.3H_2O$) (g) in metal salt solution
9.65Cu-C	30295	30444	10.0%	9.65	339.15	200.89	18.1200
4.77Cu-C	30294	30438	5.0%	4.77	339.21	211.96	9.0590
2.96Cu-C	30293	30428	2.5%	2.96	339.19	217.58	4.5302
1.44Cu-C	30292	30421	1.5%	1.44	339.19	219.79	2.7179
1.06Cu-C	30291	30410	1.0%	1.06	339.21	220.89	1.8125
0.44Cu-C	30290	30392	0.5%	0.44	339.21	222.02	0.9056
0.17Cu-C	30289	30388	0.1%	0.17	339.20	222.92	0.1809
ZnO-C	30288	30387	0%	0.15 (30377)	339.20	223.13	-

SI 5.2: Sample loadings and weights of precursors for the coprecipitation series.

5.8.2 XRF

Sample	Sample amount (mg)
7.28Cu-I	101.2
3.86Cu-I	99.8
1.06Cu-I	98.7
0.86Cu-I	99.4
0.3Cu-I	100.5
9.65Cu-C	64.1
4.77Cu-C	95.1
2.96Cu-C	99.3
1.44Cu-C	98.7
1.06Cu-C	102.2
0.44Cu-C	98.8
0.17Cu-C	98.8
ZnO-C	75.5

SI 5.3: Amounts of sample used for XRF analysis.

5.8.3 ICP

To assure the preciseness of XRF as the method to determine the CuO content in our calcined samples, Inductively Coupled Plasma-Optical Emission Spectroscopy (ICP-OES) was performed on the Cu-I series samples. For this, each sample was dissolved in a mixture of 10 mL H_2O and 5 mL HNO_3 (65 % suprapur) while heating to ca. 250 °C at a maximum of 6 MPa. The resulting solutions were diluted to 50 mL using H_2O, and 200 µL instances of this were sampled and mixed with 50 µL HNO_3 and again diluted with water to 10 mL before sampling. The solutions were analysed in a Perkin Elmer Optima 8300 optical emission spectrometer in axial mode. For evaluation, commercial multielement standards were used and the data were analysed using the Syngistix software for ICP. In figure SI 5.4 (page 83), the results of the analysis are presented. The data of Cu/Zn ratios determined by ICP vs. Cu/Zn ratios determined by XRF fall on a straight line with a slope of about 1. This highlights that the XRF determined CuO contents are of high accuracy.

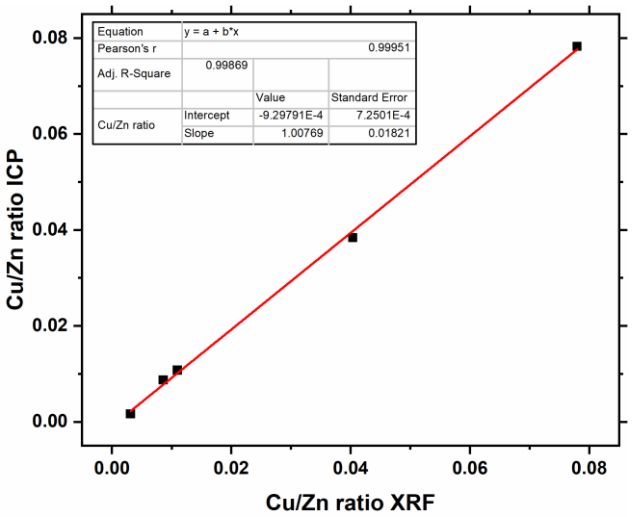

SI 5.4: Comparison of Cu/Zn ratios determined using ICP-OES and XRF.

5.8.4 BET

The BET (Brunauer-Emmet-Teller) surface area of the samples was investigated using N_2 adsorption at liquid nitrogen temperature and subsequent desorption in an Autosorb-68-MP (Quantachrome) 6 port BET setup. Prior to the measurement, around 100 mg of sample were heated to degas in vacuum.

In figure SI 5.5 (page 84), the BET surface areas of all calcined samples are presented. For the Cu-C series, the BET surface area was also determined for the uncalcined precursors, and the comparison of the surface areas of the precursors and calcined samples can be found in figure SI 5.6 (page 84). From the figures, it becomes evident that there is a general increase in surface area with increasing Cu content for all these series, especially in case of the calcined sample. The surface area of the Cu-C series increased significantly upon calcination. The BET surface area is decidedly higher for the Cu-C series than for the Cu-I series.

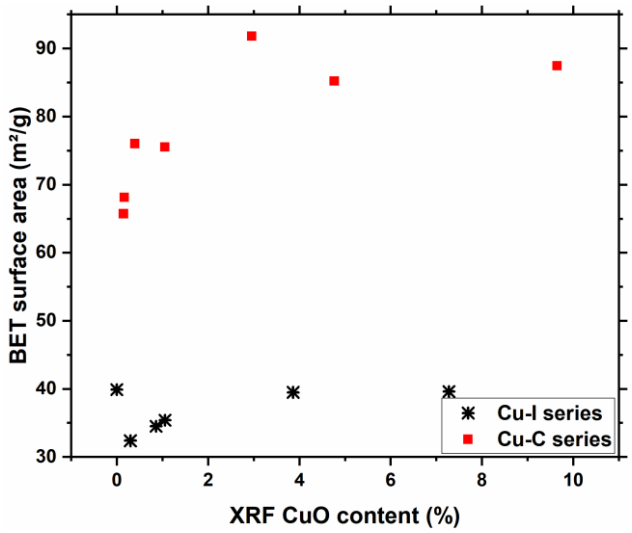

SI 5.5: BET surface area of both sample series (calcined samples).

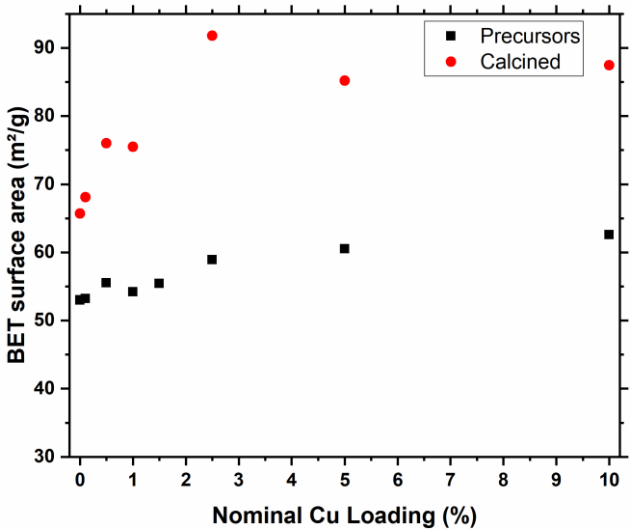

SI 5.6: BET surface areas of the Cu-C series calcined samples and precursors.

5.8.5 XRD

The full X-ray diffractograms for all samples are given in figures SI 5.7 and SI 5.10 (page 85-86). Close-ups around the most intense ZnO reflections as well as the region where CuO 111, the most intense reflection in the diffractogram of CuO, would appear are given in figures SI 5.8 and SI 5.11 (page 85-86). From the diffractograms, it becomes evident that most samples do not contain visible contributions from CuO, a notable exception are the Cu-I series samples with a CuO content > 1 % , e.g., the 7.28Cu-I sample's diffractogram which shows a small contribution by the CuO 111 reflection at around 2θ = 39°. This result can be explained by several interpretations, either the CuO reflections can be broadened into the background due to the small crystallite size of CuO in our samples, or it is possible

that there is no separate CuO phase present in these samples, but rather, the Cu content is present within the ZnO structure. Furthermore, the overall Cu content of the samples is quite low, which means that there is less contribution by Cu-containing phases to the diffractogram than by, e.g., the ZnO phase. Using Rietveld fitting, it was possible to estimate the CuO content in those samples where a CuO reflection was found. However, even with the best fit model, a small systematic discrepancy in the higher angle extension ("foot") of the ZnO 101 reflection exits. This discrepancy allows for the accommodation of about 1 wt.% CuO in the fit, even in the case of ZnO-I, since the CuO reflection is located in the foot of this reflection. For this reason, a base value of ca. 1 wt.% is obtained for the lower loading samples, while a linear correlation between Rietveld-based CuO amount and XRF results is obtained for higher loadings (figure SI 5.9, page 86).

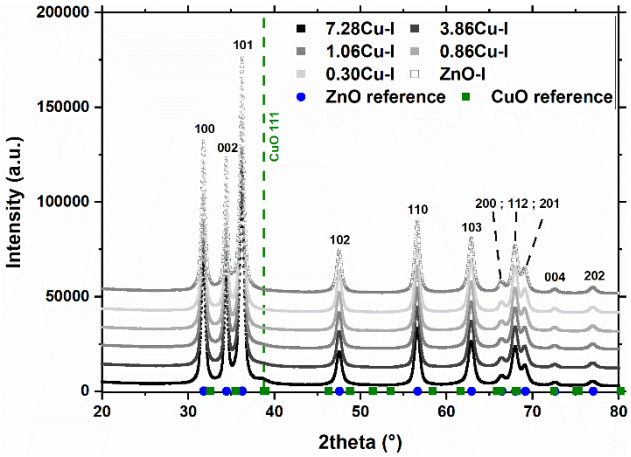

SI 5.7: Overview X-ray diffractograms of the Cu-I series samples. The ZnO[60] and CuO[61] references are given from literature data.

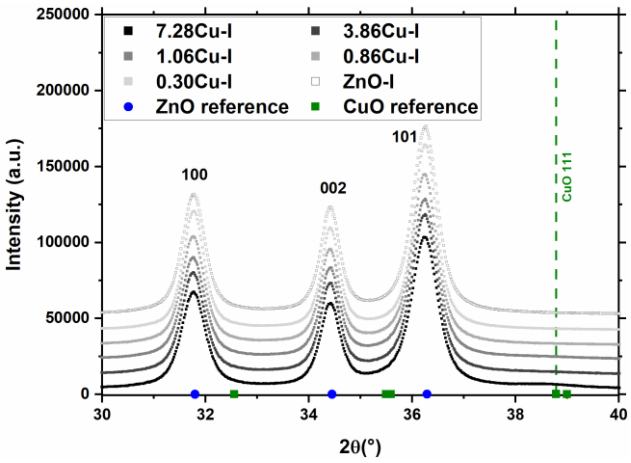

SI 5.8: Close-up of the X-ray diffraction patterns for the Cu-I series samples around the most intense ZnO features, including the region which would show the CuO 111 reflection (most intense).

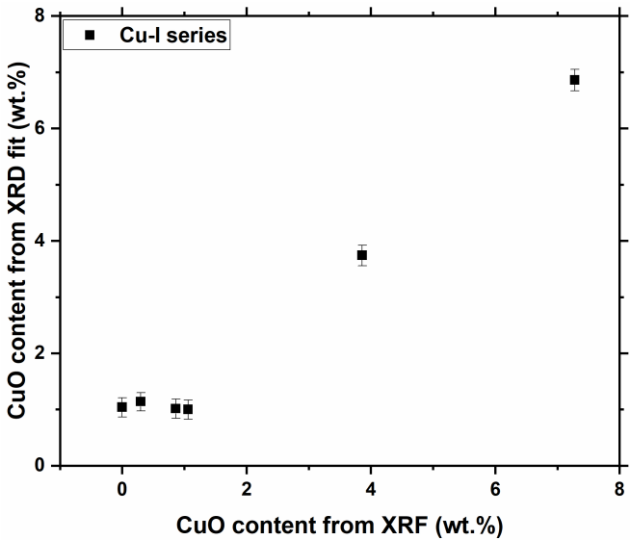

SI 5.9: CuO content determined from Rietveld fit of the Cu-I series diffractograms vs. CuO content determined by XRF.

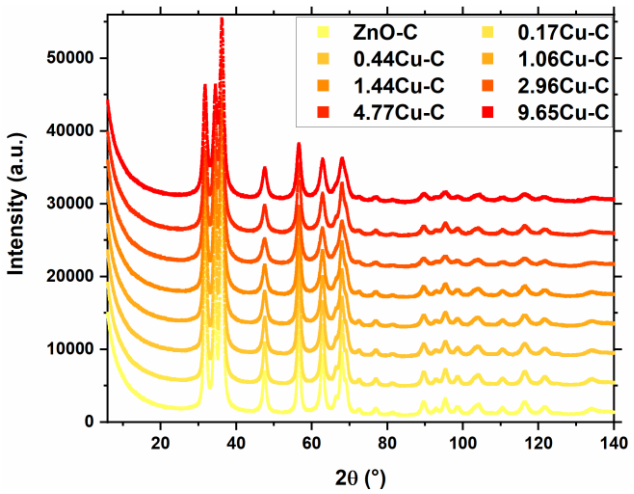

SI 5.10: X-ray diffractograms of the Cu-C series samples.

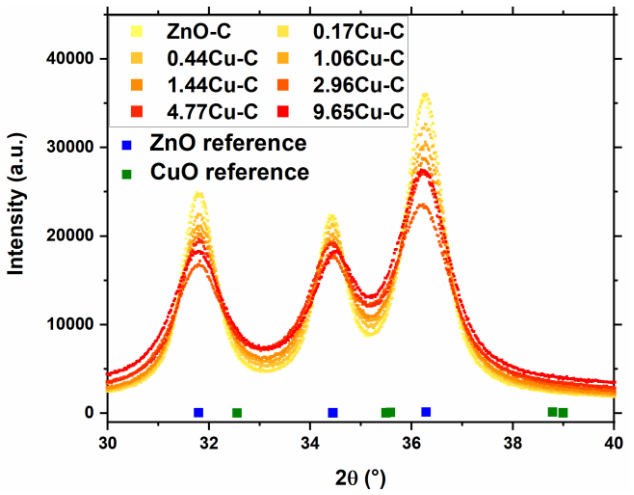

SI 5.11: Close-up of the X-ray diffractograms of the Cu-C series samples around the three main peaks of ZnO, including the region for the CuO 111 reflection. The references for ZnO[60] and CuO[61] are given as symbols.

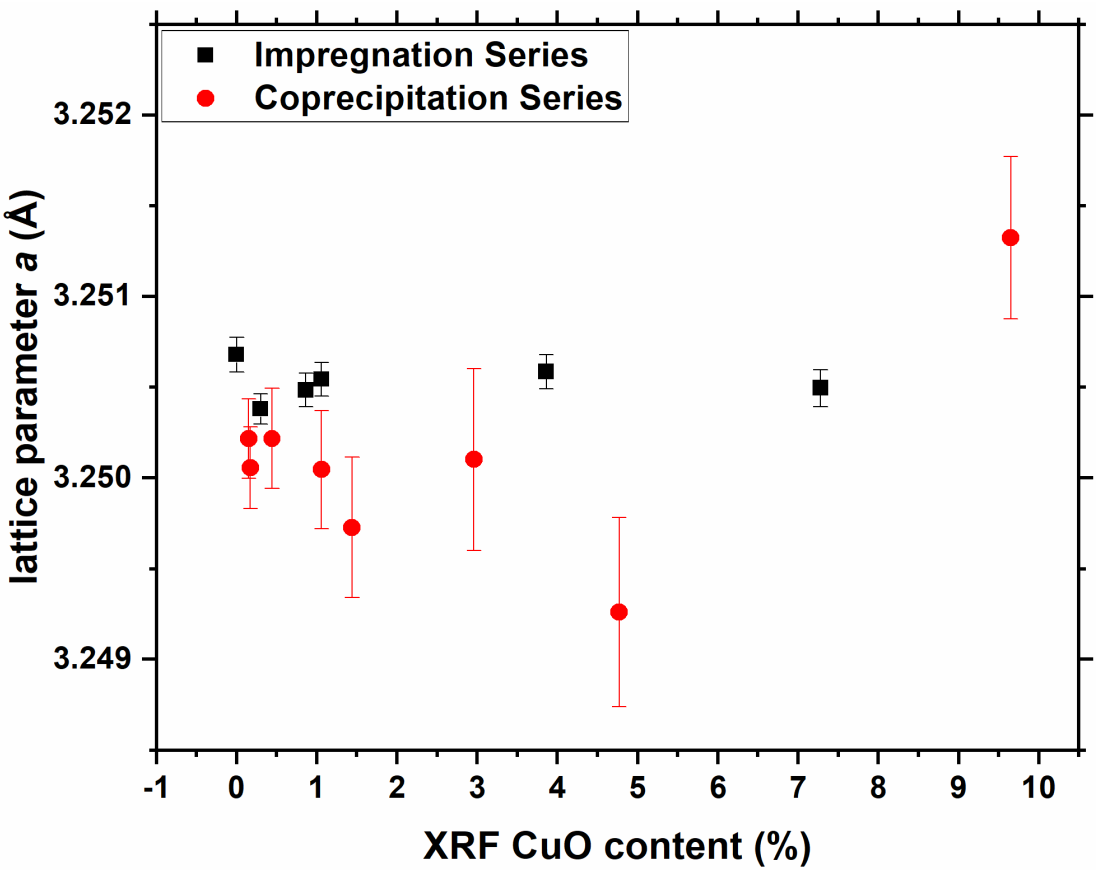

SI 5.12: Lattice parameter *a* for all samples as determined from the Rietveld fits.

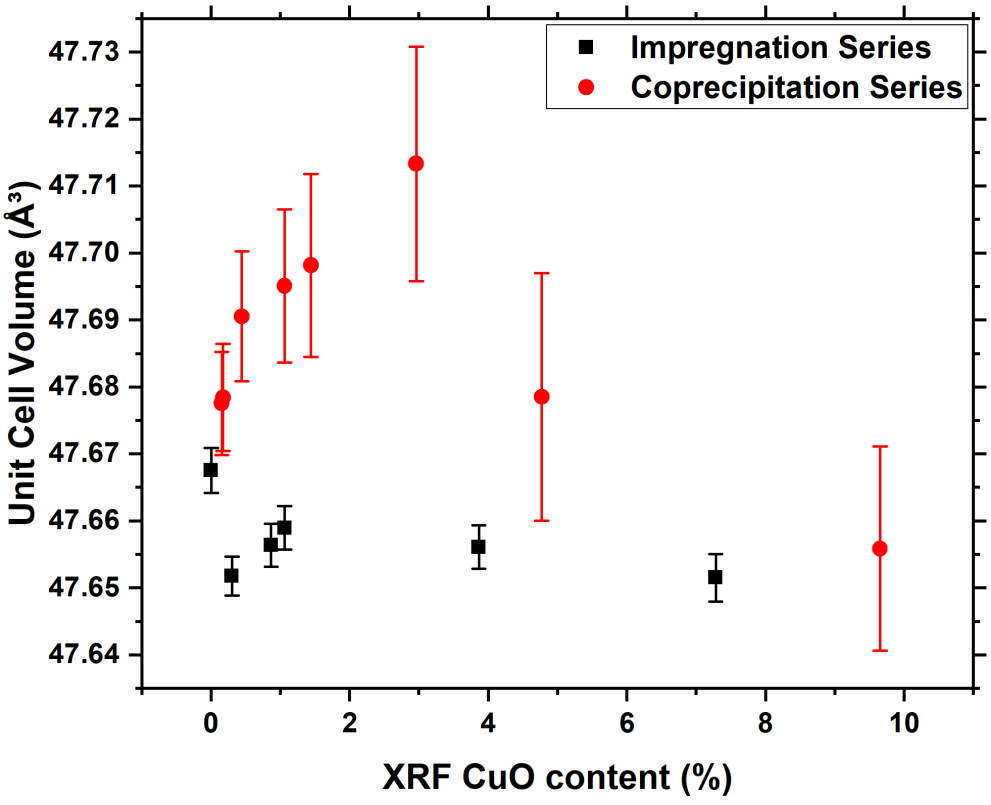

SI 5.13: Unit Cell Volumes calculated from the lattice parameters *a* and *c* determined from the Rietveld fits. The error bars designate 3 standard deviations.

Using an *in situ* X-ray diffraction setup (STOE Bragg-Brentano Theta/Theta diffractometer with attached gas supply system and an Anton Paar XRK900 high-temperature diffraction chamber), it was possible to investigate the powder diffraction patterns of three Cu-C series samples before and after reduction at room temperature, without exposure of the samples to air which would result in oxidation. In this way, it can be evaluated whether reflections belonging to Cu metal, e.g., the Cu 111 reflection at 2θ = 43.35°,[62] appear after the reduction treatment. The diffractograms of 1.06Cu-C and 2.96 Cu-C are given in figures SI 5.14 and SI 5.15 (page 88-89). There are no obvious differences between the diffractograms obtained before and after the reduction treatment. It has to be noted that the absence of Cu reflections does not exclude the presence of very small metallic Cu particles, because the reflections may be broadened into the background due to the small domain size. Also, the Cu content in these two samples is very low, lessening the contribution of Cu-species in these samples. In contrast, the diffractogram of 9.65Cu-C (figure SI 5.16, page 89) shows evidence for the presence of metallic Cu (e.g., there is a reflection appearing at 43.45°) after reduction.

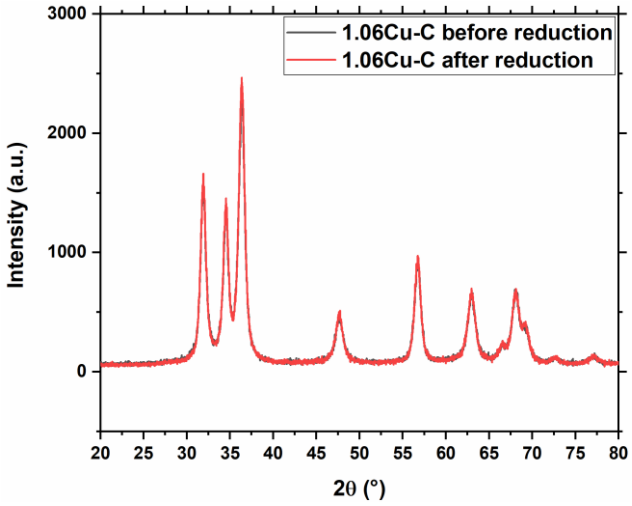

SI 5.14: XRD before and after reduction of the 1.06Cu-C sample.

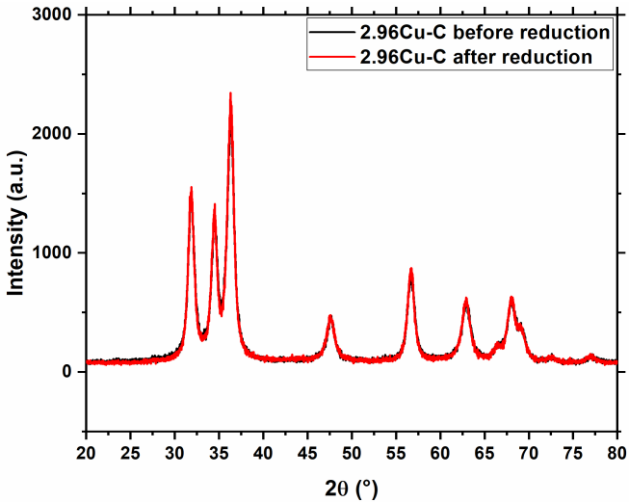

SI 5.15: XRD before and after reduction of the 2.96Cu-C sample.

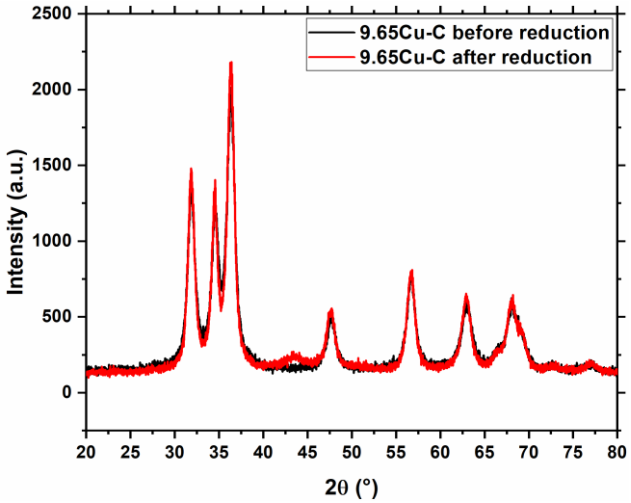

SI 5.16: XRD before and after reduction of the 9.65Cu-C sample.

5.8.6 Cu surface area determination

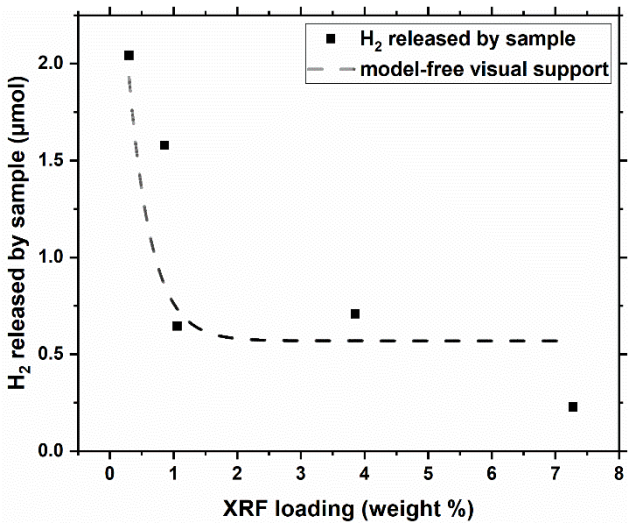

SI 5.17: H_2 released by samples during TPD experiment.

5.8.7 UV-vis

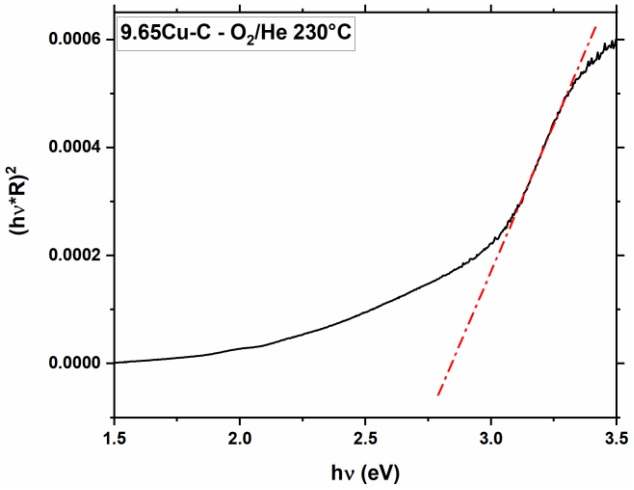

SI 5.18: Example Tauc Plot. Here, the data for 9.65Cu-C in its oxidised state at 230°C are presented.

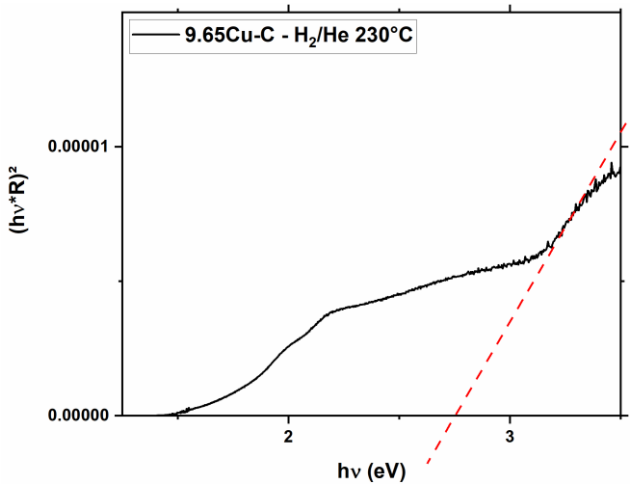

SI 5.19: Example Tauc Plot of 9.65Cu-C in the reduced state at 230°C.

5.8.8 Reactivity tests in an 8-fold parallel reactor setup

Sample	Sample weight [mg]	SiC weight [g]
0.86Cu-I	49.9	2.9510
3.86Cu-I	49.3	2.9465
0.3Cu-I	48.8	2.9628
1.06Cu-I	50.1	2.9504
ZnO-I	49.7	2.9574
7.28Cu-I (1st run)	49.0	2.9574
7.28Cu-I (2nd run)	50.4	2.9502
9.65Cu-C	49.7	2.9502
4.77Cu-C	49.4	2.9498
2.96Cu-C	49.9	2.9547
1.06Cu-C	50.0	2.9502

SI 5.20: Amounts of sample used for reactivity tests in 8-fold parallel reactor.

Sequence Nr.	CO_2:H_2:N_2 ratio	total flow per reactor [mL/min]	Temperature [°C]
1	0:1:19	30	250
2	0:0:1	30	230
3	1:1:8	10	230
4	1:1:8	20	230
5	1:1:8	30	230
6	1:1:8	10	230
7	1:1:8	10	210
8	1:1:8	10	200
9	1:1:8	10	220
10	1:1:8	10	240

11	1:1:8	10	230
12	1:2:7	10	230
13	1:3:6	10	230
14	1:1:8	10	230
15	2:1:7	10	230
16	3:1:6	10	230
17	1:1:8	10	230
18	0:0:1	30	230

SI 5.21: Experimental sequence for reactivity tests in the parallel reactor setup.

The comparability of the results obtained in the eight-fold parallel reactor ("Grimsel") to the catalytic data obtained in the MCPT setup was evaluated, with results presented in SI 5.22.

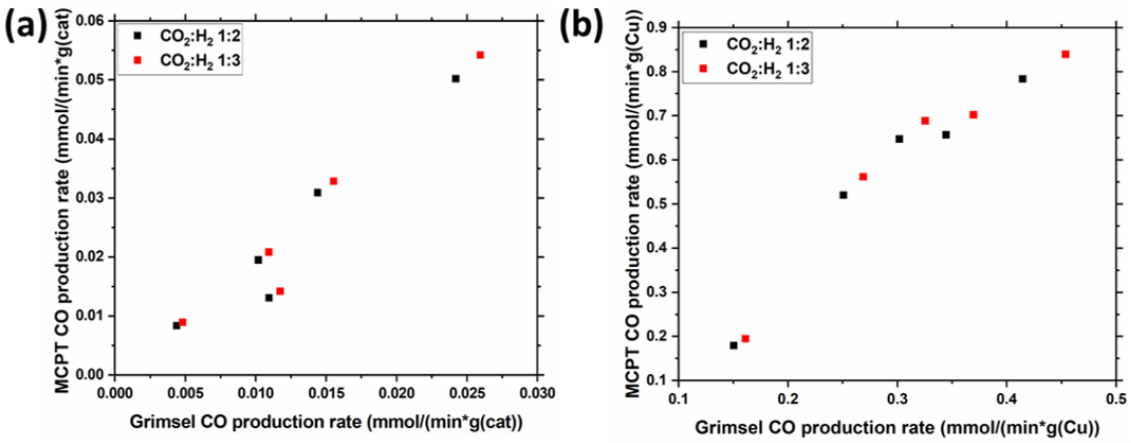

SI 5.22: Comparison of reaction rates determined in the MCPT setup and in the eight-fold parallel reactor setup.

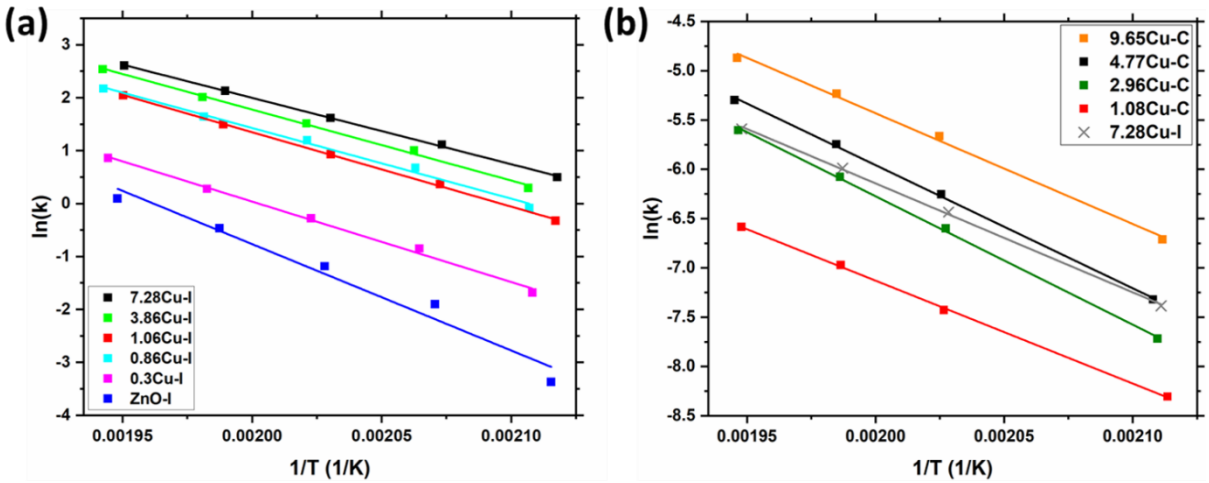

SI 5.23: Arrhenius plots (ln(k) vs 1/T) for the two investigations performed in the parallel reactor setup.

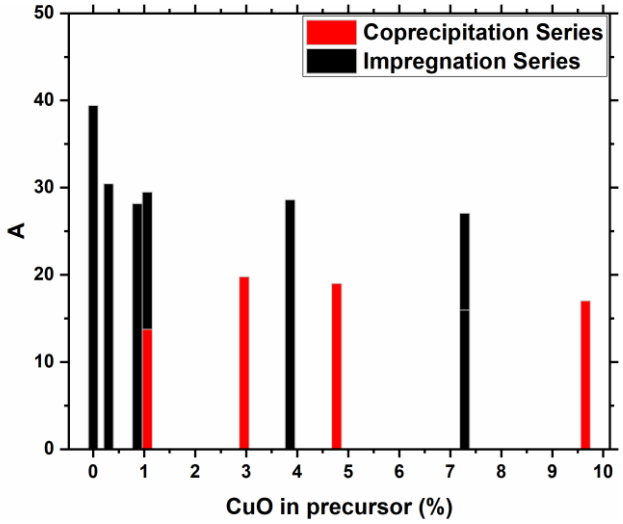

SI 5.24: Arrhenius parameters of the samples studied in the parallel reactor setup determined from figure SI 5.23 (page 93).

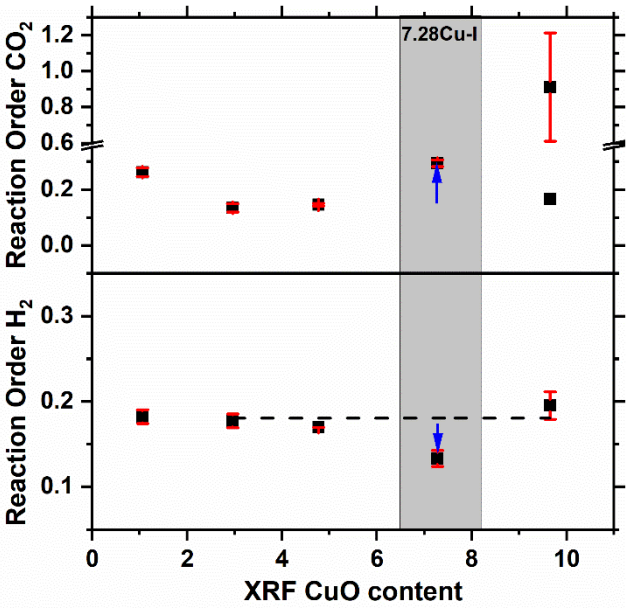

SI 5.25: Reaction orders in CO_2 and H_2 towards the rWGS reaction of the Cu-C series sample investigated in the 8-fold parallel reactor setup, as well as of 7.28Cu-I as a reference. The error bars designate 1 standard deviation. For the 9.65Cu-C sample, both the point derived from 2 points on the ln/ln plot (no error bars) and from the point including the outlier in the analysis (with error bars) are included.

5.8.9 TEM/EDX

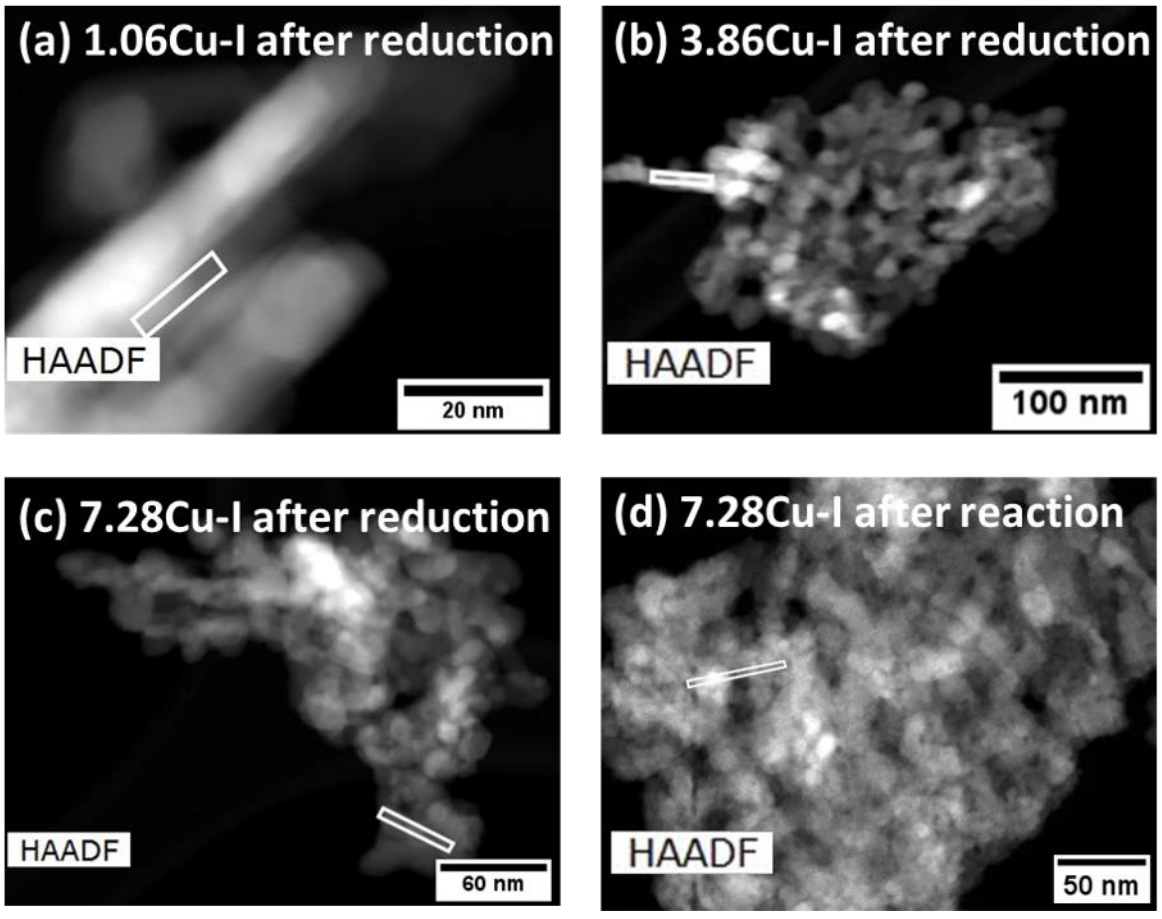

SI 5.26: HAADF images of Cu-I samples.

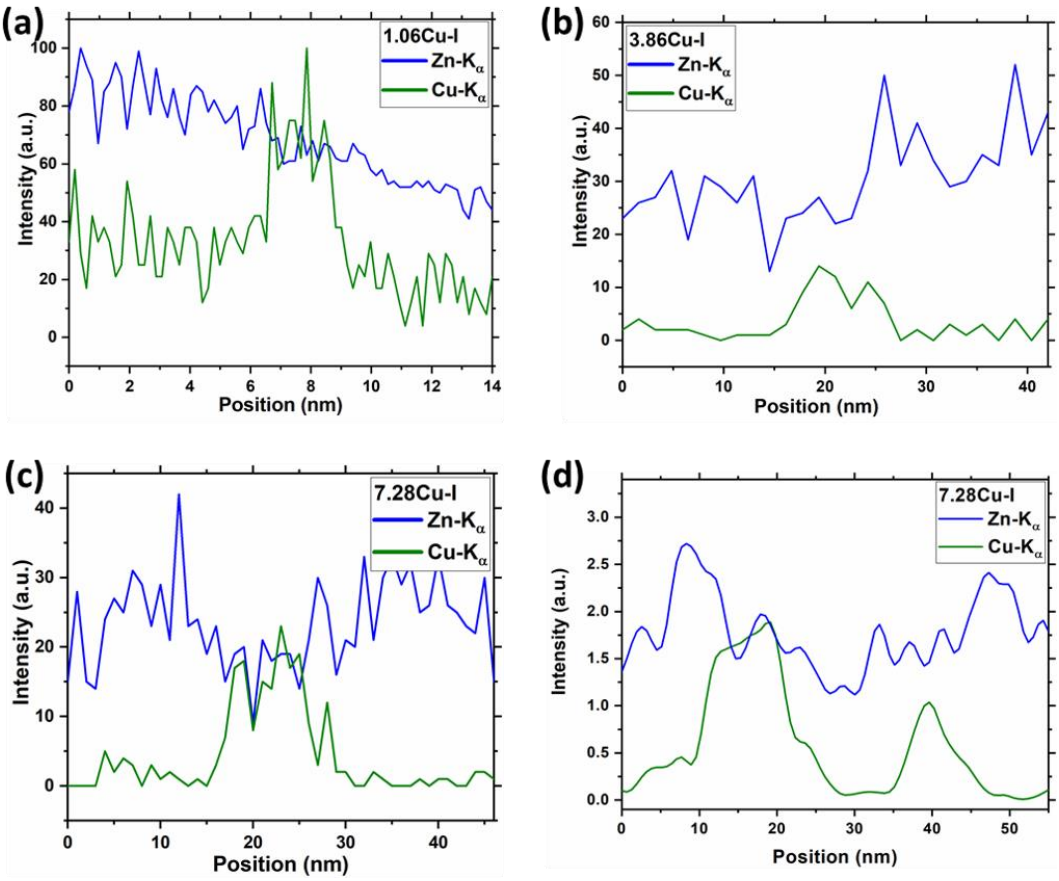

SI 5.27: EDX line scans of Cu-I samples after reduction (a-c) and after rWGS testing and re-reduction (d), corresponding to the lines indicated in Figure 5.4.

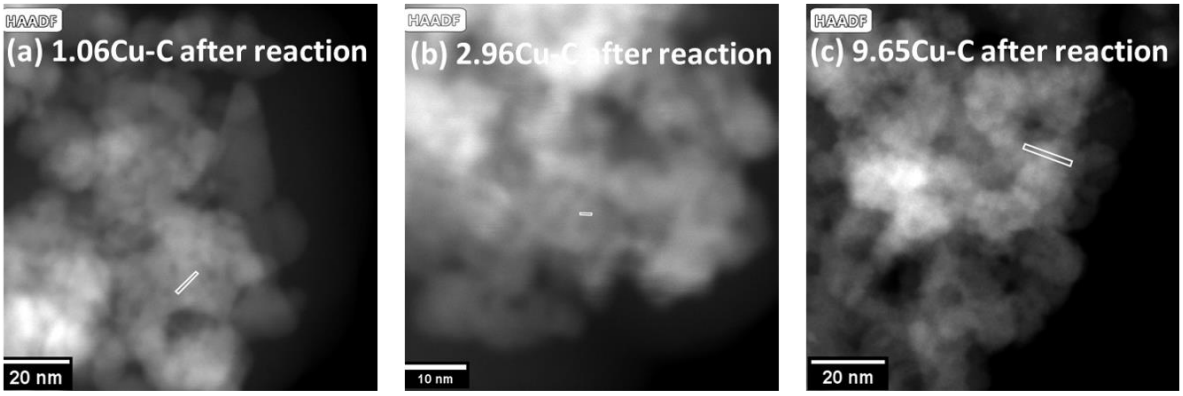

SI 5.28: HAADF images of Cu-C samples.

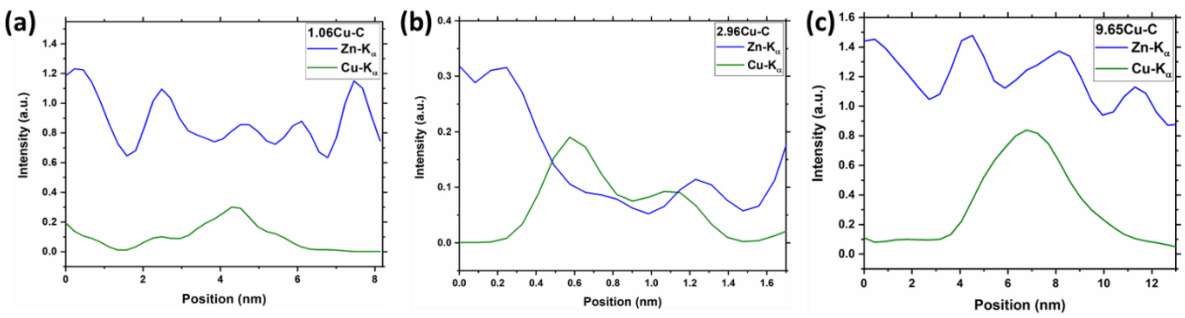

SI 5.29: EDX line scans after rWGS testing in parallel reactor and subsequent re-reduction, corresponding to the lines indicated in Figure 5.5.

5.8.10 Further reactivity data (obtained in MCPT setup)

In figure SI 5.30 (page 97), the CO production rates in the 1:2:7 CO_2:H_2:N_2 reaction feed normalised by catalyst weight, BET surface area, and Cu content are presented. While the CO production rates are lower, the observed trends are analogous to those observed for the 1:3:6 reaction feed already discussed in section 5.4.2.1.

Figure SI 5.31 (page 98) shows the differences in reaction rate differences between the two reaction feeds, normalised again by the catalyst weight, the BET surface area and the Cu content.

Figures SI 5.32 and SI 5.33 (page 99-100) present the catalytic data normalised by the N_2O-RFC derived surface area. While in the former figure, the data for an outlier (corresponding to the 0.44Cu-C sample) were removed for improved clarity, the latter figure includes these data for completeness.

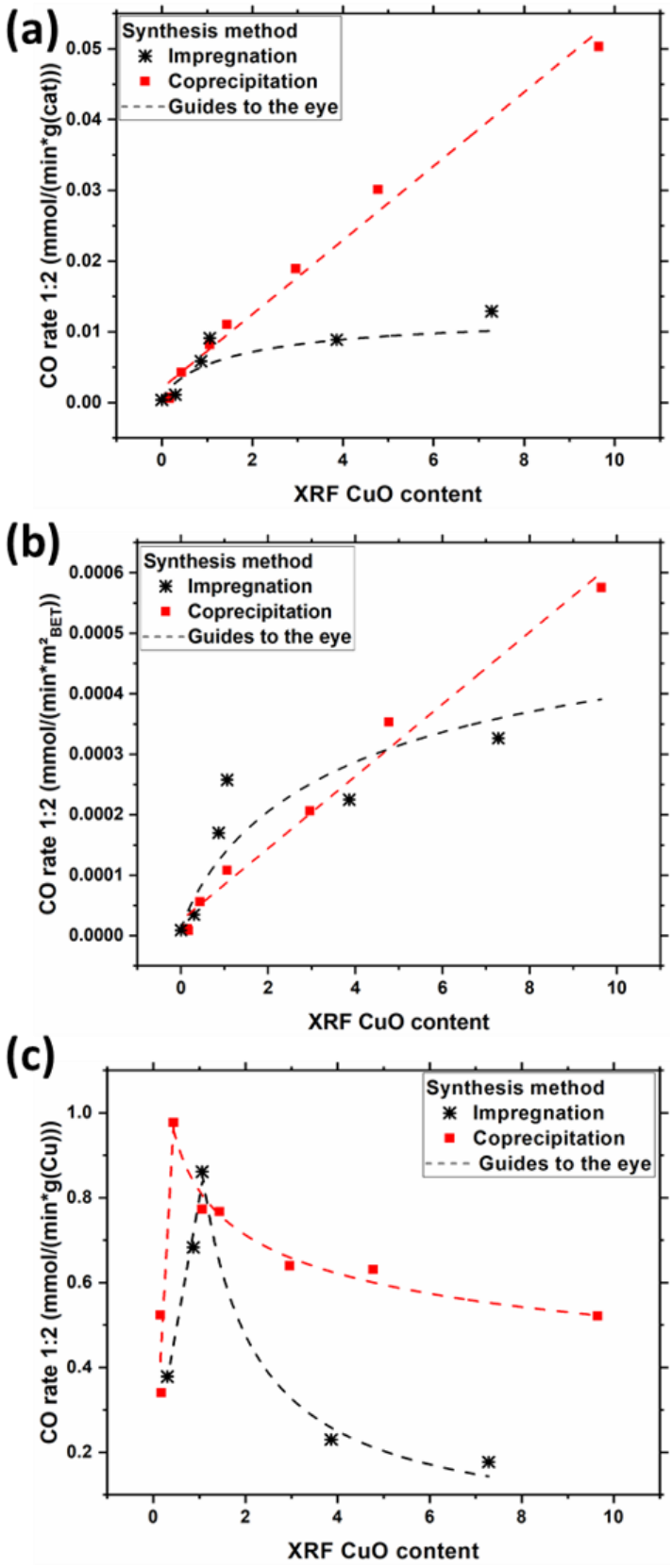

SI 5.30: CO production rate per g catalyst (a), per m² catalyst surface area determined using BET (b) and per g Cu (c) in the 1:2:7 CO_2:H_2:N_2 feed composition as a function of Cu content.

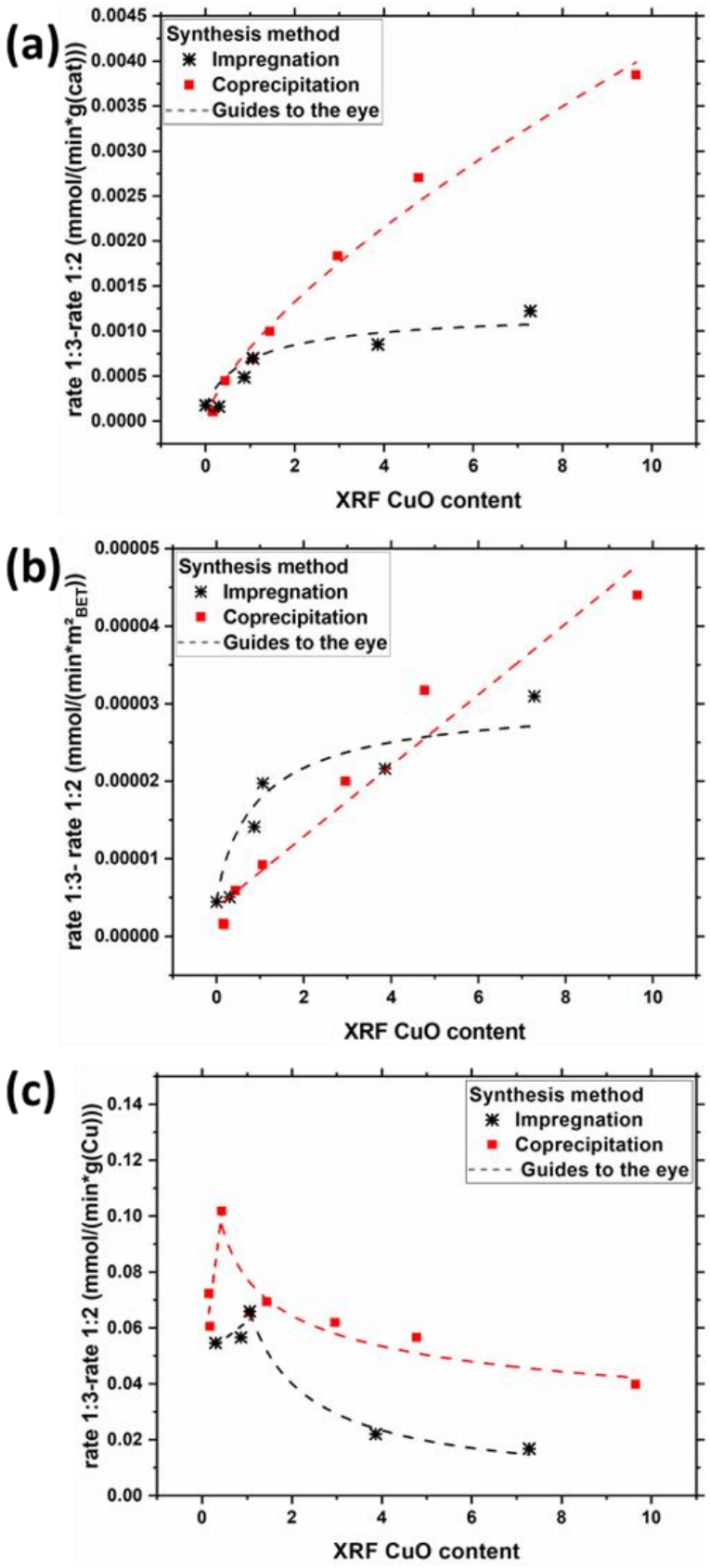

SI 5.31:Difference in CO production rates per g catalyst (a), per m² catalyst surface area (BET)(b) and per g Cu(c) of the 1:3:6 feed and 1:2:7 feed vs. the CuO content of the precursor

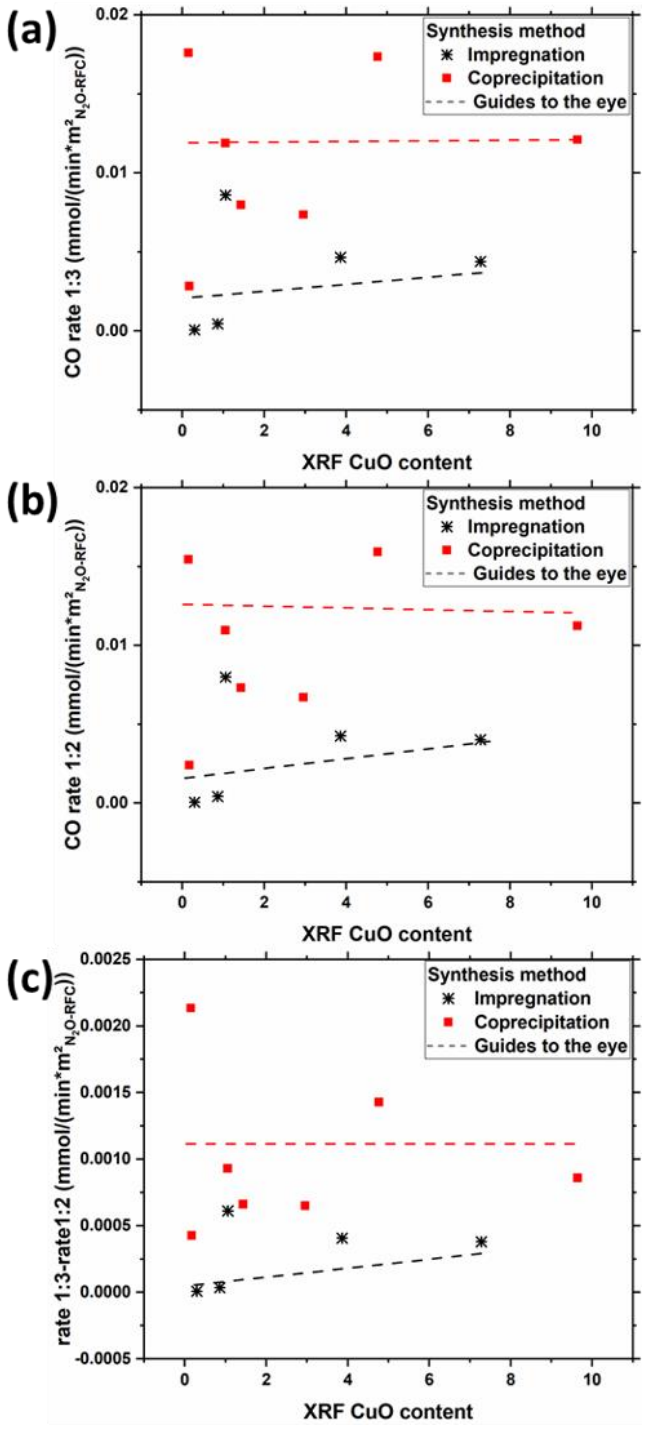

SI 5.32: N_2O-RFC normalised CO rates in (a) 1:3 and (b) 1:2 CO_2:H_2 containing reaction feed, and (c) the differences of the N_2O-RFC normalised CO rates between the two reaction feed, obtained in the MCPT setup including the outlier (0.44Cu-C). An outlier (0.44Cu-C) was removed for improved clarity, the full data sets can be found in figure SI 5.33 (page 100).

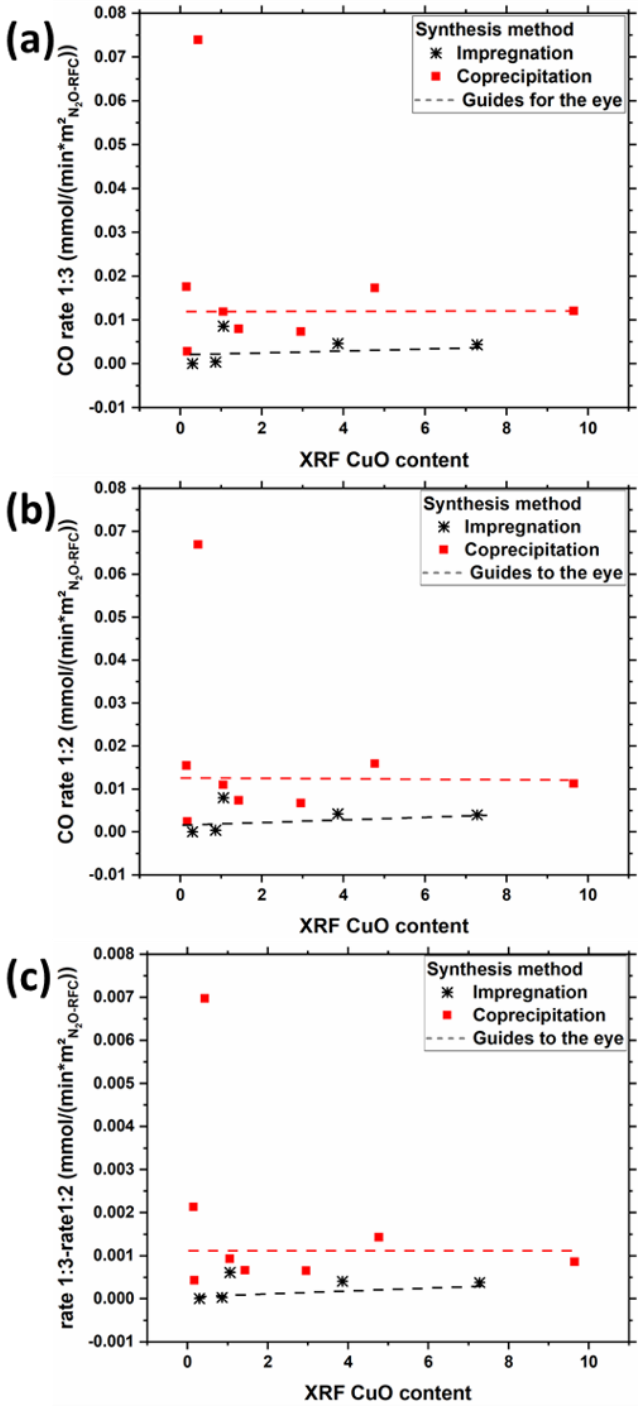

SI 5.33: N_2O-RFC normalised CO rates obtained in the MCPT setup including the outlier (0.44Cu-C).

5.8.11 Photoelectron Spectroscopy

Some samples from the Cu-I series were investigated using photoelectron spectroscopy, with the aim of gaining insight into the oxidation state of Cu species present at the sample surface, and to elucidate the work function of the samples. Prior to photoelectron spectroscopy measurements, the samples were pressed into pellets and reduced by heating to 523 K in 10 % H_2 in Ar at a rate of 2 K/min and keeping at that temperature for

1 h before cooling in the same gas mixture. The samples were then transferred to a glove box without contact to ambient air and mounted onto a sample holder and directly transferred to the spectrometer chamber without air contact.

Ultraviolet Photoelectron Spectroscopy (UPS) was performed by irradiating the sample with photons of 21.22 eV energy (He I emission line) while applying 10.2 eV negative bias used to separate the responses from secondary electrons generated in the spectrometer's detector. The work function was deduced from the UPS spectra by extrapolating the valence band top and the secondary electron cutoff, and the applied bias was subtracted from the excitation energy, providing the work functions.

X-ray photoelectron spectroscopy (XPS) spectra were recorded using non-monochromatised Al Kα (1486.6 eV) excitation and a hemispherical analyser (Phoibos 150, SPECS). The binding energy scale was calibrated using a standard two-point method, using reference samples to measure the Au $4f_{7/2}$ and Cu $2p_{3/2}$ lines, which are known to be located at 84 eV and 932.7 eV, respectively. [*]. No corrections for charging effects were carried out except noted otherwise. As evident from the Zn $2p_{3/2}$ spectra presented in figure SI 5.34 (page 102), 1.06Cu-I was found to charge, which is why its spectra in the following are offset to match the other samples' Zn 2p peaks. The validity of this correction can be gathered from the matching C 1s spectra given in figure SI 5.35 (page 102).

[*]J. F. Moulder, W. F. Strickle, P. E. Sobol and K. D. Bomben, *Handbook of X-ray Photoelectron Spectroscopy*, Perkin-Elmer Corporation, Eden Prairie, 1992.

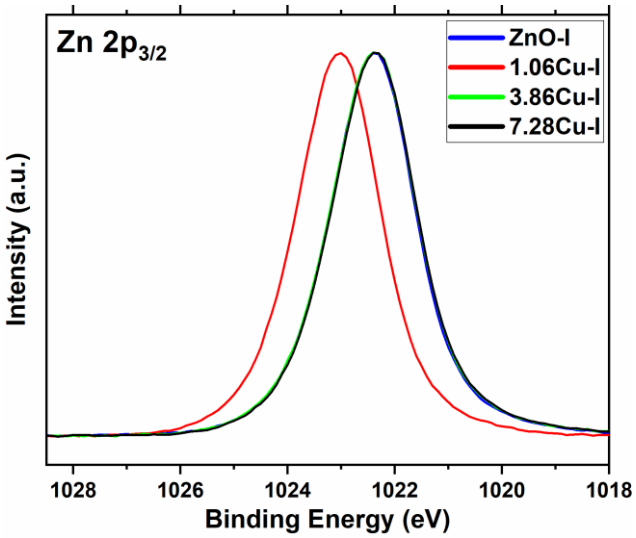

SI 5.34: Zn 2p spectra of some Cu-I series samples.

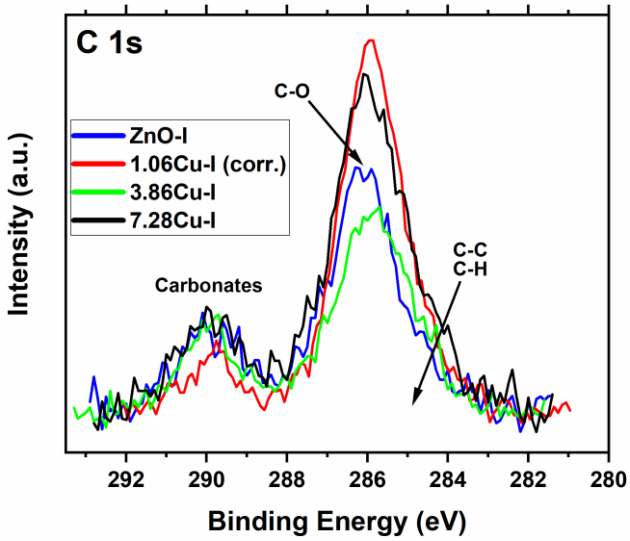

SI 5.35: C 1s XPS spectra of some samples from the Cu-I series

The Cu $2p_{3/2}$ spectra are presented in figure SI 5.36 (page 103), with close-ups to make the ZnO-I spectrum more visible. The main component found in the Cu 2p spectra corresponds to metallic Cu, except for the 1.06Cu-I sample spectrum. This indicates that the CuO present on the surface after impregnation and calcination was successfully reduced. For the 1.06Cu-I sample, the main component appears at a higher binding energy of around 933.7 eV. Cu^{2+}, which might be expected to have such an energy shift, would result in strong satellites[†], but we found no indication for such satellites in our spectra. However, a shift to higher binding energies with decreasing particle size has been found

[†] J. F. Moulder, W. F. Strickle, P. E. Sobol and K. D. Bomben, *Handbook of X-ray Photoelectron Spectroscopy*, Perkin-Elmer Corporation, Eden Prairie, 1992.

for very small Cu particles, which the authors ascribe to final-state effects.[‡] The shift observed for 1.06Cu-I we observe may thus be a result of the lower particle size of the Cu particles in this sample. Furthermore, it has to be noted that the onset of the Cu 2p peaks is at the same binding energy. The peak area of the Cu 2p peak of the 1.06Cu-I sample is within those of the peaks for the samples with higher Cu loading, so it is possible that those samples also have a component at this higher binding energy. Therefore, should a difference in oxidation state or the presence of very small Cu particles be responsible for the observed shift in case of the 1.06Cu-C sample, it is possible that the other samples also contain components in this oxidation state or of this small particle size.

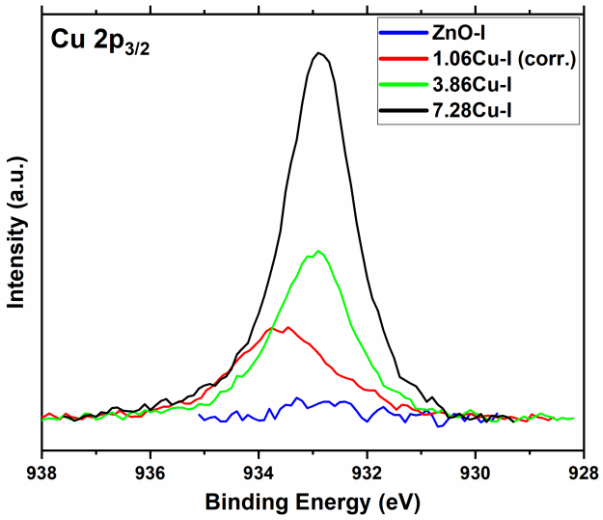

SI 5.36: XPS Cu 2p spectra.

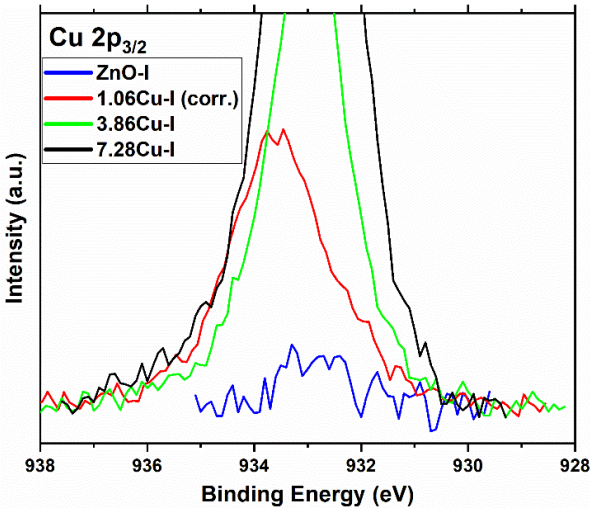

SI 5.37: Close-up of the XPS Cu 2p spectra.

[‡] Y. Wu, E. Garfunkel and T. E. Madey, *J. Vac. Sci. Technol. A*, 1996, **14**, 1662–1667.

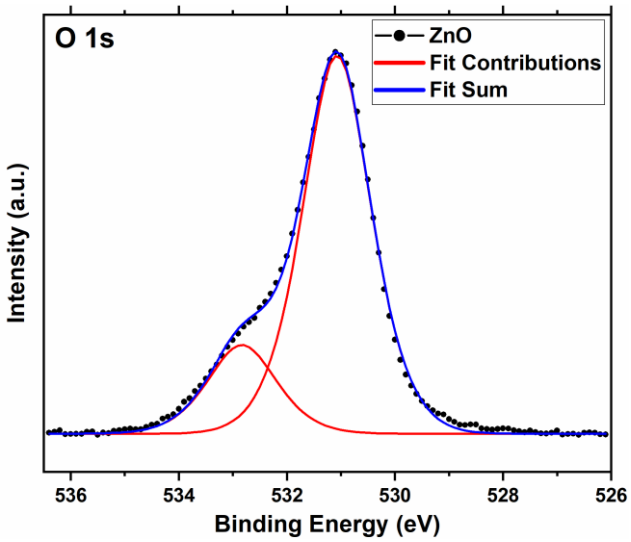

SI 5.38: XPS O1s spectrum of ZnO-I.

The work functions of the investigated samples, given in SI 5.39 (page 104), do not show a direct trend related to the Cu content in the samples.

Sample	**Work function (determined before XPS) [eV]**	**Work function (determined after XPS) [eV]**
ZnO-I	5.31	-
ZnO-I (measured after 3 weeks in glove box)	5.16	-
0.3Cu-I	5.56[a]	5.77
1.06Cu-I	Continuously Charging	5.26
3.86Cu-I	5.33	-
7.28Cu-I	5.1	5.4
[a]the sample charged		

SI 5.39: Work function of the samples determined from UPS spectra.

5.8.12 MCPT

5.8.12.1 Time-on-stream plots of operando MCPT measurements in the rWGS reaction

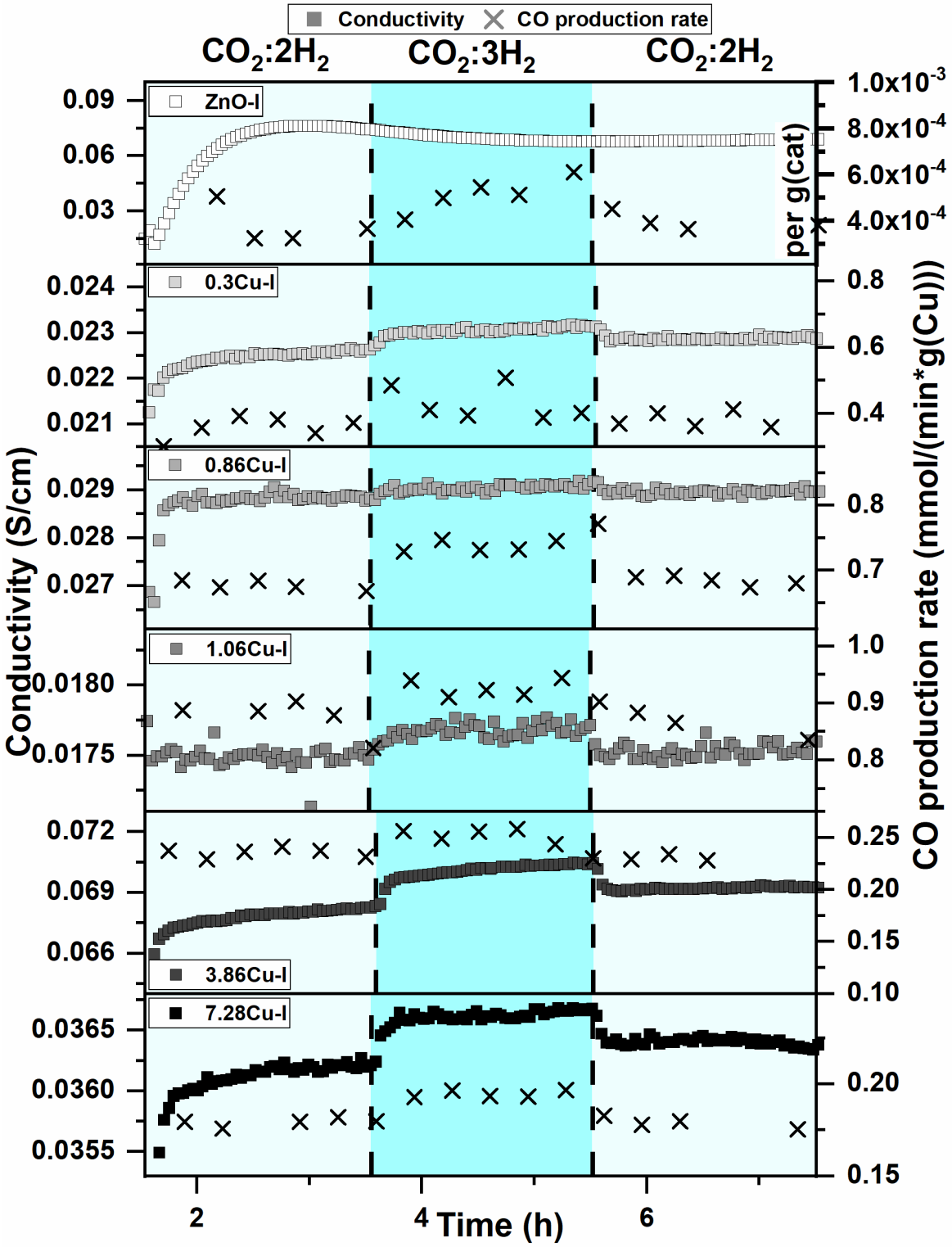

SI 5.40: operando conductivity measurements in rWGS feeds of varying composition of the Cu-I series.

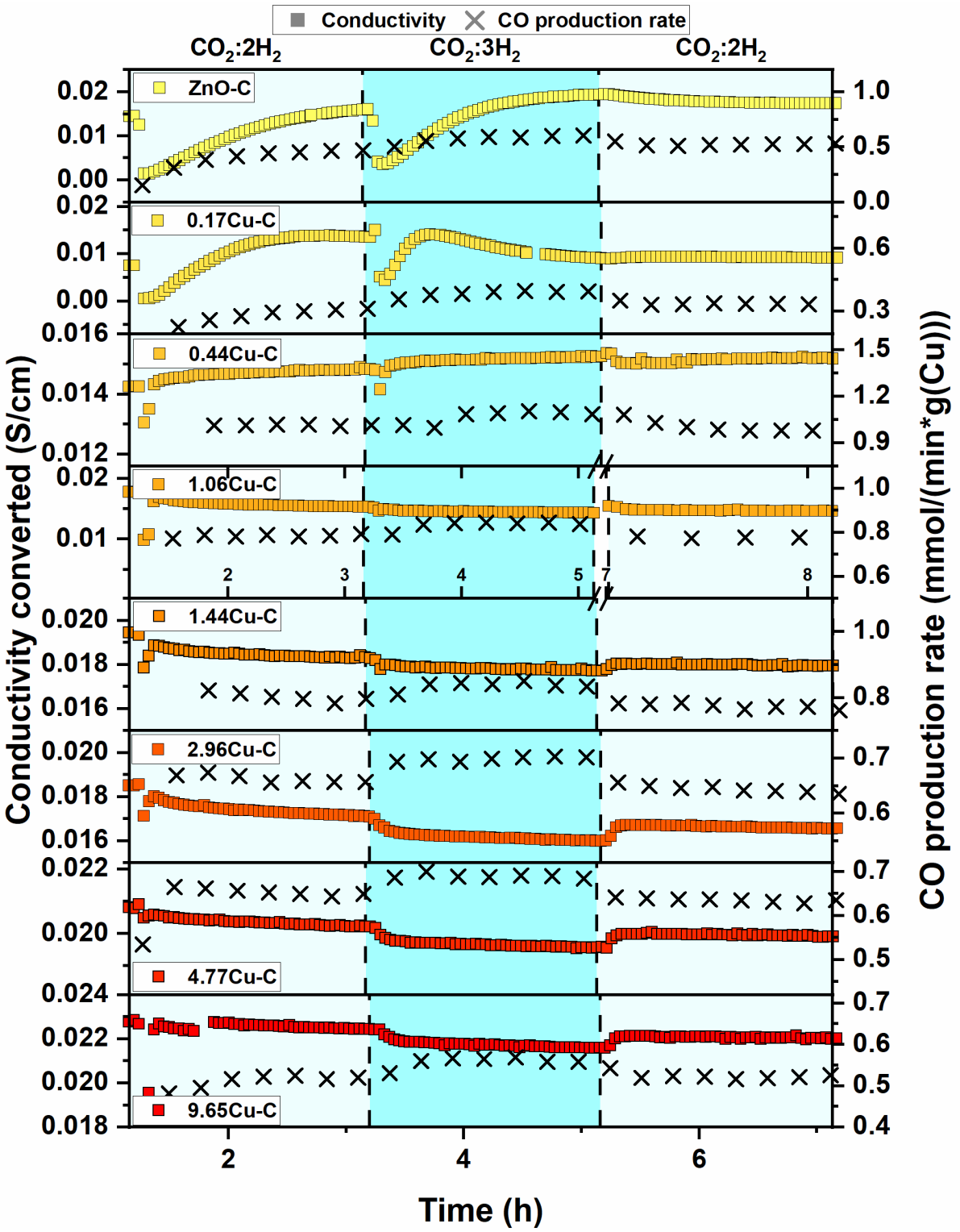

SI 5.41: operando conductivity measurements in rWGS feeds of varying composition of the Cu-C series.

5.8.12.2 MCPT conductivity in reducing and oxidising conditions

The conductivities of the samples were furthermore measured in reducing and oxidising conditions at 503 K. Time-on-stream representations of these measurements are given in figures SI 5.42 and SI 5.43 (page 107-108) for the Cu-I series and Cu-C series, respectively.

In addition, the average conductivity of the last ten measurement points in each gas phase was determined for improved clarity, with results presented in figures SI 5.44 and SI 5.45 (page 109).

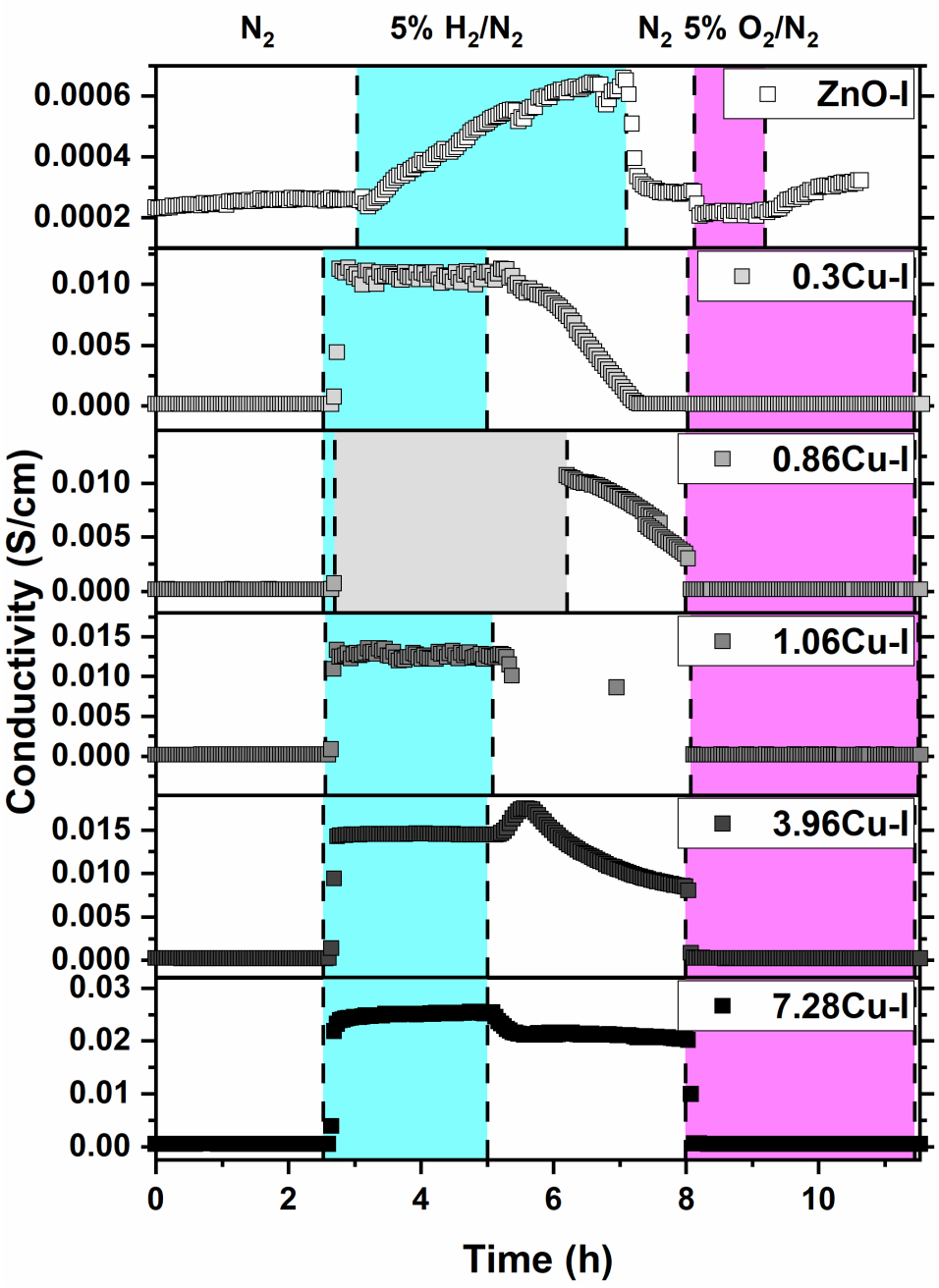

SI 5.42: Time-on-stream graph of the MCPT condutivities of the Cu-I series samples in reducing and oxidising conditions at 503 K.

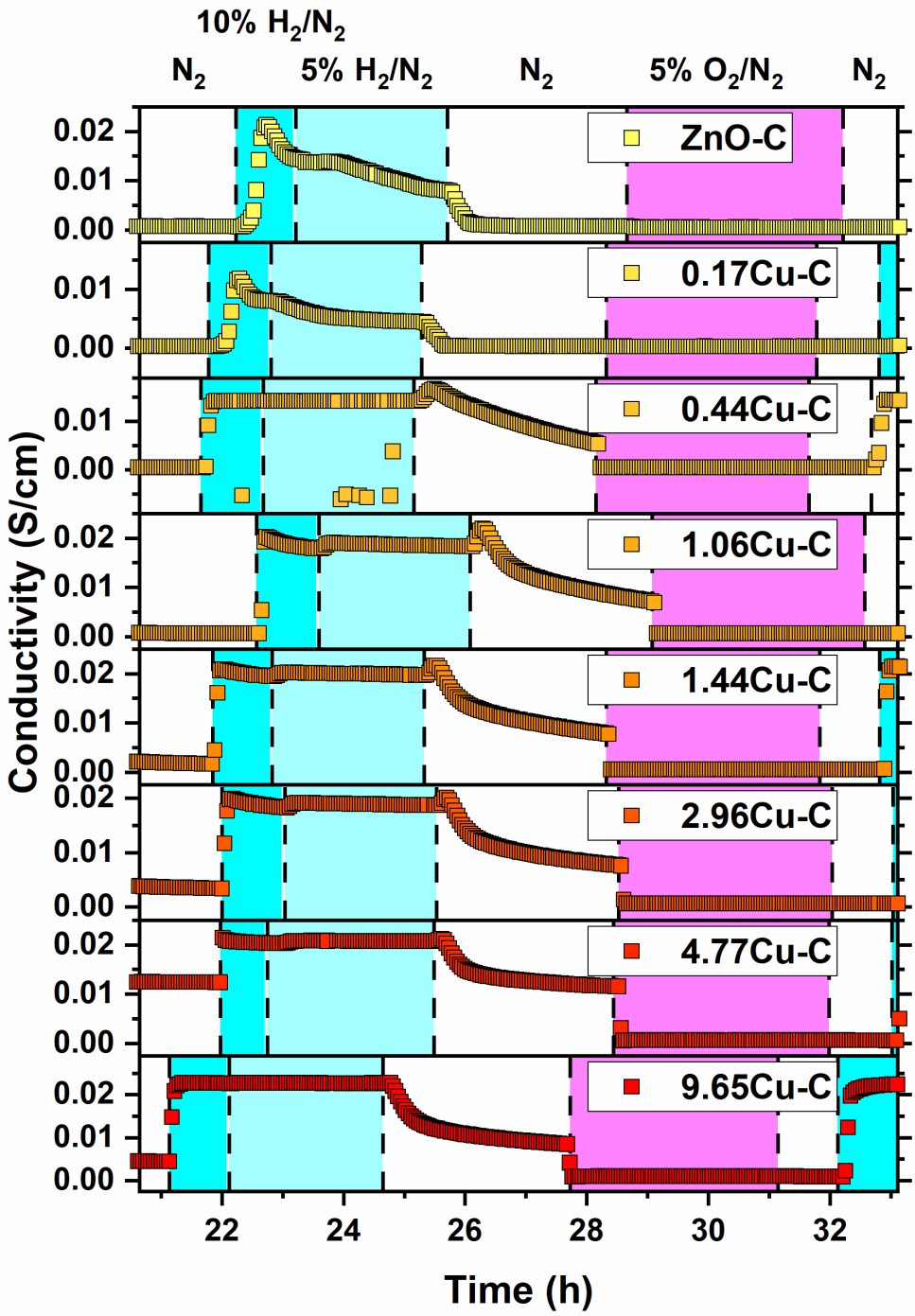

SI 5.43: Time-on-stream graph of the MCPT condutivities of the Cu-C series samples in reducing and oxidising conditions at 503 K.

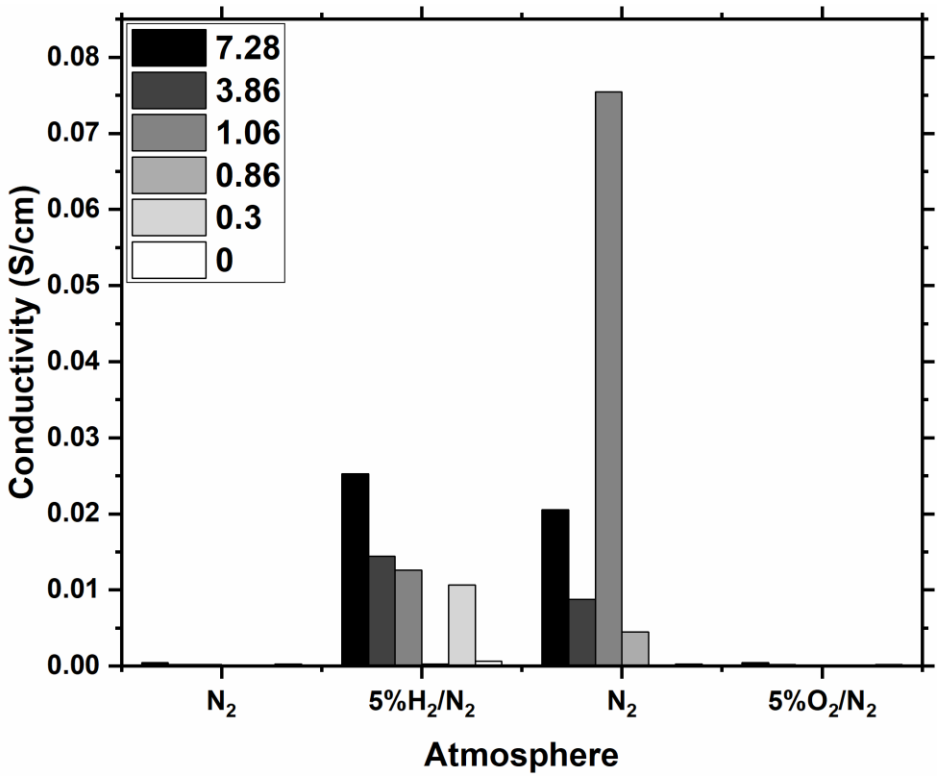

SI 5.44: MCPT conductivities of the Cu-I series samples in reducing and oxidising conditions at 503 K. For each gas feed (the x-axis represents the experimental sequence), the average of the last ten values is represented.)

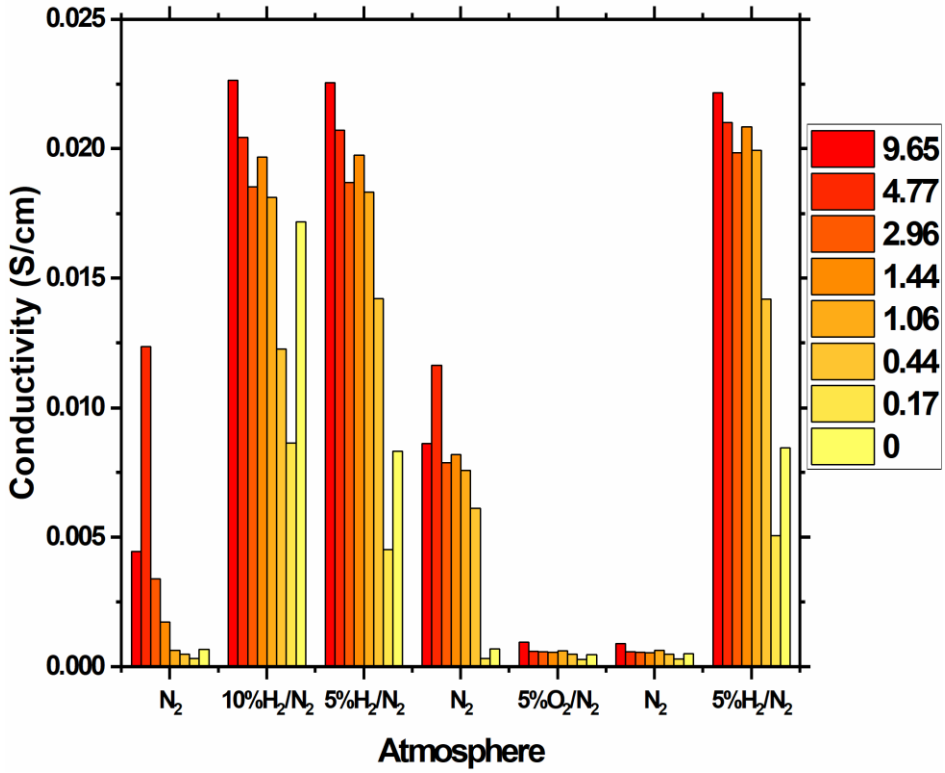

SI 5.45: MCPT conductivities of the Cu-C series samples in reducing and oxidising conditions at 503 K. For each gas feed (the x-axis represents the experimental sequence), the average of the last ten values is represented.)

5.8.12.3 Reproducibility and influence of sample dilution

Since the conductivity showed such drastic qualitative differences between the two sample series, a series of experiments were performed using the two samples with nominal loading of 5 %. (7.28Cu-I and 4.77Cu-C). The results of these experiments are shown in figure SI 5.46 (page 110). To make sure that differences in the setup or long-term drifts in the quality of the cavity, both samples were measured again as they were before (7.28Cu-I undiluted, and 4.77Cu-C diluted 1:1 with SiO_2), producing the same qualitative response as was observed before. To exclude the SiO_2 dilution applied for the measurements of the Cu-C series, the same measurement was again performed with undiluted Cu-C, again leading to the same qualitative response (decreasing conductivity with increasing H_2 content in the feed). Thus, dilution can be excluded as the source for the observed qualitative behaviour. The results of these measurements are presented in figures SI 5.46 and SI 5.48 (page 110-111).

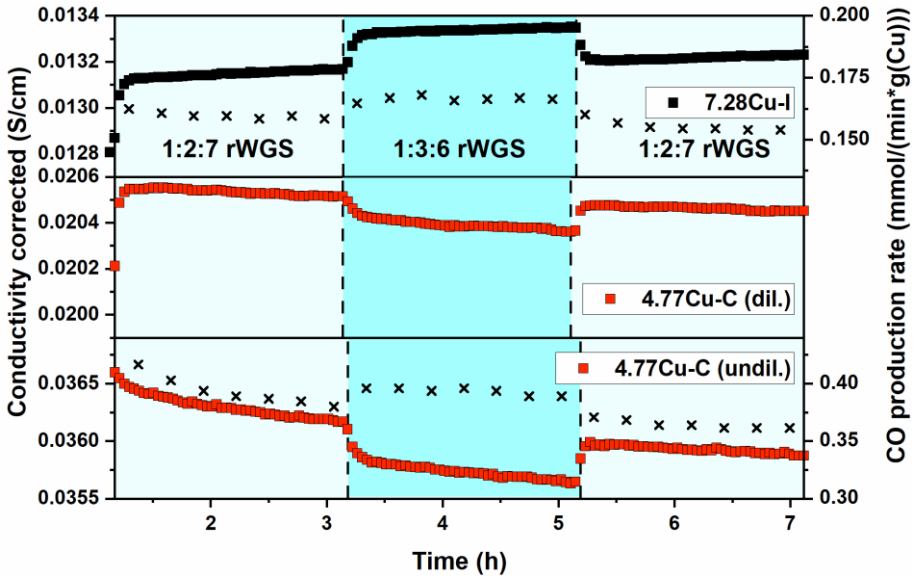

SI 5.46: Comparability of results from Cu-I and Cu-C series, elimination of dilution of Cu-C series samples as a source for changes in qualitative conductivity changes.

It should be noted that while a drift in the MCPT response can be caused by the sample or the sample's response to the applied conditions, an additional contribution can be resulting from a not yet conclusively explained drift caused by the set-up itself. To illustrate this, the Q-values of a MCPT empty measurement in varying gas feeds at 503 K is presented in figure SI 5.47 (page 111). A small drift in the Q factor over time is observed, while (as expected) no response to the changes in gas phase is present.

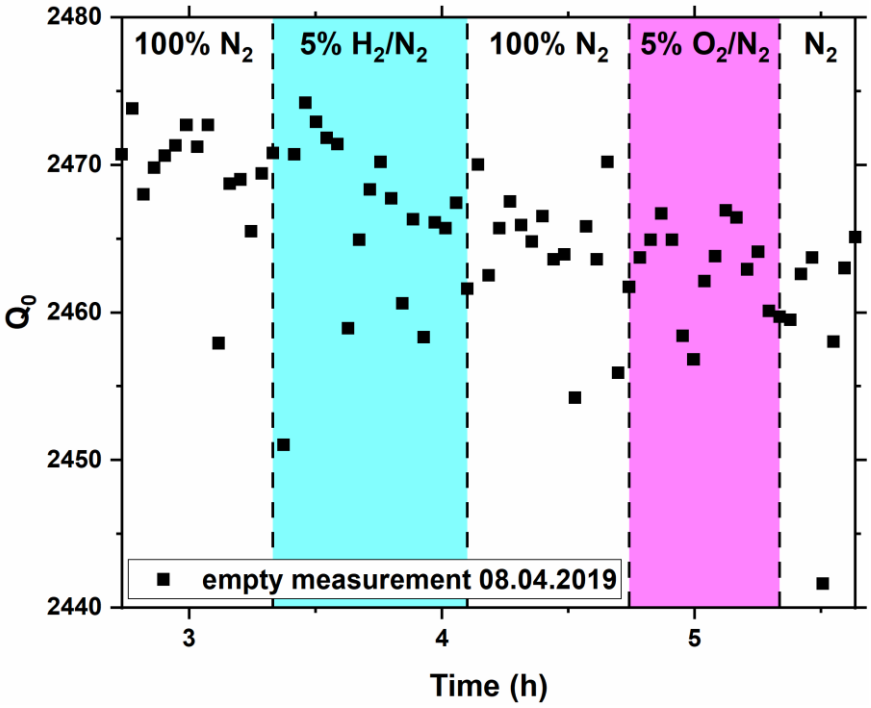

SI 5.47: Q factors of an empty measurement as an example (measurement at 503 K in N_2, 5 % H_2/N_2, and 5 % O_2/N_2, no response of the empty reactor to changes in the applied gas phase is observed).

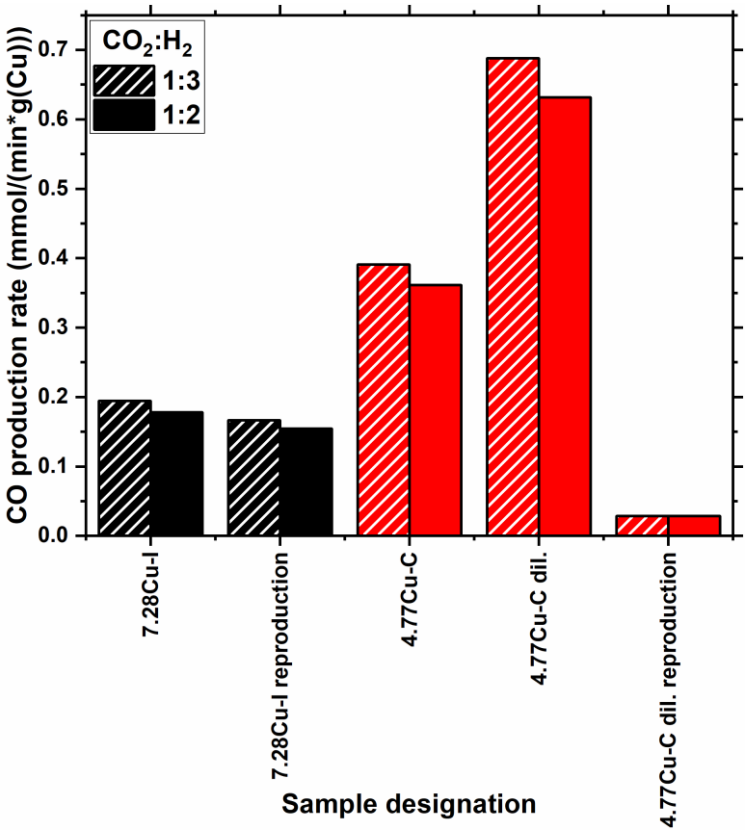

SI 5.48: Comparison of CO production rates of 7.28Cu-I and 4.77Cu-C.

In the reproduction of the measurement of diluted 4.77Cu-C, a problem with the gas chromatograph occurred, which is why the corresponding catalytic data were omitted

from figure SI 5.46 (page 110). As can be seen in figure SI 5.48 (page 111), the values the GC gave for this measurement are much lower than for the other measurements of the comparable sample, and in fact, the obtained CO peaks in the FID trace did not correspond to any CO observed in the TCD trace, as opposed to the case of the other samples, leading to the assumption that the instrument did not perform as desired in case of this measurement.

5.8.12.4 Relationship between conductivity and activity of the investigated samples

To highlight the relationship between catalytic activity and the conductivity of Cu/ZnO samples, these measures are correlated in figure SI 5.49 (page 112). It becomes evident that both sample series (with the exception of the samples with very low Cu loading) form roughly linear trends. Within each gas phase, it is notable that the Cu-C series trend has a much steeper slope than the trend of the Cu-I series, where the absolute value of the conductivity appears to be near independent from the catalytic activity. Furthermore, it can be estimated when samples with a Cu content > 1 % are taken into account in order to avoid the off-trend values for the low loaded samples, that the slopes are nearly identical in both gas feed compositions.

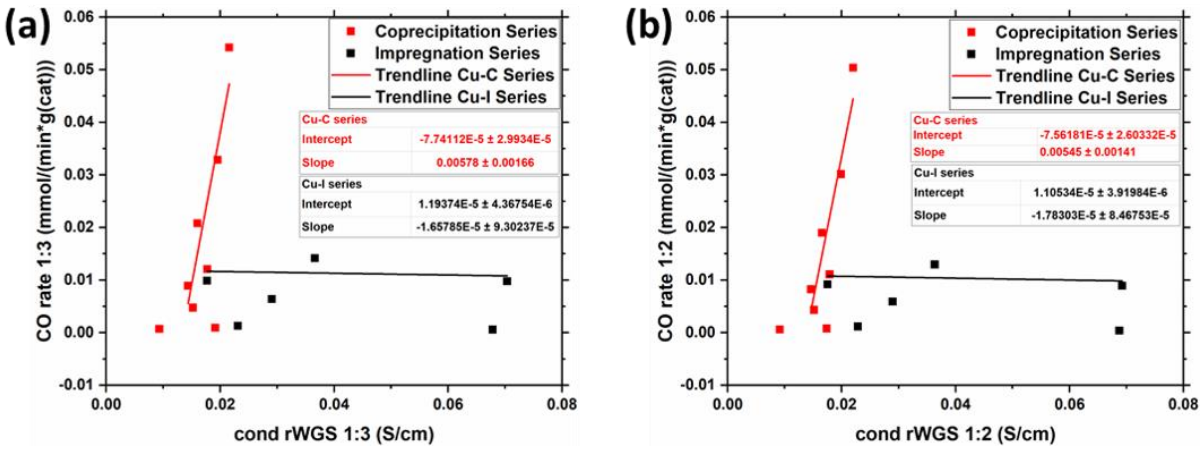

SI 5.49: CO production rates as a function of conductivity in the respective gas feeds: 1:3:6 (a) and 1:2:7 (b).

The above figure illustrates that the changes to the Cu/ZnO system effected by the different synthetic approaches also significantly affect the relationship between the electronic and catalytic properties of the system. However, when considering the data set as a whole, no direct relationship between CO production rate and conductivity was found. Thus, while the qualitative conductivity changes upon changing the reaction feed,

or the steepness of the trends of CO production rate vs. conductivity can differentiate between the two different synthesis methods, it is not possible to decide the productivity of the catalyst from the conductivity alone.

If the activation of CO_2 was the rate-determining step in the rWGS reaction, a higher concentration of charge carriers available for the activation process should be beneficial to the overall reaction rate. In general, an increase in the concentration of charge carriers should lead to an increase in conductivity, if the mobility of the charge carriers is constant. However, what we observe is that the Cu-C series, which has an overall slightly higher CO production rate compared to the Cu-I series, shows a *decrease* in conductivity under conditions that make these samples more productive. Therefore, if the assumption that an increase in conductivity corresponds to an increase in charge carrier concentration for our samples is correct, the activation of CO_2 cannot be the rate determining step of the reaction.

With the data available, it is not possible to determine whether the change in CO production rate or the change in the direction of conductivity change is causal for the other, because the samples are all different (different Cu loading and/or synthesis technique), which influences the chemical nature of the catalyst and its components. However, if the chemical nature of Cu and its interaction with ZnO could be made the same across a whole series of catalysts with varying activity, such an assessment could be possible. However, since the absolute changes in activity are so small, it has to be stressed that a very small change in the properties of the material, e.g., a small change in the Cu lattice parameter, would conceivably be sufficient to change the way the catalyst interacts with the gas phase.

6 Reversible Reduction and Oxidation of Cu Ions Located in a ZnO Lattice

E.H. Wolf, M.-M. Millet, W. Riedel, F. Girgsdies, R. Imlau, O. Timpe, M.G. Willinger, T. Risse, E. Frei, S. Cap, and R. Schlögl

Author contributions: E. H. Wolf designed and oversaw the project and collected the experimental results by writing this paper draft. Furthermore, she carried out and evaluated the MCPT, DR-UV-vis-NIR and low temperature UV-vis experiments. M.-M. Millet synthesised the samples and gave feedback on the paper draft. W. Riedel carried out and evaluated the EPR experiments and gave extensive feedback on the paper draft and project design. F. Girgsdies performed XRD measurements and analysis and aided in writing the related sections. R. Imlau carried out the TEM and electron diffraction as well as helping to write the related sections. O. Timpe carried out the XRF analysis. M.G. Willinger carried out TEM measurements and provided feedback on an early draft of the paper. T. Risse, E. Frei, and S. Cap contributed by discussion and by feedback on the paper draft as well as advice on project design. T. Risse, S. Cap, and R. Schlögl supervised the project and gave feedback on the experimental design.

Reversible Reduction and Oxidation of Cu Ions Located in a ZnO Lattice

6.1 Abstract

The Cu/ZnO system is known for its efficiency in reducing CO_2 which is a key reaction in efforts to decrease the amount of greenhouse gases and for the production of alternative fuel. To optimise the system´s catalytic performance it is central to improve the fundamental understanding of this catalyst. The reversible reduction and oxidation of Cu ions in a zinc oxide lattice was investigated using in situ and inert transfer experimental techniques. To focus on the modification of ZnO by Cu ions rather than the effects of metallic Cu particles, we studied a sample containing an amount of Cu below the solubility limit in ZnO. Using the *in situ* microwave cavity perturbation technique (MCPT) it was possible to detect a reversible reduction and oxidation process by contactless measurements of the samples conductivity. Powder X-ray diffraction and electron diffraction in transmission electron microscopy were unable to confirm the presence or absence of Cu ions in the ZnO lattice due to the low amount of Cu present in our sample. However, Electron Paramagnetic Resonance (EPR) confirmed the presence of isolated Cu^{2+} ions in the sample, the amount of which was greatly reduced upon reduction. A slow change in EPR signal was observed after reducing and vacuum sealing the sample. Our findings highlight the dynamic nature of the Cu/ZnO system, which is of importance for the understanding and improvement of the system in catalytic applications. The effects discussed may also be relevant for the understanding of the results presented in chapter 5. *In situ* and inert transfer methods are shown to be essential for the detection of small changes to the air sensitive samples, especially those occurring on short timescales.

6.2 Introduction

The Cu/ZnO system is known for its high performance in the catalytic reduction of CO_2, for example, the reverse water gas shift reaction or the methanol synthesis reaction. In this system, the role of the support is not only the stabilisation of Cu against sintering, preserving the catalyst's activity.[1] Instead, ZnO is commonly considered as a reservoir for

dissociated hydrogen generated on Cu, which can then be released during the hydrogenation step.[2] There exists a strong metal-support interaction (SMSI), hypothesised to be responsible for the catalytic activity, which is higher than the one of either of the components alone.[3] This SMSI, which is responsible for the performance of this catalytic system, requires the close contact of Cu and ZnO. To be able to improve on the catalytic performance of the system, it is key to better understand the interplay between the components and their dynamic behaviour.

Different characteristics of the Cu-ZnO interaction have been previously proposed in literature, highlighting the close contact between these two components. Cu atoms in Cu/ZnO samples were found to be mobile,[4] with a reversible migration and reduction and oxidation of Cu atoms depending on the redox potential of the applied gas phase.[5,4] There is no clear consensus about the oxidation state of Cu in the active catalyst, apart from metallic Cu^0, Cu^+ and intermediate oxidation states have been proposed.[6–9] Furthermore, the Cu-ZnO interface has been highlighted as important for the activity of the catalyst.[2,10] The nature of this interaction is the focus of the current investigation.

While the industrial catalyst has a high Cu/Zn ratio (> 50 mol% Cu),[11] it is nevertheless useful to study systems with a much lower Cu content in order to focus on the Cu-Zn interaction, since the underlying processes are likely general to samples containing Cu and ZnO. In this investigation, a sample with a Cu content below the solubility limit of Cu^{2+} ions in ZnO (2 at.%)[12] was used. With a loading of 1.06 wt.% Cu, the sample has the possibility of containing Cu^{2+} ions in ZnO, but has sufficient Cu content to analyse its nature with different analytic techniques. Since the Cu content is low enough to limit the formation of particles, it is possible to isolate the dissolution of Cu in ZnO from the effects induced by metallic Cu particles.

The intermixing behaviour of Cu with the ZnO support has been extensively studied and observed using many experimental techniques, e.g., high-resolution electron microscopy,[5] X-ray diffraction,[5,13] *in situ* electron energy loss spectroscopy (EELS),[4] extended X-ray absorption fine structure measurements (EXAFS),[13] UV-vis-NIR-spectroscopy,[9] FTIR,[14] and surface area determination techniques such as temperature programmed desorption (TPD) or N_2O-reactive frontal chromatography (N_2O-RFC)[2]. This research reveals that the state of Cu in the system critically depends on the experimental

conditions, making *in situ* experimental techniques especially valuable. Furthermore, such techniques allow the study of dynamic processes that cannot be revealed by offline experimental methods.

In this contribution, we follow the reduction and oxidation of the CuO/ZnO sample by the means of a combination of inert transfer and *in situ* techniques.

6.3 Experimental

6.3.1 Materials

Materials used for the synthesis were $Zn(NO_3)_2 \cdot 6H_2O$ (ACROS, 98 %), HNO_3 (ROTH, ≥ 65 %), Na_2CO_3 (ROTH, ≥ 99.5 %), $Cu(NO)_3)_2 \cdot 3H_2O$ (ACROS, 99 %), NaOH (Merck, ≥ 97 %), citric acid (Alfa Aesar, 99 + %), NH_3 (VWR, 25 % in water). Deionised water was taken from a Milli-Q system (Merck). For X-ray fluorescence analysis, $Li_2B_4O_7$ (Fluxana, >99.98 %) and an additive containing LiBr (Fluxana) Gases (Westfalen) were of purity 5.0 (99.999 %), and additionally treated with moisture and O_2 filters (Agilent, < 0.1 ppm water and < 50 ppb O_2 at 1-10 L/min operating flow).

6.3.2 Synthetic procedure

6.3.2.1 Synthesis of ZnO

Zinc oxide was prepared by precipitation from an aqueous nitrate solution. 357.00 g $Zn(NO_3)_2 \cdot 6H_2O$ were dissolved in 500 mL Milli-Q water. 15 mL 65 % nitric acid were added, before filling up to 600 mL. 339.16 g Na_2CO_3 were dissolved in deionised water to make 2 L solution. 400 mL deionised water were added to a Labmax (Mettler-Toledo) automated laboratory reactor, before the addition of the nitrate solution at a rate of 20 g/min for 30 min while keeping the pH constant at 6.5 by adding the appropriate amount of carbonate solution. The ageing time for the mixture was 60 min. Consecutively, the product (zinc hydroxycarbonate) was filtered and washed until the filtrate had a conductivity lower than 0.5 mS/cm. After drying at 373 K for 10 h in an oven, the powder was calcined to ZnO in static air in a muffle oven at 603 K (ramp rate 2 K/min, dwell time 180 min).

6.3.2.2 Synthesis of Cu citrate

48.96 g $Cu(NO_3)_2 \cdot 3H_2O$ were dissolved in 400 mL deionised water. In further 400 mL deionised water, 16.20 g NaOH were dissolved, before slowly adding to the nitrate solution under ice-cooling. $Cu(OH)_2$ formed as a blue residue. The powder was filtered and washed until the filtrate conductivity was lower than 0.5 mS/cm. The hydroxide was then suspended in 400 mL deionised water. A solution of 16.58 g citric acid in 100 mL water was then added slowly, before leaving to stand at room temperature for 4 days. During this time, a greenish precipitate formed on the beaker walls, which was removed from the walls using an ultrasonic bath, filtered, and dried. Thermogravimetry (NETZSCH Jupiter) was employed to determine the quantity of citrate needed for the following impregnation step. The mass remaining as CuO after complete oxidation was 33.41 % of the original test weight.

6.3.2.3 Synthesis of CuO/ZnO

945.19 mg of Cu citrate were dissolved in 10 mL 12.5 % ammonia solution (formed by diluting 25 % ammonia in water with additional deionised water). The resulting citrate solution was diluted in the ratio 1:4 (2 mL solution filled to 10 mL) in order to give the appropriate concentration for impregnation. 6 g of ZnO were impregnated with 3 mL of this solution. After air drying at room temperature, the powder was further dried in a muffle oven in static air by heating to 393 K using a ramp rate of 2 K/min and holding this temperature for 10 h. Subsequently, the sample was calcined at 603 K for 3 h (ramp rate 2 K/min) in a muffle furnace in static air, to yield CuO/ZnO.

6.3.3 Characterisation

6.3.3.1 X-ray fluorescence analysis (XRF)

The loading of CuO on ZnO was determined using X-ray fluorescence analysis (XRF) using a Bruker S4 Pioneer X-ray spectrometer. For this, 98.7 mg sample were fused with 8.9 g lithium tetraborate and about 100 mg of an additive containing lithium bromide to form a glass melt disc of 40 mm diameter. The Cu $K\alpha_1$ and Zn $K\alpha_1$ lines were used for the determination of the Cu and Zn content respectively.

6.3.3.2 Powder X-ray diffraction (XRD)

To evaluate the sample in its reduced state, powder XRD under inert conditions was applied. For this, the sample was first reduced by heating to 523 K at a rate of 2 K/min and holding for 1 h, all in an atmosphere of 10 % H_2/Ar (total flow 40 mL/min). The sample was then inertly transferred into a glove box (Ar filled, O_2 level < 1 ppm), where it was filled into an airtight sample holder. The residence time in the glove box lasted several hours after removal from the reduction tube. Finally, the sealed sample holder was transferred to the X-ray diffractometer. The XRD measurement was performed in Bragg-Brentano geometry on a Bruker AXS D8 Advance II theta/theta diffractometer using Ni filtered $Cu_{\alpha 1+2}$ radiation and a position sensitive energy dispersive LynxEye silicon strip detector. The resulting X-ray diffractogram was analysed by whole powder pattern fitting according to the Rietveld method as implemented in the TOPAS software (version 5, Bruker AXS).

6.3.3.3 Electron paramagnetic resonance (EPR)

Prior to EPR measurement, the sample was reduced in a quartz tube (2.9 mm outer diameter) attached to a flange connector, with which it was connected to a gas dosing system and vacuum pump. The tube was evacuated and flushed with 100 % H_2 several times and heated until the desired colour change of the sample concurrent with reduction (beige to dark grey) had occurred at a furnace temperature of 573 K. The sample was sealed in vacuum by melting off the quartz tube from the flange.

For comparison, the non-reduced CuO/ZnO sample was also measured in an open quartz tube. Both the reduced and non-reduced sample were heated to 500 K in air for 1 h after initial EPR measurements to investigate the reversibility of the reduction process.

Continuous wave (CW) EPR spectra at X-band frequencies (9.86 GHz) were obtained at room temperature using a Bruker B-ER420 spectrometer upgraded with a Bruker ECS 041XG microwave bridge and a lock-in amplifier (Bruker ER023M). The samples were measured in a Bruker SHQ resonator applying a modulation amplitude of 5 or 10 G. All spectra were background corrected by subtracting the spectrum of an empty quartz tube.

6.3.3.4 (Inert transfer) transmission electron microscopy (TEM)

Prior to TEM investigations, the sample was reduced by heating to 523 K using a rate of 2 K/min, and holding at this temperature for 1 h, all in an atmosphere of 10 % H_2/Ar (total flow 40 mL/min). After reduction, the sample was prepared on Au grids with lacy carbon support films and transferred inertly to the respective microscope via a glove box using a vacuum transfer holder. For TEM measurements, a Thermo Scientific Talos F200X S/TEM, operated at 200 kV acceleration voltage, was used. The microscope is equipped with a HAADF detector for STEM measurements, the energy dispersive X-ray spectroscopy (EDX) maps were recorded using ChemiSTEM Super-X detectors, and diffraction patterns using a Thermo Scientific Ceta camera.

6.3.3.5 Diffuse reflectance UV-vis-NIR spectroscopy

DR-UV-vis-NIR spectroscopy was carried out in an Agilent Cary 5000 photospectrometer equipped with a Harrick Praying Mantis Diffuse Reflection Accessory and Reaction Chamber. The sample was heated up to 503 K in inert atmosphere (flow of 50 mL/min He) before the gas feed was switched to 10 % H_2/He, back to He, and then to 10 % O_2/He. This procedure was repeated after heating up to 523 K, again in inert atmosphere. The spectrum of the sample was recorded against a background determined using Spectralon as a white standard at room temperature and in ambient air.

6.3.3.6 Microwave cavity perturbation technique (MCPT)

We measured the response of the CuO/ZnO sample in reducing and oxidising conditions using the contact-free and *in situ* Microwave Cavity Perturbation Technique. Previous reports detail the experimental setup and measurement technique.[15] Our setup allows for the simultaneous application of reactive and inert gases at the same time as the conductivity is measured.

48.4 mg of sample (sieve fraction 100-200 µm) were placed in a 3 mm inner diameter quartz glass reactor and fixed between two quartz wool plugs. The length of the sample bed was 10 mm. A constant flow of 1 mL/min at a pressure of 1300 mbar was applied, mixed from reactive and inert gases. The cavity was flushed with 15 mL/min N_2 gas in order to prevent the formation of moisture droplets, since the cavity was cooled to 293 K throughout the experiment. In order to heat the sample, a stream of 8 L/min N_2 was pre-

heated and flown through a dewar system around the reactor tube, thus heating the sample while at the same time insulating the cavity from heat by the dewar's vacuum.[15] The measurement range was 3.18 to 3.30 GHz, over which 20001 measurement points were taken using a bandwidth of 500 Hz. Three measurements were averaged to give one data point to increase the data quality. The resulting data were fit using an algorithm implemented in MATLAB by Kaijfez.[16] The resulting quality factor and resonance frequency for experiments with and without sample were used to calculate the permittivity and in turn the conductivity of the sample at each data point, as detailed elsewhere.[15] The values were corrected to account for the filling fraction of the powder sample using a formalism established in literature.[17,18]

For the redox experiment, the sample was heated under 100 % N_2 flow to 503 K at a rate of 5 K/min, before alternating feeds containing 5 % H_2 in N_2, and 5 % O_2 in N_2 were applied, separated by pure N_2 feeds.

6.4 Results

X-ray fluorescence analysis (XRF) was used to determine the elemental composition of the as-synthesised powder after the calcination step. The concentration of CuO was found to be 1.06±0.03 wt.%. This corresponds to a loading of 1.11 at.% CuO on ZnO which is thus, as intended, well below the solubility limit of Cu in ZnO.

In order to investigate the sample in reducing and oxidising conditions, we employed a combination of *in situ* and inert transfer experimental techniques. The sample is not stable in air in its reduced state, which is why such methods are required to gain insight into the system under different experimental conditions. Temperatures in the range of 503 – 533 K were chosen such that the reduction of Cu was possible, while at the same time avoiding the reduction of ZnO to Zn.

The conductivity of the sample under reducing and oxidising conditions was measured using MCPT. This method is sensitive to small changes in the electronic structure of the material under test, and can thus give insight into the processes as well as their reversibility in case the sample is subject to multiple reduction and oxidation steps. The temporal dependence of the conductivity during redox cycling of the sample is presented in Figure 6.1. The reducing phases are indicated with a blue background, and the oxidising

phases are marked red. A white background corresponds to an inert gas feed (pure N_2), which was applied in between the two reactive gas atmospheres. For comparison, the inset in Figure 6.1 shows the corresponding experiment for pure ZnO on the same conductivity scale, highlighting that the large responses observed for the CuO/ZnO sample are not inherent to the ZnO support only.

As the gas feed is changed to reducing conditions, the conductivity increases first sharply, followed by a slow increase, which extends to the end of this period. This temporal response directly shows that clearly more than one process contributes to the conductivity increase in Cu/ZnO under reducing conditions. When switching to the inert gas feed a slow decrease in conductivity is observed. Exposing the sample to an oxidising feed results in an immediate reduction of the conductivity back to the initially measured value. This change is immediate upon changing the gas atmosphere, and there is no subsequent slow change in the conductivity. Furthermore, the conductivity of the oxidised sample does not change after switching to the inert gas feed. Both of these observations are in contrast to the response upon admission of reducing gas atmosphere. The conductivity increase in reducing and the decrease in oxidising conditions is consistent with a n-type conduction in our sample. When the reduction process is repeated, the experiment shows good reproducibility, indicating the good reversibility of the redox process.

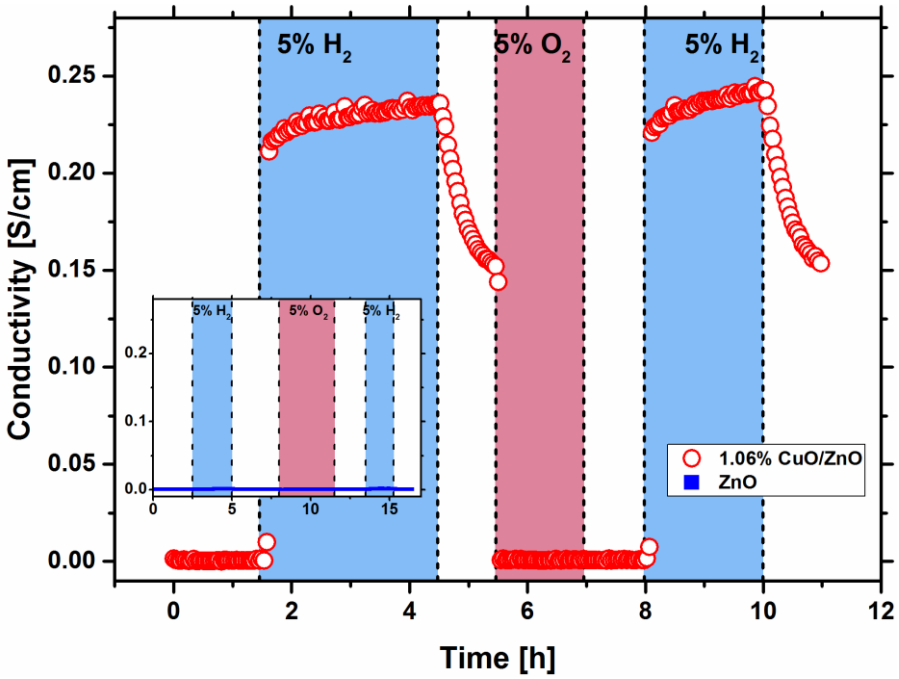

Figure 6.1: ***In situ*** **MCPT conductivity measurement at 503 K in reducing conditions (blue) oxidising conditions (red) and inert gas (white) for 1.06 wt.% CuO/ZnO (red open circles) and, for reference, ZnO (blue filled squares, in the inset plot).**

The *in situ* MCPT measurements clearly demonstrate the involvement of several processes occurring on different time scales. ZnO is known to exhibit H_2 gas sensing properties due to adsorption of dissociated hydrogen, which is expected to be a rapid process resulting in a change in conductivity. However, the gas sensing capabilities of ZnO would then have to be drastically changed by the addition of Cu, since the conductivity change of unmodified ZnO subjected to the same reductive treatment is not of the same order of magnitude (see the inset in Figure 6.1). Since the concentration of Cu in our sample is below the solubility limit of Cu in ZnO, Cu^{2+} ions are expected to largely reside as dopants at the surface or in the lattice of ZnO. The reduction of these Cu^{2+} species to Cu^{+} or Cu^{0} should occur on a fast time scale, especially for easily accessible Cu species near the ZnO surface.

To investigate the presence of such Cu^{2+} ions in the as-synthesised sample we performed low-temperature UV-vis-NIR spectroscopy. Stirling and Stone[19] attribute a broad absorption band around 1500 nm splitting into two contributions at liquid nitrogen temperature to the presence of Cu^{2+} in solid solution with ZnO. In contrast to their findings, we do not observe such a signal for our sample as synthesised or after reduction.

Spectra associated with this experiment can be found in the supporting information (figure S 6.4, page 140).

Upon reduction, however, a colour change of the sample is observed. To investigate this in more detail, diffuse reflectance UV-vis spectroscopy was employed. Since an impregnation method was applied, it may be speculated that the Cu concentration is highest close to the surface of the ZnO support, possibly leading to the formation of Cu-enriched particles, which may be reduced by H_2 to metallic Cu, resulting in an increased conductivity of the sample. Such metallic nanoparticles of small size (≤ 30 nm) exhibit characteristic plasmon bands, in the case of Cu in the region of 590-600 nm.[20–22] We did not observe an appearance of such a band when a reducing atmosphere (10 % H_2/He) was applied at 503 K. Therefore, the UV-vis data do not provide a conclusive proof of the presence of metallic Cu under reducing conditions. However, upon application of these reducing conditions and when switching back to inert conditions the intensity of the spectra in the visible region changed significantly, which is in line with the observed change of colour upon reduction. The reduced sample was significantly less reflective, which is in line with an increased electron density in the sample in the reduced state as compared to the as synthesised or oxidised sample. The relevant spectra as well as comparison of the intensity changes at different points throughout the visible region are presented in the supporting information (figures S 6.2 and S 6.3, page 139-140). It should be noted that we do not observe a clear absorption edge corresponding to Cu_2O nor to CuO in our spectra of the as synthesised sample (figure S 6.1, page 139).

To further investigate the speciation of Cu in the reduced state, X-ray diffraction was measured under inert conditions after reduction and inert transfer via a glove box. It was endeavoured to find evidence for the presence of metallic Cu or of Cu as a dopant in the ZnO lattice. The diffraction pattern of the sample shows clear peaks of ZnO crystallising in the wurtzite structure. The low Cu loading and probably small domain size (strong peak broadening) make the detection of potential Cu metal peaks challenging. Thus, the diffraction data were subjected to whole powder pattern fitting to enhance the detection limit. The Cu 111 reflection would appear around 43° 2θ, between the ZnO 101 and 102 reflections. It turned out that the diffraction profiles of ZnO showed a pronounced anisotropic (*hkl* dependent) peak broadening. The proper modelling of these profiles is

essential, as a misfit of the extending ZnO reflection "feet" could mask the presence of a low and broad Cu 111 peak. The best approximation of the ZnO profiles was obtained using an anisotropic extension of the Double-Voigt profile shape[23], in which the Lorentzian component of the size broadening was replaced with an 8th order spherical harmonics function. The ZnO lattice parameters (*a*, *c*) and the refined oxygen *z* coordinate of the first fit were evaluated for signs of possible Cu doping in the ZnO lattice. The values were compared to those for pure ZnO and ZnO doped with various metal ions (Al, Ga, Mg) reported previously.[24] None of the parameters (*a*, *c*, or *z*(O)) exhibits significant changes. However, the effect of Cu on the ZnO lattice is expected to be overall small due to the similarity of the ionic radii of Zn^{2+} and Cu^{2+}.

In order to decide whether or not a low, broad Cu 111 reflection is present, two fit models were used, with and without a Cu metal phase, respectively. Figure 6.2 (a) presents the result assuming a pure ZnO phase, while Figure 6.2 (b) shows the fit including an additional metallic Cu phase. Both options lead to equally good fits, and thus, XRD provides no indication for the presence of crystalline metallic Cu in this sample.

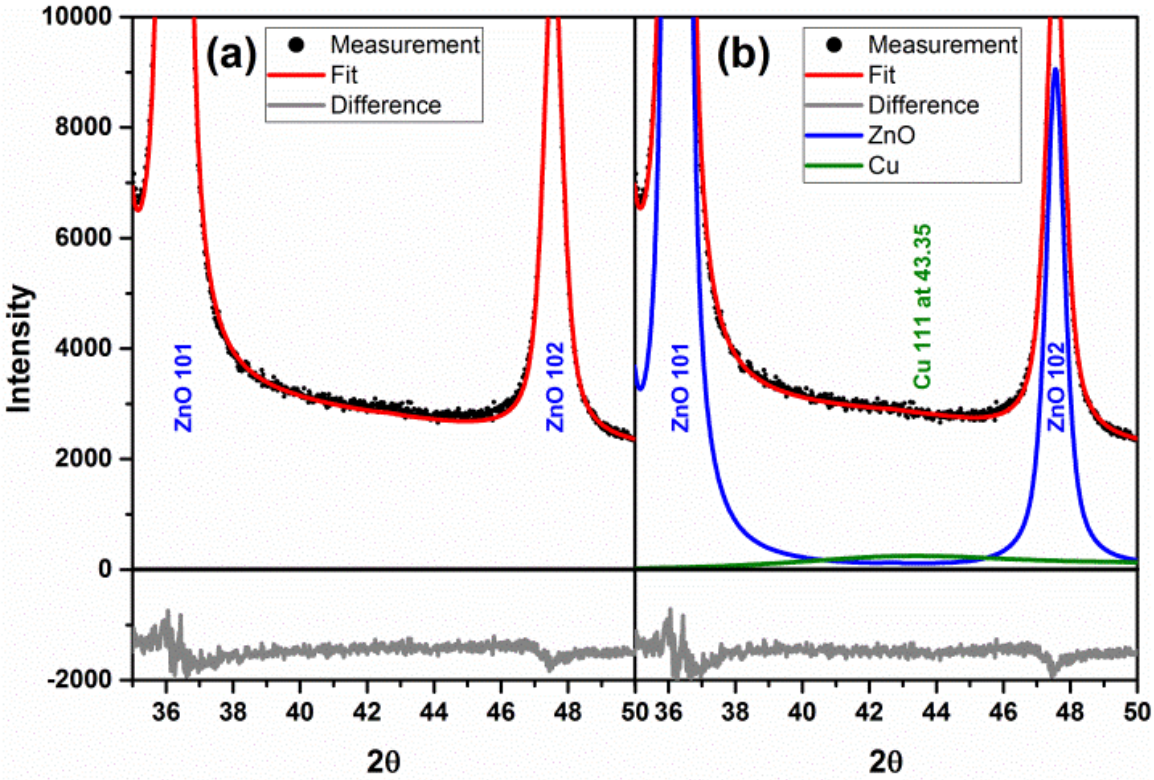

Figure 6.2: Powder XRD measurement data and fits (a) assuming ZnO as the only crystalline phase (b) assuming the presence of crystalline Cu metal in addition to ZnO – enlarged to the relevant area (full fit shown in S 6.5).

Since XRD, an integral analysis method, was unable to provide additional information on the nature and location of Cu species in out samples, a detailed analysis of the structure and morphology of the sample and the location of Cu in the sample was performed using inert transfer transmission electron microscopy (TEM) and energy dispersive x-ray spectroscopy (EDX). These methods facilitate a more local investigation of the sample, even if the Cu species are so small that they would be undetectable by XRD due to line broadening.

For these measurements, the sample was reduced and transferred inertly to the microscope via a glove box using a vacuum transfer holder. The residence time in the glove box of the sample after reduction was 1-2 h. Overview TEM imaging revealed two different morphologies of particles to be present in the reduced sample: Needle-shaped and platelet-shaped particles of various sizes. The length of the needles typically exceeds the diameter of the platelets. Some overview images are given in figure S 6.8 (page 142). This anisotropy can also lead to the peak broadening observed in X-ray diffraction. Analysing a number of overview TEM images (low magnification of ca. 8600x) it was investigated whether the addition of Cu citrate and subsequent heat treatment of the sample impacted the morphology of the sample support by preferential deposition and subsequent growth on certain (polar or non-polar) facets of ZnO. In these images (examples can be found in S 6.7 and S 6.8, page 142), the numbers of needle-like and platelet-like structures were counted. The pure support was previously calcined again in order to exclude the effects of the second calcination step, and this sample was then compared to unreduced CuO/ZnO. For the pure ZnO support, a total of 5 needle-like areas were found and 32 platelet-like areas (ratio = 0.16), and for CuO/ZnO, 7 needle-like and 44 platelet-like areas (ratio = 0.16 likewise). Thus, no clear indication of a difference in morphology was observed between ZnO and CuO/ZnO.

Selected area electron diffraction was used to elucidate phases present in a typical agglomerate of particles, consisting of both needles and platelets. The selected area which forms the basis of the investigation and the resulting diffraction pattern are presented in the supporting information (figure S 6.6, page 141), and the calculated ring integral is presented alongside references for Cu[25] and ZnO[26] in Figure 6.3. As observed, no

conclusions about the presence of Cu-containing nanoparticles were possible. However, the diffraction pattern revealed the presence of ZnO in the sample.

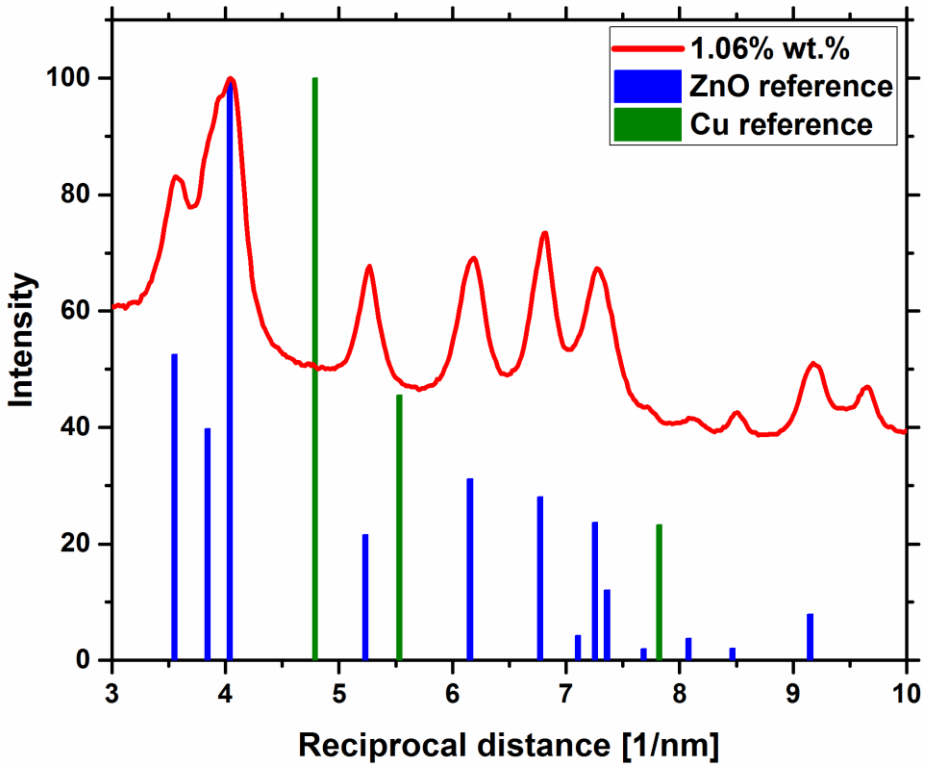

Figure 6.3: Ring integrals of selected area diffraction patterns of sample with 1.06 wt.% Cu (red) and references for ZnO[26] (blue) and Cu[25] (green)

Energy-dispersive X-ray spectroscopy (EDX) was performed in order to determine the distribution of Cu within the sample. The mapping (Figure 6.4) shows the presence of small Cu-enriched agglomerates of about 5 nm in size, underlined by the line scan in Figure 6.4 (d) The location of the linescan is marked in the Cu map (Figure 6.4 (c)). The count statistics (15±3 counts for the Cu-rich region) allow to evidence the presence of these Cu enriched clusters. The green line in Figure 6.4 (d) shows the Zn-L intensity for comparison, to show that effects of local sample thickness can be excluded for the differences in intensity in the Cu-K_α – line.

For quantification, the average Cu/Zn ratio in a selected region (marked yellow) in an EDX map was determined (Figure 6.5). EDX quantification of the summed spectrum indicates an average Cu/Zn ratio of 1.5/100. Local clusters show a significantly increased amount of Cu signal, e.g., by a factor of 3 in the line scan shown in Figure 6.4. The Cu signal between the clusters is attributed to the presence of Cu in this region. Artificial Cu signal does not play a significant role as Cu free TEM grids were used.

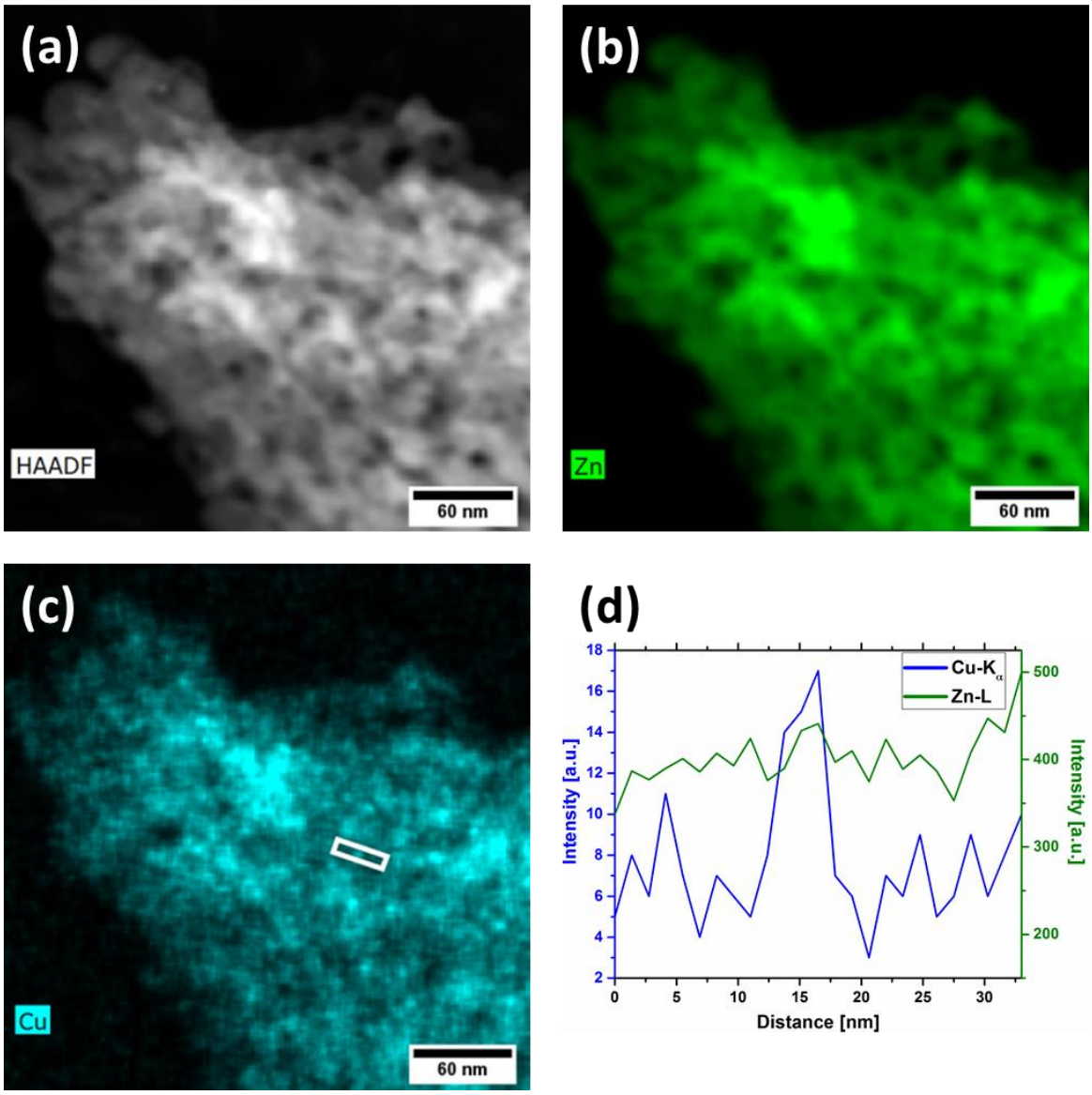

Figure 6.4: (a) STEM-HAADF and (b-c) EDX maps ((b) – Zn, (c) – Cu) and (d) line scan of 1.06 wt.% sample, 5 days in glove box. The white box in the Cu map indicates the area and direction of the line scan

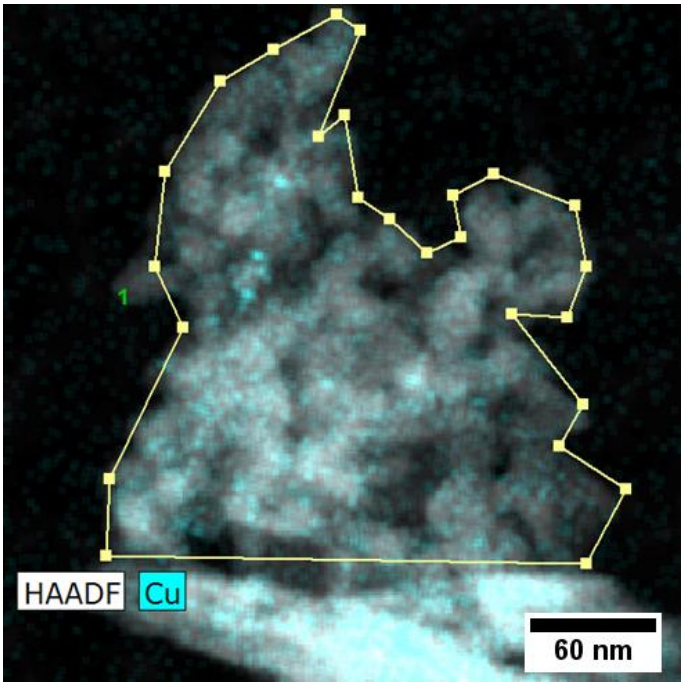

Figure 6.5: EDX map with selected region (yellow) – Image resolution of 490x490 pixels

While TEM confirms the presence of Cu-rich particles, the question remains if isolated Cu^{2+} species on or inside ZnO also exist which may contribute to the observed conductivity increase upon reduction. Therefore, electron paramagnetic resonance (EPR) experiments were performed on the reduced and non-reduced samples, gaining information about the nature and environment of Cu species. EPR is able to provide evidence of the presence of Cu^{2+}, since this ion is paramagnetic. Figure 6.6 (a) shows the EPR spectrum of the non-reduced Cu-doped ZnO sample exhibiting a strong signal around g = 2.05 with a broad, structured tail at low field due to hyperfine interaction (hfi) characteristic for isolated (no spin-spin interaction) Cu^{2+} ions (S = ½; $^{63(65)}$Cu: natural abundance 69.15 % (30.85 %) both I = 3/2). A closer inspection of the low field part of the signal indicates the presence of at least two different Cu^{2+} species. In contrast to this, the typical ZnO-defect signals (around g = 1.958 shallow donor states and g = 2.001 oxygen vacancies[27,28]) are found to be very weak for the non-reduced sample. This is in good agreement with previously reported EPR spectra of Cu:ZnO samples exhibiting strong Cu^{2+} signals as well as ZnO defect features of varying intensity.[27–30] It should be noted that in contrast to UV-vis-NIR measurements, the EPR spectra provide clear evidence for the presence of Cu^{2+} species in the sample

Upon reduction, the EPR spectrum of the Cu-doped ZnO markedly changes (see Figure 6.6 (b-d)). The Cu^{2+} signals are strongly decreased in intensity (factor of ≥10) consistent with

the expected (partial) reduction of Cu^{2+} species. Moreover, the signals of the typical defects in ZnO at g = 2.001 and g = 1.958 gain considerably in intensity (factor of > 5). Thus, these defects are largely induced by the reduction procedure. Please note that the amount of isolated Cu^{2+} centres in the reduced sample remains significantly higher than the number of ZnO related defects.

After prolonged storage of the reduced Cu-doped ZnO under vacuum in the sealed quartz tube (> 4 days), a broad feature centred at 290 mT appears and grows in intensity with increasing storage time, while the intensity of ZnO defect signals and Cu^{2+} signals discussed above display no significant change in intensity. Thus, the newly observed signal does not grow at the expense of the other EPR active species, suggesting that this signal is associated with previously EPR silent species. Hence, the results clearly show the reduced and sealed off sample to be metastable and subject to changes over long time periods.

It should be noted that in contrast to the reduced sample, no change over time or after heating in air could be observed for the non-reduced sample. Thus, while the reduced sample sealed off under vacuum demonstrated clear changes over time, the non-reduced sample appears to be stable, which is in line with the behaviour of the conductivity in the presence of an inert gas atmosphere. The EPR results suggest the process is not just a reoxidation to the initial state of the sample as the EPR signal clearly differs from that of the isolated Cu^{2+} ions dominating the EPR spectrum of the oxidised sample.

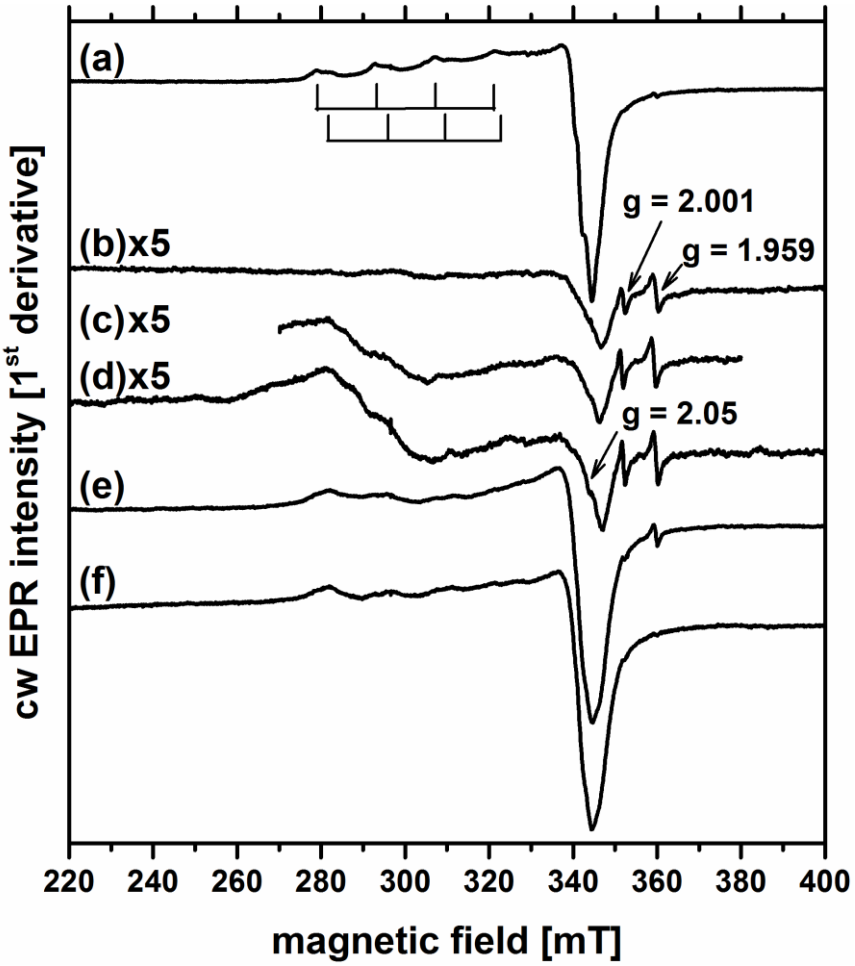

Figure 6.6: cw EPR spectra of the sample, (a) non-reduced, and reduced and in vacuum for (b) 40 h, (c) 90 h, and (d) 160 h, as well as reoxidised by (e) exposure to ambient air and (f) heating to 500 K in air

To investigate the reversibility of the effects of reduction, the reduced and sealed-off sample was opened and exposed to ambient air. The changes in the EPR signals are presented in Figure 6.6 (e). The Cu^{2+} signals increase immediately upon air exposure reaching approximately the level detected for the non-reduced sample after 1 day, in agreement with a reoxidation to Cu^{2+} species. The time scale of this reversible process is longer than in the MCPT measurements, as expected for an activated process conducted at lower temperatures. The signal at g = 2.001 markedly decreases in amplitude to a value similar to the non-reduced sample upon exposure to ambient air, while the signal at g = 1.959 increases in amplitude upon exposure to air. This is in contrast to the unreduced sample, where the g = 1.959 signal is nearly absent. The broad signal around 290 mT still appears to be present, but it is masked by the Cu^{2+} signals. The cw EPR spectra change only marginally upon prolonged air exposure time (data not shown). In contrast, subsequent heating of the sample to 500 K in air (Figure 6.6 (f)) results in a strong decrease

of the signal at g = 1.959 associated with defects in ZnO, while the Cu^{2+} related signal is hardly changed. Thus, the changes observed upon reduction are reversible for the Cu^{2+} as well as the ZnO defect signals, however, both exhibit a different temperature dependence, which excludes a direct correlation between the corresponding processes. In addition, the broad signal at 290 mT appears to remain present in the EPR spectra even after heating to elevated temperature. In previous EPR studies, a signal at a similar resonance position was attributed to exchange coupled Cu^{2+} species, namely Cu-dimers.[31] The high spin nature of the corresponding species is corroborated by EPR spectra taken at 34 GHz (data not shown), which indicate a marked zero field contribution to the observed resonance position. The appearance of the signal cannot be explained by a simple oxidation of the sample, e.g., by the residual gas present in the evacuated sample, as underlined by the EPR spectra of the opened sample. Thus, a more complex process leads to the presumably irreversible formation of EPR active from EPR silent species which occurs on a much longer time scale than the reversible processes observed by EPR. A possible scenario could be diffusion of Cu^{+} followed by a disproportionation to Cu^{2+} and Cu^{0}.

All in all, EPR clearly shows the reversibility of the reduction of isolated Cu^{2+} species and the formation of ZnO defects. Moreover, the presence of a slower, presumably irreversible, change in the reduced sample under inert conditions is evidenced.

6.5 Discussion

The sample with 1.06 wt.% loading of CuO on ZnO showed a complex response to reducing and oxidising atmospheres. Contactless measurements using MCPT showed an increase in conductivity when the sample was exposed to reducing conditions. After an initial fast increase, the conductivity increases slowly over several hours. This implies that there are several underlying processes responsible for the conductivity increase.

A possible cause of the initial fast conductivity increase is the reduction of Cu^{2+} species on the surface or subsurface (dissolved in the lattice of ZnO). The presence of such isolated Cu^{2+} species in the sample before reduction was shown by EPR measurements. The sample as synthesised shows signals corresponding to at least two types of isolated Cu^{2+} species. For the reduced and sealed off sample, the intensity of these species is drastically

reduced, in line with the interpretation that the Cu^{2+} ions get reduced to EPR-silent Cu^{+} or Cu^{0}. The electrons necessary to reduce Cu^{2+} are provided by the H_2 gas dissociating on the sample surface. The resulting H^{+} ions can produce OH-groups at the surface of the sample, or be removed as H_2O by reaction with oxygen from the sample. This is also supported by the fact that the amount of vacancies (shallow donor states and oxygen vacancies) in ZnO is increased concurrently.

In comparison to the fast reduction processes involving transfer of electrons through the sample,[32] mechanisms involving the restructuring of the sample such as movement of Cu^{2+} dopant ions to the surface and subsequent reduction will be slow.[33] Thus, such a process can lead to the slower conductivity increase observed in reducing conditions.

Under inert atmosphere after reduction, EPR evidences a slower and most likely irreversible change, showing that the reduced sample which was sealed off in vacuum is metastable.

When the sample is reoxidised, its conductivity immediately returns to the original value, which is maintained even in the following inert feed. EPR shows that the isolated Cu^{2+} species are largely reformed. Thus, this fast oxidation response most likely corresponds to a reoxidation of species inside the ZnO lattice which are EPR-silent under reducing and inert conditions. Since the conductivity returns to its original value, any of the processes responsible for the slow increase in reducing conditions would then have to be reversed during the inert conditions.

Overall, the changes of the sample induced by the application of reducing and oxidising conditions are mostly reversible, as the conductivity response to a second reduction indicates.

6.6 Conclusions

A CuO/ZnO sample, with an amount of CuO lower than the solubility limit in ZnO, prepared by impregnation of ZnO with copper citrate and subsequent calcination shows evidence of dissolution of Cu ions in the ZnO lattice. Our experimental results show that under reducing conditions, the amount of the observed Cu^{2+} species is decreased markedly. This is likely due to several processes, since the conductivity increase occurs on different time scales, one initial rapid increase followed by a further slow increase. The fast increase in

conductivity is most likely associated to the reduction of Cu^{2+} in the lattice of ZnO to EPR silent species (Cu^{+} or Cu^{0}). The state of the sample after reduction is metastable as evidenced by the slow decrease in conductivity observed in inert conditions, and the slow change in EPR signal over several days in the vacuum-sealed quartz tube. When the sample is re-oxidised, it returns to its original state as evidenced by *in situ* conductivity measurements and further supported by the return of the EPR signal associated with isolated Cu^{2+} ions. In a second reduction, the system shows the same conductivity response as during the first reduction step, indicating the reversibility of this redox process. Our findings highlight the dynamic nature of this sample and stress the importance of using *in situ* and inert transfer techniques. Further, the observed dynamic processes might be of general relevance while mimicking interfacial processes occuring in Cu/ZnO catalysts, for example in the sample series presented in chapter 5. In future investigations, experiments such as *in situ* EPR will be able to contribute to the understanding of this important catalytic system.

6.7 Acknowledgements

The authors thank J. Kröhnert for assistance in setting up the low-temperature UV-vis-NIR experiment. E.H.W. thanks the IMPRS (International Max Planck Research School) “Functional Interfaces in Physics and Chemistry” for funding and support. W.R. and T.R. thank the centre of Excellence “UNICAT” supported by the DFG and hosted at TU Berlin for financial support.

6.8 Bibliography

1 J. W. Geus and A. J. Van Dillen, *Prep. Solid Catal.*, 2008, 460–487.

2 R. Burch, S. E. Golunski and M. S. Spencer, *J. Chem. Soc. Faraday Trans.*, 1990, **86**, 2683–2691.

3 S. Zander, E. L. Kunkes, M. E. Schuster, J. Schumann, G. Weinberg, D. Teschner, N. Jacobsen, R. Schlögl and M. Behrens, *Angew. Chemie - Int. Ed.*, 2013, **52**, 6536–6540.

4 J. W. Andreasen, F. B. Rasmussen, S. Helveg, A. Molenbroek, K. Ståhl, M. M. Nielsen and R. Feidenhans’l, *J. Appl. Crystallogr.*, 2006, **39**, 209–221.

5 T. M. Yurieva, L. M. Plyasova, V. I. Zaikovskii, T. P. Minyukova, A. Bliek, J. C. van den Heuvel, L. P. Davydova, I. Y. Molina, M. P. Demeshkina, A. a. Khassin and E. D. Batyrev, *Phys. Chem. Chem. Phys.*, 2004, **6**, 4522.

6 R. G. Herman, K. Klier, G. W. Simmons, B. P. Finn and J. B. Bulko, *J. Catal.*, 1979, **56**, 407–429.

7 S. Mehta, G. W. Simmons, K. Klier and R. G. Herman, *J. Catal.*, 1979, **57**, 339–360.

8 Y. Okamoto, K. Fukino, T. Imanaka and S. Teranishi, *J. Phys. Chem.*, 1983, **87**, 3747–3754.

9 D. Stirling, F. S. Stone and M. S. Spencer, *Stud. Surf. Sci. Catal.*, 1993, **75**, 1507–1518.

10 Y. Choi, K. Futagami, T. Fujitani and J. Nakamura, *Appl. Catal., A*, 2001, **208**, 163–167.

11 M. Behrens, F. Studt, I. Kasatkin, S. Kühl, M. Hävecker, F. Abild-Pedersen, S. Zander, F. Girgsdies, P. Kurr, B.-L. Kniep, M. Tovar, R. W. Fischer, J. K. Nørskov and R. Schlögl, *Science*, 2012, **336**, 893–7.

12 D. O. Klenov, G. N. Kryukova and L. M. Plyasova, *J. Mater. Chem.*, 1998, **8**, 1665–1669.

13 J. D. Grunwaldt, A. M. Molenbroek, N. Y. Topsoe, H. Topsoe and B. S. Clausen, *J. Catal.*, 2000, **194**, 452–460.

14 N. Topsøe and H. Topsøe, *Top. Catal.*, 1999, **8**, 267–270.

15 M. Eichelbaum, R. Stösser, A. Karpov, C.-K. Dobner, F. Rosowski, A. Trunschke and R. Schlögl, *Phys. Chem. Chem. Phys.*, 2012, **14**, 1302–12.

16 D. Kajfez, *Q Factor Mesurements Using MATLAB (R)*, Artech House, Norwood, 2011.

17 D. C. Dube, *J. Phys. D Appl. Phys.*, 1970, **3**, 1648–1652.

18 H. Looyenga, *Physica*, 1965, **31**, 401–406.

19 D. Stirling and F. S. Stone, *Solid State Ionics*, 1993, **63**–**65**, 289–295.

20 V. Petranovskii, V. Gurin, N. Bogdanchikova, A. Licea-Claverie, Y. Sugi and E. Stoyanov, *Mater. Sci. Eng. A*, 2002, **332**, 174–183.

21 O. Akhavan and E. Ghaderi, *Surf. Coatings Technol.*, 2010, **205**, 219–223.

22 A. N. Pestryakov, V. P. Petranovskii, A. Kryazhov, O. Ozhereliev, N. Pfänder and A. Knop-Gericke, *Chem. Phys. Lett.*, 2004, **385**, 173–176.

23 D. Balzar, in *Microstructure Analysis from Diffraction*, ed. J. Snyder, R.L., Bunge, H.J., Fiala, International Union of Crystallography, 1999, p. 44.

24 J. Schumann, M. Eichelbaum, T. Lunkenbein, N. Thomas, M. C. Álvarez Galván, R. Schlögl and M. Behrens, *ACS Catal.*, 2015, 3260–3270.

25 R. W. G. Wyckoff, in *Crystal Structures 1*, Interscience Publishers, New York, 2nd Ed., 1963, pp. 7–83.

26 K. Kihara and G. B. T.-A. T. V. in Z. Donnay, *Can. Mineral.*, 1985, **23**, 647–654.

27 R. Buchheit, F. Acosta-Humánez and O. Almanza, *Rev. Cub. Fis.*, 2016, **33**, 4–12.

28 S. Colak and C. Aktürk, in EMR/ESR/EPR Spectroscopy for Characterization of Nanomaterials, 2017, vol. 62, pp. 151–179.

29 A. J. Reddy, M. K. Kokila, H. Nagabhushana, R. P. S. Chakradhar, C. Shivakumara, J. L. Rao and B. M. Nagabhushana, *J. Alloys Compd.*, 2011, **509**, 5349–5355.

30 K. I. Milenova, P. M. Nikolov, N. A. Kasabova and I. A. Avramova, *Polish J. Chem. Technol.*, 2014, **16**, 55–59.

31 F. Wang, R. Büchel, A. Savitsky, M. Zalibera, D. Widmann, S. E. Pratsinis, W. Lubitz and F. Schüth, *ACS Catal.*, 2016, **6**, 3520–3530.

32 N. A. Jayah, H. Yahaya, M. R. Mahmood, T. Terasako, K. Yasui and A. M. Hashim, *Nanoscale Res. Lett.*, 2015, **10**, 1–10.

33 D. G. Thomas and J. J. Lander, *J. Chem. Phys.*, 1956, **25**, 1136–1142.

6.9 Supporting Information

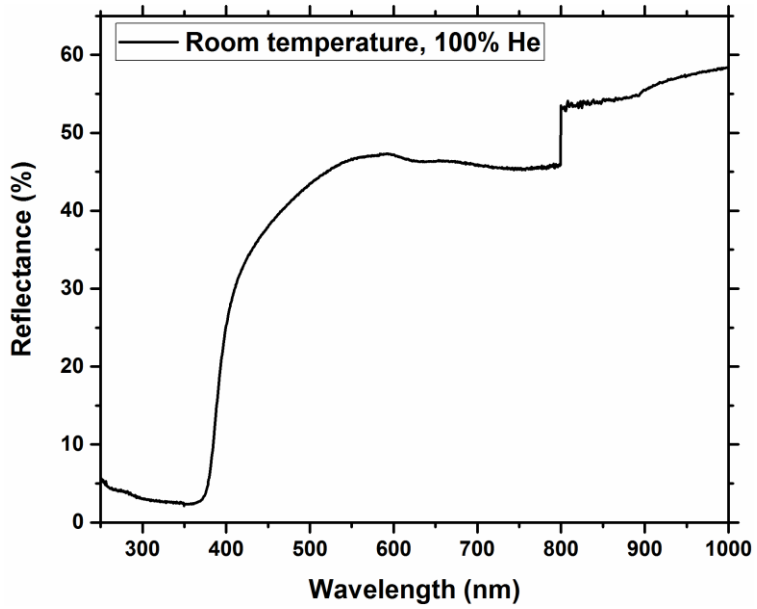

S 6.1: UV-vis spectrum of the as-synthesised sample.

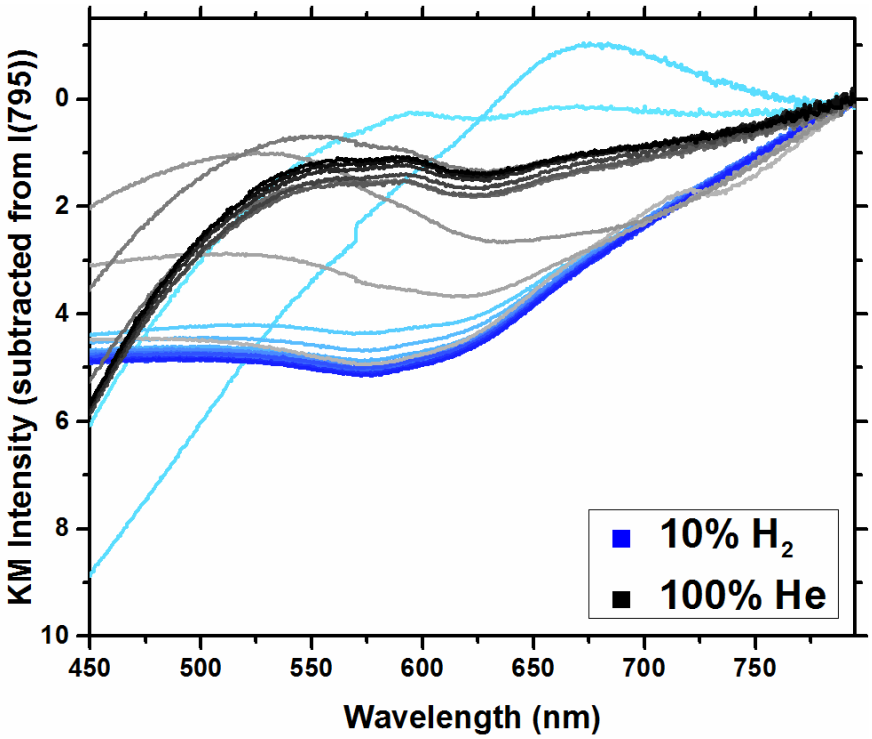

S 6.2: UV-vis spectra in reducing and inert conditions - normalised to intensity at 795 nm. Blue: Spectra in 10 % H2/He (230 °C) Black: Spectra in 100 % He (230°C). A more intense colour indicates a longer time in the respective atmosphere

To compare the intensity changes at different points throughout the visible region, the spectra were normalised to the intensity at 795 nm, where all spectra showed a characteristic kink due to a lamp/grating change in the spectrometer. A significant

reflectance loss occurred, especially in the visible region. We present the normalised intensity at several wavelengths in the centre of this region (between 565 nm and 635 nm), around the expected Cu plasmon region (590-600 nm). It becomes apparent that this region of the spectrum generally loses intensity upon switching to reducing gas, but no evidence of a plasmon band can be found.

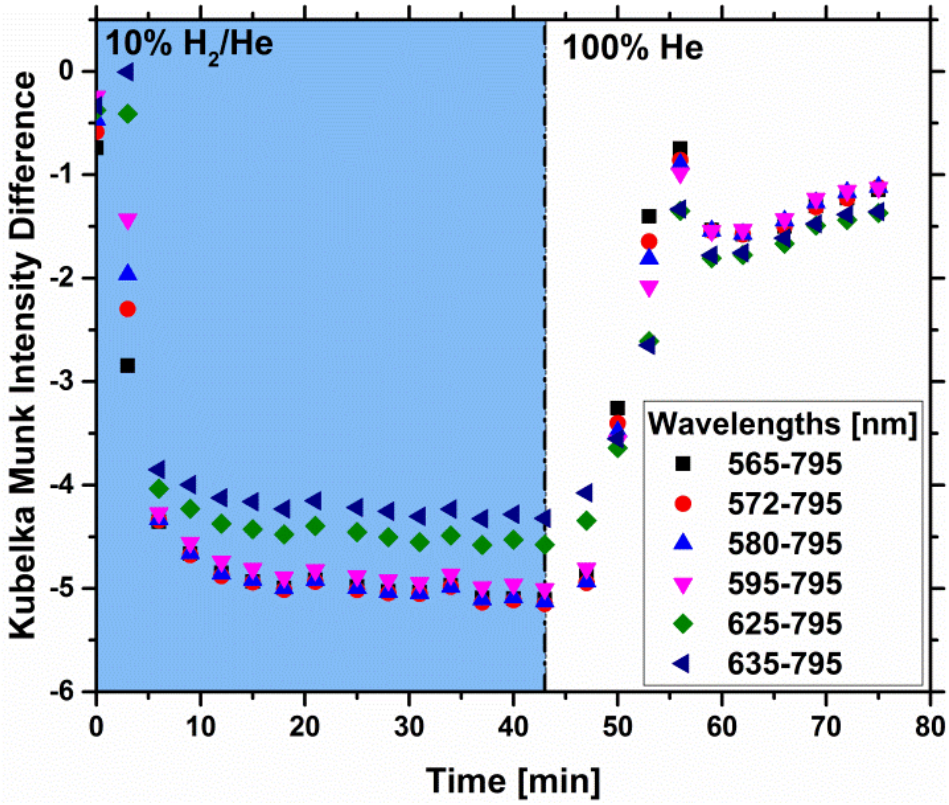

S 6.3: Intensities of selected wavelengths over time - normalised to intensity at 795 nm. The blue region indicates reducing conditions.

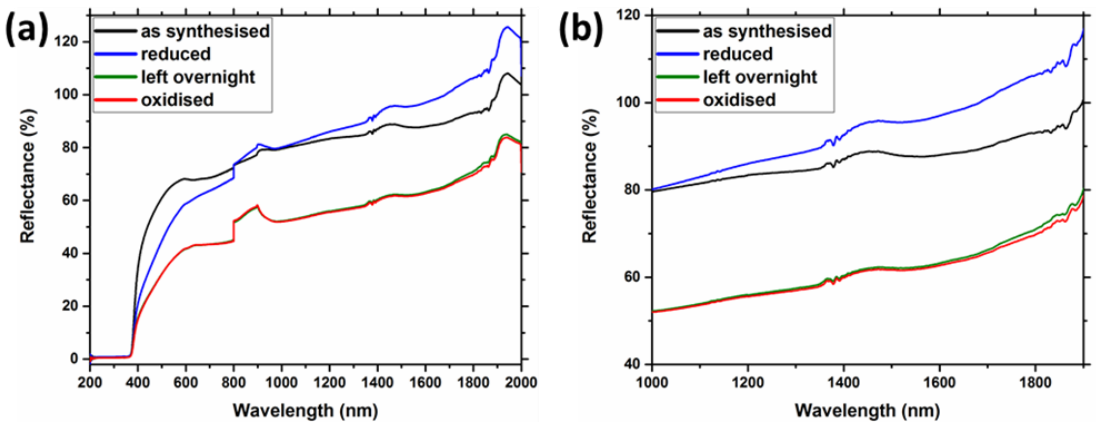

S 6.4: DR-UV-vis-NIR low temperature spectra as synthesised (black), after reduction at 250 °C in 10 % H_2/He (blue), after leaving in the evacuated cell overnight (green), and oxidised at 250 °C in 10 % O_2/He (red). (a) whole range spectrum and (b) close up

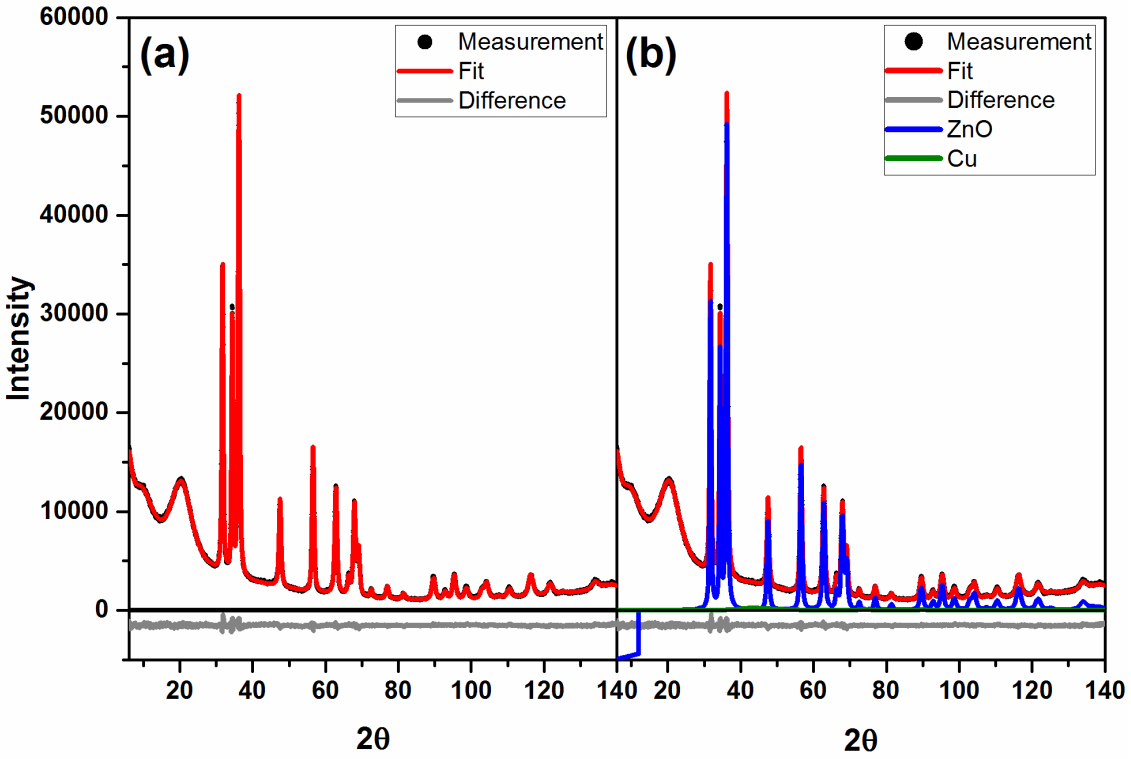

S 6.5: Whole XRD patterns of sample with fit (a) assuming ZnO as the only crystalline phase (b) assuming the presence of crystalline Cu metal in addition to ZnO. The broad features visible below 30° are caused by the airtight sample holder polymer cap.

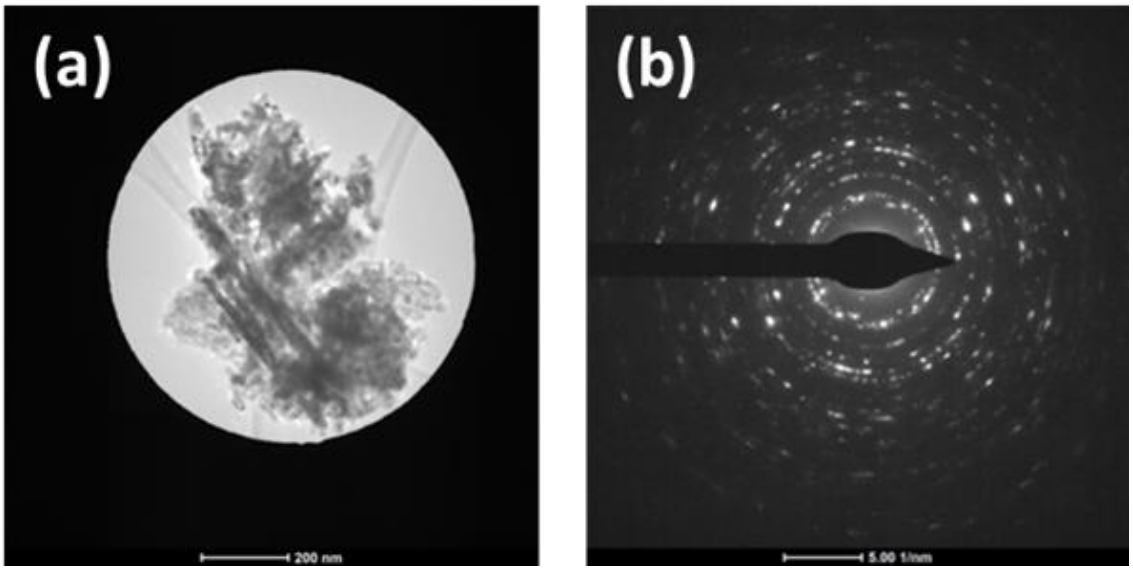

S 6.6: Selected area TEM image and corresponding diffraction pattern.

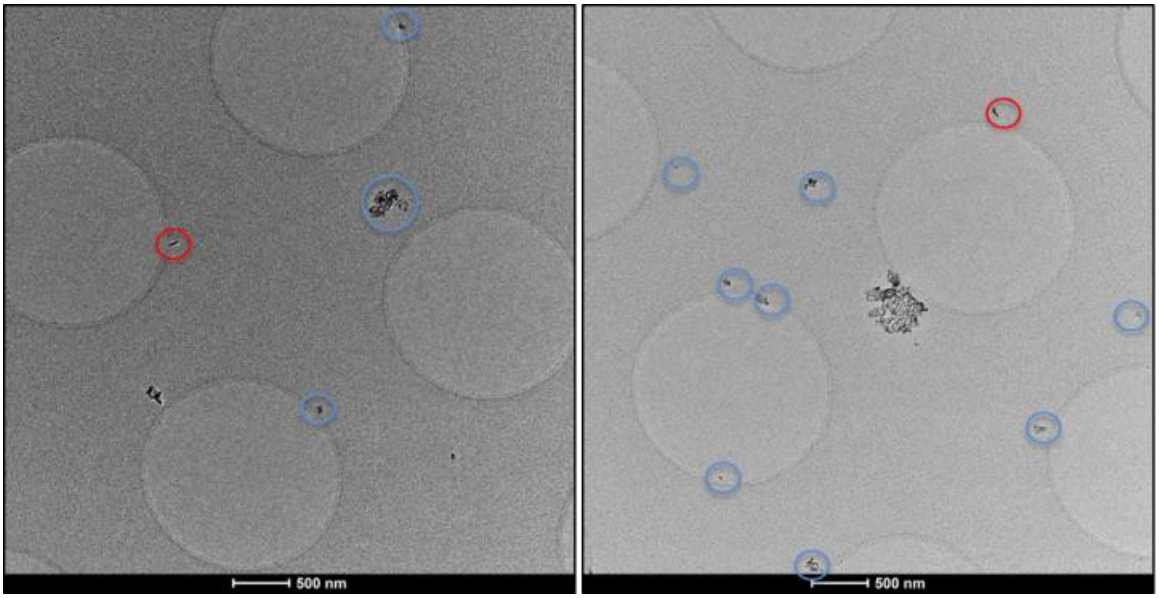

S 6.7: Example overview TEM counting morphology, ZnO. Regions with needle-like particles are marked in red, while regions with platelet-like particles are circled in blue.

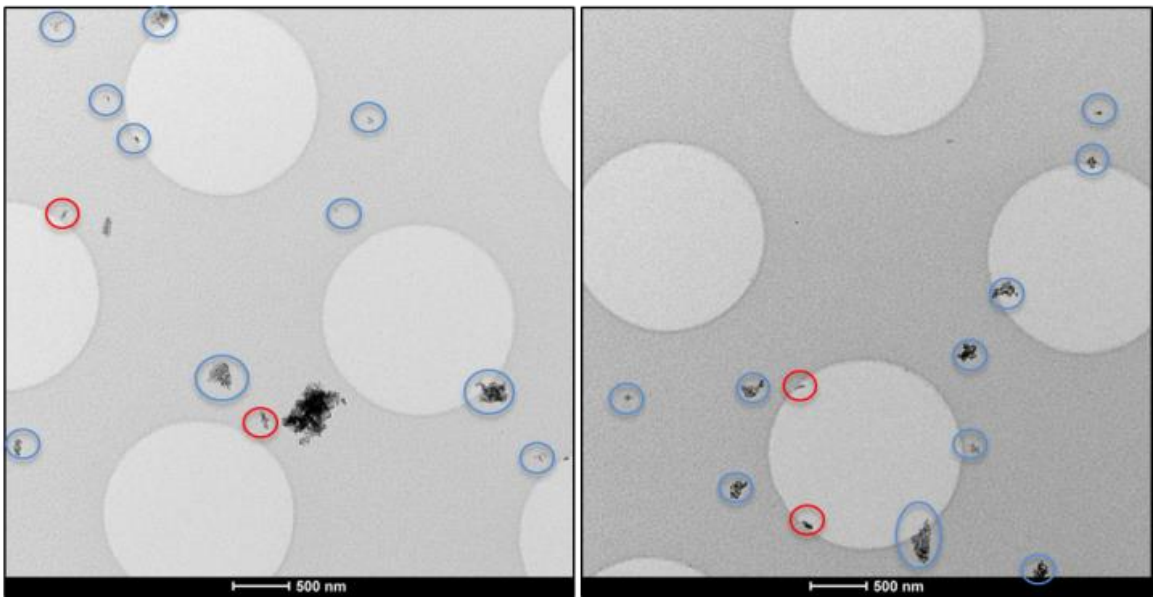

S 6.8: Example overview TEM counting morphology, sample. Regions with needle-like particles are marked in red, while regions with platelet-like particles are circled in blue

7 F-doping of nanostructured ZnO: a way to modify structural, electronic, and surface properties

Published paper: E. H. Wolf, M. Millet, F. Seitz, F. A. Redeker, W. Riedel, G. Scholz, W. Hetaba, D. Teschner, S. Wrabetz, F. Girgsdies, A. Klyushin, T. Risse, S. Riedel and E. Frei, Phys. Chem. Chem. Phys., 2020, 22, 11273

DOI: https://www.doi.org/10.1039/D0CP00545B - Published by the PCCP Owner Societies.

Author contributions: Elisabeth Hannah Wolf collected the experimental results by writing the paper, and organised the distribution of the samples to colleagues carrying out additional characterisation techniques. Furthermore, she carried out and evaluated the MCPT and DR-UV-vis experiments. Marie-Mathilde Millet synthesised the ZnO sample which also served as a precursor for ZnO_F1 and ZnO_F10 and provided feedback on the paper draft. Friedrich Seitz carried out and evaluated the IR experiments, provided a first draft of the corresponding sections, and provided feedback on the paper draft. Frenio A. Redeker carried out the treatment of ZnO with gaseous F_2, Wiebke Riedel carried out and evaluated the EPR experiments and provided feedback on the paper draft. Gudrun Scholz carried out and evaluated the NMR experiments and provided feedback on the paper draft. Walid Hetaba carried and evaluated the electron microscopy experiments and provided feedback on the paper draft. Detre Teschner carried out and evaluated the XPS experiments and provided feedback on the paper draft. Sabine Wrabetz carried out and evaluated the microcalorimetry experiments and provided feedback on the paper draft. Frank Girgsdies carried out and evaluated the XRD experiments and fits, and provided feedback on the paper draft. Alexander Klyushin carried out and evaluated the NEXAFS experiments and provided feedback on the paper draft. Thomas Risse oversaw the project, especially with regards to the EPR experiments, and provided feedback to the paper draft. Sebastian Riedel oversaw the project, especially with regards to the fluorine treatment. Elias Frei designed and oversaw the entire project, and provided extensive feedback on the paper draft.

8 Appendix: Microwave Cavity Perturbation Measurements of Highly Perturbing Samples

8.1 Method

In order to exemplify the loss of resonance which occurs for samples which disturb the field to a high degree, along with the progressively increasing peak shift and peak broadening of the signal (reflection coefficient vs. frequency), it is necessary to measure comparable samples which perturb the field to an increasing degree. For this reason, it was chosen to produce physical mixtures of commercially available compounds, selecting carbon black as the highly perturbing, and silica as the non-perturbing materials. To ensure a good separation between carbon particles, SiO_2 is chosen in nanopowder form. After weighing out the components, they were mixed in an agate mortar until visual homogeneity was achieved. After measurement in the MCPT setup, the quality factor Q was determined using three methods (Kajfez'[1] and Heine's[2] algorithms and fitting a Lorentz peak to the experimental data, with details given in chapter 2.4.). This method was then applied to the real-world application of hydrothermal carbon samples as a further example of a highly perturbing system. These materials are used, for example, as supports for electrocatalysts.[3] For their use as such supports, the materials are required to be good conductors, since they must ensure a good transport of electrons between electrode and catalyst.

8.2 Experimental

8.2.1 Hydrothermal carbon series

Hydrothermal carbon materials were provided by our collaborators at MPI-CEC Mülheim an der Ruhr, Department of Heterogeneous Reactions. The development of the synthesis and a detailed characterisation of the samples was published previously.[3] The materials were carbon samples prepared by hydrothermal synthesis from glucose at different pH (pH = 0, 1, 3, and 6) by synthesising in differently concentrated aqueous HNO_3 solutions. For a typical synthesis, 72 g of glucose were placed in the HNO_3/H_2O solvent and reacted in a hydrothermal reactor at 473 K for 6 h. Each batch was divided in two parts, one of which was furthermore annealed under a flow of N_2 (487.5 mL/min) at 1173 K for 5 h. The annealed sample with the highest synthesis pH was expected to have the highest

conductivity and thus perturb the field the most, so measurements of a dilution series were performed with this sample. A 1:20 HTC:SiO_2 ratio was chosen after inspection of the resulting resonance peaks for subsequent measurement of the whole HTC series in order to limit the dielectric loss produced by the samples. Exact dilution proportions of the HTC dilution series and of the 1:20 dilutions of the whole sample series are given below.

Table 8.1: Dilution series of HTC pH6, annealed.

Dilution	silica weight (mg)	carbon weight (mg)	carbon content (% weight)	Internal sample number
1:100	100.7	0.7	0.6903	#26265
1:50	114.3	3.2	2.7234	#26266
1:20	115.9	6.0	4.9221	#26267
1:10	99.1	10.9	9.9091	#26268
1:5	107.5	20.8	16.2120	#26269
1:1	51.2	47.4	48.0730	#26270

Table 8.2: 1:20 dilution of HTC samples in SiO_2.

Sample	silica weight (mg)	carbon weight (mg)	carbon content (% weight)	Internal sample number
RSG-NK-731:silica 1:20	113.3	5.7	4.7899	#26302
RSG-NK-732:silica 1:20	95.3	4.7	4.7000	#26303
RSG-NK-698-silica 1:20	84.6	4.2	4.7297	#26304
RSG-NK-699:silica 1:20	78.7	3.9	4.7215	#26305
RSG-NK-784:silica 1:20	78.8	3.9	4.7158	#26323
RSG-NK-711:silica 1:20	71.9	3.6	4.7682	#26324
RSG-NK-783:silica 1:20	91.3	4.5	4.6973	#26325

8.2.2 Preparation of a dilution series of carbon black in silica

A dilution series of commercial carbon black (Alfa Aesar carbon black, super P, conductive, 99+ % (metals basis)) in silica (Aldrich silicon dioxide nanopowder, 10 nm, 99.5 %) was produced by physically mixing appropriate amounts of the two components using an

agate pestle and mortar until visual homogeneity was achieved. An overview of the samples' composition can be found in the table below.

Table 8.3: Composition of diluted carbon samples.

Sample description	silica weight (mg)	carbon weight (mg)	carbon content (% weight)	Internal sample number
carbon black:silica 1:100	204.0	2.0	0.9709	#21797
carbon black:silica 1:20	106.4	6.4	5.6738	#21796
carbon black:silica 1:10	109.7	12.4	10.1556	#21795
carbon black:silica 1:5	103.1	19.9	16.1789	#21794
carbon black:silica 1:1	104.6	108.9	51.0070	#21793

8.2.3 MCPT measurements

A typical microwave cavity perturbation technique (MCPT) experiment using the previously published setup[4] was carried out as follows: A quartz glass sample tube was filled with a fixed bed of the sample under test between two glass wool plugs. The bed length was determined using a calliper and was about 5 mm in the case of the carbon black dilution series measurements and about 10 mm in the case of the hydrothermal carbons and the HTC dilution series. The exact bed lengths and sample weights can be found in Table 8.4). The inner diameter of the reactor was 3 mm. The TM_{010} mode of a J-Band resonator at about 6.73 GHz (carbon dilution series) and of an S-band resonator at about 3.26 GHz (hydrothermal carbons) were used, respectively. The resonator was cooled to about 292 K using Peltier elements placed above and below the resonator, which were in turn cooled using a water cooling system. The temperature of the samples was approximately 293 K as measured with a thermocouple located in the sample tube just outside the cavity, and the measurement was performed without application of any gas flow. The cavity was flushed with 15 mL/min N_2 gas in order to prevent possible condensation of water on the cavity walls. For each measurement, 20001 measurement points (reflection coefficient vs. frequency) were taken in the selected measurement range. Three runs were taken consecutively to give the data for one measurement as an average. An IF bandwidth (IFBW) of 500 Hz and a save delay (time of the start of one

measurement to the start of the next) of 150 s were used for all measurements, such that a new measurement (average of three runs) was taken every 2.5 min. The data acquisition was carried out until the data received reached a reasonable degree of stability, after an initial drift had settled. For each experiment, a corresponding empty measurement was performed using the exact same reactor (without sample and glass wool) and same measurement protocol.

Table 8.4: Sample tube filling and sample weight of the measured carbon samples.

Sample	sample weight (mg)	bed length (mm)
SiO_2 (commercial)	5.1	4.4
carbon black:silica 1:100	9.5	5.1
carbon black:silica 1:20	7.8	5.25
carbon black:silica 1:10	7.6	5.45
carbon black:silica 1:5	8.8	6.45
carbon black:silica 1:1	4.2	5.45
RSG-NK-566:silica 1:100	17.5	9.5
RSG-NK-566:silica 1:50	15.7	9.55
RSG-NK-566:silica 1:20	17.2	9.9
RSG-NK-566:silica 1:10	18.5	8.6
RSG-NK-566:silica 1:5	13.5	9.6
RSG-NK-566:silica 1:1	10.5	9.15
RSG-NK-731:silica 1:20	18.8	9.5
RSG-NK-732:silica 1:20	18.0	10.55
RSG-NK-698-silica 1:20	20.1	10.6
RSG-NK-699:silica 1:20	18.6	9.65
RSG-NK-784:silica 1:20	22.7	11.1
RSG-NK-712:silica 1:20	19.5	10.5
RSG-NK-783:silica 1:20	20.8	10.7
SiO2 (commercial)	12.9	8.8

8.3 Results and Discussion

8.3.1 Comparison of the conductivity of different hydrothermal carbon samples

In the following, conductivity measurements of differently synthesised hydrothermal carbons (HTCs) are presented. Owing to their applications in electocatalysts, the conducitivtiy of the samples is higher than for samples usually measured using MCPT, resulting in higher dielectric losses. Therefore, a dilution series of the sample with the highest expected conductivity was generated. This sample had been synthesised at pH = 6

and undergone the thermal annealing treatment. Annealing can be expected to increase the amount of conductive graphitic carbon in the sample.[5,6] In case the conductivity of several samples is to be compared, it is especially important to ensure comparable conditions for all samples and the applicability of the underlying perturbation theory throughout the series of samples. Because the samples perturb the field to a different degree, it is possible that the point at which measurement becomes unreliable and application of the equations given above becomes unsuitable is at different concentrations of sample in dilution medium. If one stays sufficiently far away from this point, it is possible to compare samples diluted to the same extent. In Figure 8.1, the MCPT signal of the last measurement of each sample in the dilution series is presented.

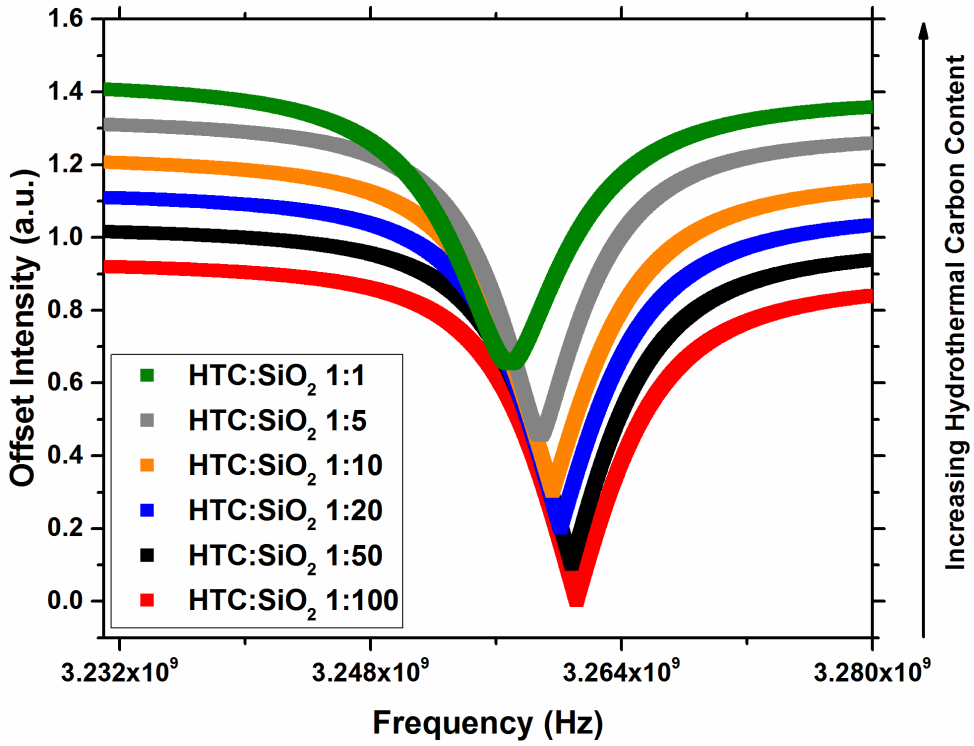

Figure 8.1: MCPT signal intensity versus frequency for the dilution series of the HTC sample which was expected to perturb the field the most in silica. The data have been offset for increased clarity.

The conductivity of the dilution series samples was calculated from the formulae presented in the introduction after determining Q using the method by Heine[2]. In order to account for the powder form of the samples, prior to calculation of the conductivity the sample permittivities were corrected as explained before. The obtained quality factors and conductivity values are presented in Figure 8.2. Both quality factor and conductivity depend linearly on the carbon content except obtained for the sample with about 10 %

carbon content which shows a lower conductivity than expected. From these results it is concluded that all samples in this dilution series can be investigated with this technique. To elucidate the impact of dilution on the ability to reproducibly determine the conductivity of the sample, which may become important in case of samples with even higher losses, the focus was put on the highly diluted side of this series choosing samples with a dilution ratio of 1:20 to compare the conductivities within the series of HTC carbon samples.

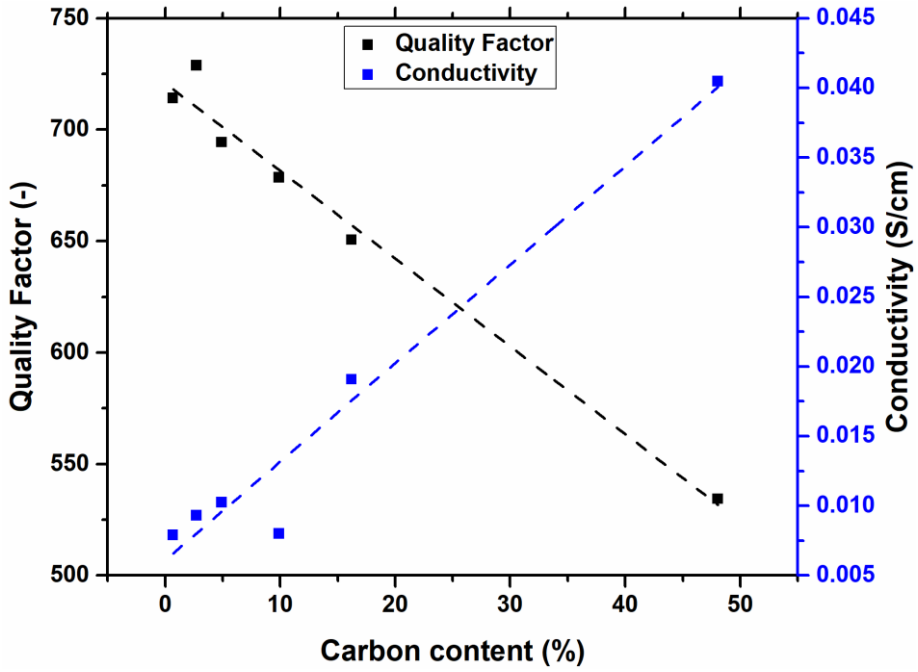

Figure 8.2: Quality factor (left axis, black) and conductivity (right axis, blue) of the diluted HTC sample (synthesis pH = 6, annealed).The dashed lines serve as guides for the eye.

The conductivity results of the diluted HTC samples for the series are presented in Figure 8.3. As expected, the most basic preparation conditions result in samples with the highest conductivity. The sample synthesised at pH 6 showed an increased conductivity after annealing to high temperature, which is likely due to increased amounts of conductive graphitic carbon in the sample. [5,6] An increase of the conductivity upon annealing is also observed for samples prepared at pH 1 and 3, however, the absolute conductivity is significantly smaller than found for the sample at pH 6. While the sample synthesised at pH 0 exhibits a slightly higher conductivity in the non-annealed state as compared to the samples at pH 1 and 3, annealing to 1173 K results in a small reduction of the conductivity, which indicates a complex interplay between the different preparation parameters.

However, the results nicely illustrate the ability to use diluted samples for a reliable determination, which allows to address changes within a sample series.

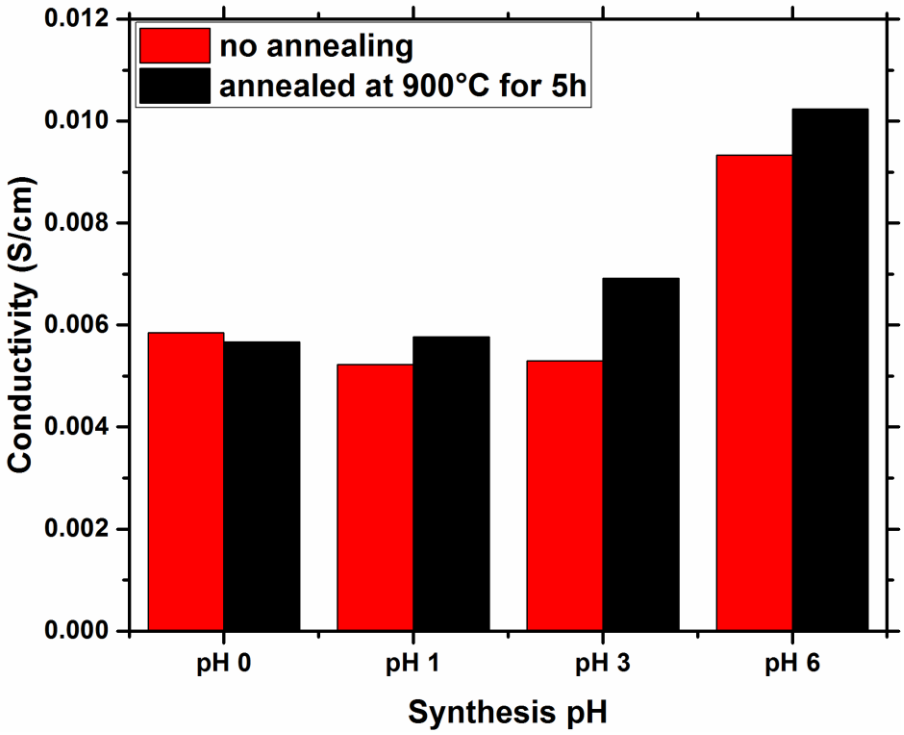

Figure 8.3: Conductivity of the diluted hydrothermal carbon synthesised at different pH without and with annealing treatment.

8.3.2 Dilution series of carbon black in silica

In order to illustrate the effects of introducing a more conductive sample into the setup, carbon black samples were investigated. A series of samples containing increasing amounts of carbon black diluted in SiO_2 as the non-perturbing matrix was measured in the MCPT setup. Results from this investigation were already presented in chapter 2.4, but a more detailed analysis will be presented here. From comparison of the MCPT signal intensities of this dilution series (Figure 2.4) to the one presented in Figure 8.1, it becomes clear that the shift in resonance frequency and peak broadening observed upon increasing the amount of carbon in the sample is more severe than in the case of the HTC sample. It can thus already be deduced that this sample results in higher dielectric losses and has a higher conductivity than the HTC sample.

From the MCPT signal, the quality factor was determined using Kajfez' algorithm.[1] Figure 8.4 presents a comparison of the quality factors of the setup for the samples in this dilution series as a function of time. As seen from the inset, the temporal changes of the

Q factor with time are significantly below 1 %. The slight drift towards higher Q values with time is due to a slight change in temperature when the sample is transferred from the laboratory atmosphere into the cooled resonator. The ability to observe this small effect highlights the stability of the current setup. It is possible to select a range where reasonable stability is reached (marked in the example in grey colour) to take an average Q as an equilibrium quality factor.

Within the dilution series, an increasing carbon content results in a decreasing, Q, since more energy is dissipated in the overall more conductive sample.

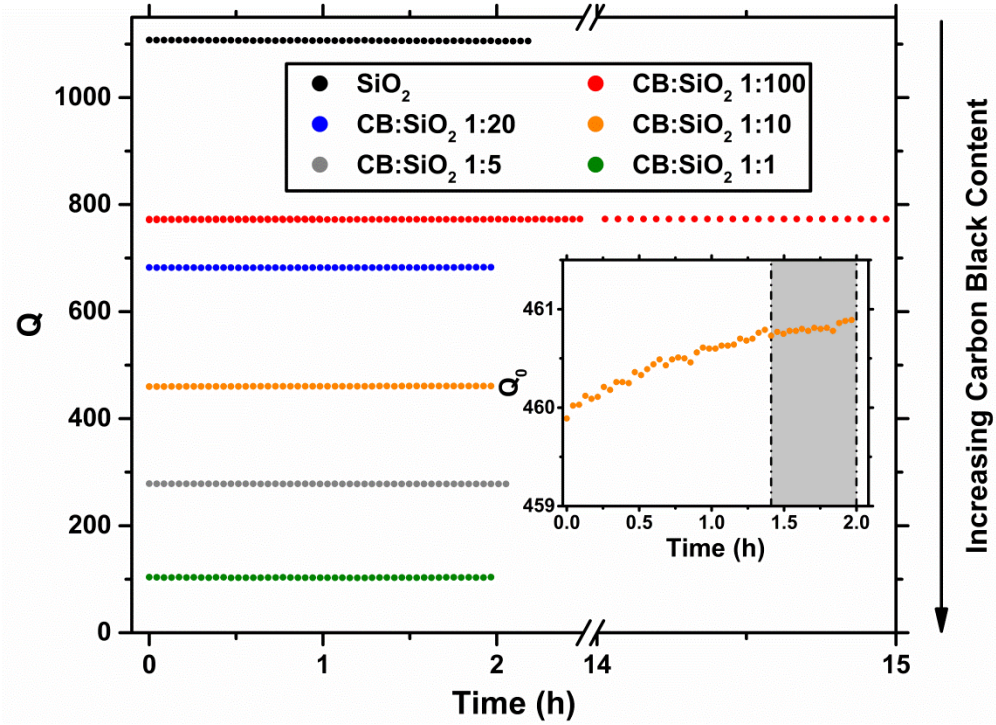

Figure 8.4: Q factors vs. measurement time of the carbon black dilution series.

The description of the average Q factors thus determined for this dilution series Figure 2.5) and the implications for the choice of dilution ratio was already presented in chapter 2.4, and will therefore not be repeated here. In short, a decrease in Q with increasing carbon content was observed, which flattened off significantly towards the high carbon content end of the dilution series. The choice of dilution should be made from the first regime where there still is a linear decrease in Q with increasing content of conductive sample.

8.3.3 Conclusions from the MCPT measurements of carbon samples

In this chapter, it was shown that dilution of carbon samples with the non-perturbing material SiO_2 facilitates the measurement and comparison of these samples of high conductivity. This provides a pathway for the contact-free conductivity measurement of highly conductive materials. Problems such as loss of resonance and measurement outside of the regime where the perturbation technique can reasonably be applied are overcome by this method, which enabled the measurement and comparison of the conductivities of several hydrothermal carbon materials produced under different conditions. The comparison between the experiments performed using carbon black and HTC revealed that the different carbon samples show a significantly different response to MCPT. The different conductivities of the sample and the response function of the technique results in differences in the range of concentrations which can be used for a proper determination of the conductivities. Furthermore, it was shown that the operational window in terms of dilution does not depend on the fit method chosen for the evaluation of the quality factor Q.

8.3.4 Dilution of 9.65Cu-C and MCPT measurements in reducing conditions

In order to facilitate a sufficient data quality for the MCPT measurements of the coprecipitated samples used in chapter 5, the highest loaded sample 9.65Cu-C was diluted and investigated in reducing conditions. As mentioned in chapter 2.4, in case that *operando* MCPT investigations are required, it is necessary to ensure a sufficient dilution under the most conductive conditions expected to occur throughout the entire measurement series. For this reason, the sample with the highest Cu content was investigated in the most reductive conditions planned throughout the experiments, namely 10 % H_2/N_2 at 250 °C. The dilution series was prepared by shaking the appropriate amounts of 9.65Cu-C and SiO_2 in a glass vial until visual homogeneity was achieved. The 100-200 µm sieve fraction of both materials was used to ensure that a gas flow could be applied during the *operando* experiment, and the samples were mixed in a glass vial by shaking rather than using a mortar and pestle to preserve the sieve fraction. For the MCPT measurements, the TM_{020} mode of an S-band resonator was employed. In Figure 8.5, the results of this investigation are presented. As expected, the resonance peak shifted and broadened with increasing content of 9.65Cu-C in the mixture. The data quality of all

samples which had been diluted with SiO_2 appeared sufficient for the necessary subsequent fitting step in contrast to the data of the undiluted (100 %) 9.65Cu-C sample. Most importantly, this sample's data contained a large shift and broadening of the resonance peak, as well as a second mode appearing at the high frequency side of the chosen frequency window. For this reason, a 1:1 dilution of CuO/ZnO precursor to SiO_2 was chosen for the investigation of all coprecipitated samples in chapter 5. This made the measurement of the samples and the subsequent data analysis possible and convenient, while still ensuring the highest possible catalyst content in the reactor, making the analysis of the conversion feasible.

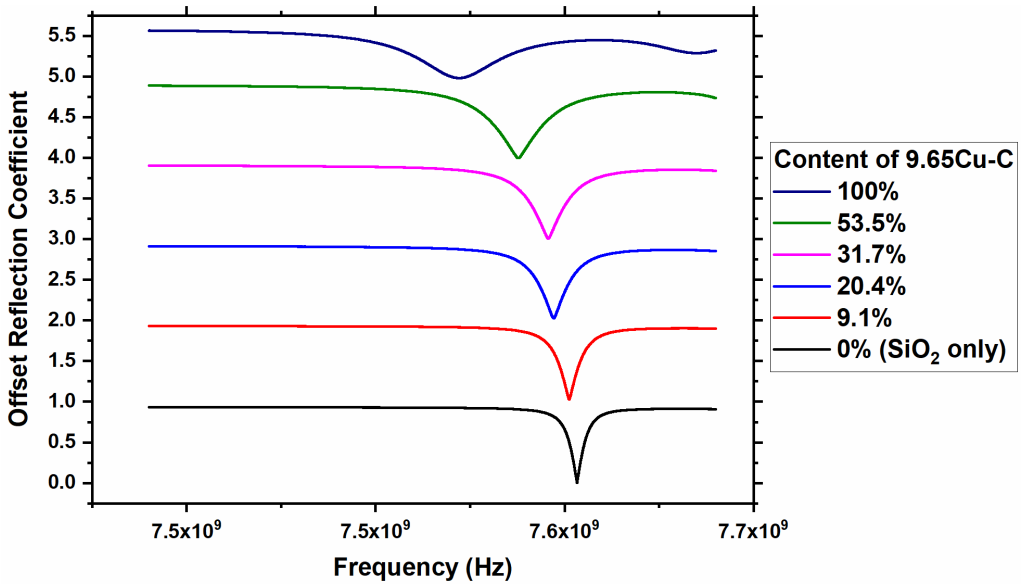

Figure 8.5: MCPT reflection coefficient vs. frequency of the dilution series of 9.65Cu-C with SiO_2.

8.3.5 Bibliography

1 D. Kajfez, *Q Factor Mesurements Using MATLAB (R)*, Artech House, Norwood, 2011.

2 C. Heine, Dissertation, The Electronic Structure of Vanadium Oxides as Catalysts in the Selective Oxidation of Small Alkanes The Electronic Structure of Vanadium Oxides as Catalysts in the Selective Oxidation of Small Alkanes, Technische Universität Berlin, 2014.

3 S. Reiche, N. Kowalew and R. Schlögl, *ChemPhysChem*, 2014, **16**, 579–587.

4 M. Eichelbaum, R. Stösser, A. Karpov, C.-K. Dobner, F. Rosowski, A. Trunschke and R. Schlögl, *Phys. Chem. Chem. Phys.*, 2012, **14**, 1302–12.

5 D. Krishnan, K. Raidongia, J. Shao and J. Huang, *ACS Nano*, 2014, **8**, 449–457.

6 M. Zhao, B. Li, J. X. Cai, C. Liu, K. G. McAdam and K. Zhang, *Fuel Process. Technol.*, 2016, **153**, 43–49.

List of Publications

- “F-doping of nanostructured ZnO: A way to modify structural, electronic, and surface properties” (Elisabeth Hannah Wolf, Marie-Mathilde Millet, Friedrich Seitz, Frenio A. Redeker, Wiebke Riedel, Gudrun Scholz, Walid Hetaba Detre Teschner, Sabine Wrabetz, Frank Girgsdies, Alexander Klyushin, Thomas Risse, Sebastian Riedel, and Elias Frei), Phys. Chem. Chem. Phys., 2020, **22**, 11273–11285

- “Synthesis and Characterization of Ag-Delafossites $AgBO_2$ (B: Al, Ga, In) from a Rapid Hydrothermal Process” (Leon Zwiener, Travis Jones, Elisabeth Hannah Wolf, Frank Girgsdies, Milivoj Plodinec, Alexander Yu. Klyushin, Elena Willinger, Frank Rosowski, Robert Schlögl, Elias Frei), European Journal of Inorganic Chemistry, 2019,18,2333

Selbstständigkeitserklärung

Hiermit versichere ich, die vorligende Dissertation selbstständig und ohne unerlaubte Hilfe angefertigt zu haben. Bei der Verfassung der Dissertation wurden keine anderen als die in der Dissertation angegebenen Hilfsmittel verwendet.

Elisabeth Hannah Wolf

Statement of Honesty

I hereby declare that the presented dissertation was prepared by myself and without impermissible help. No resources other than those indicated were used to write this dissertation.

Elisabeth Hannah Wolf